The Effect of Bubbles on Developed Turbulence

Promotiecommissie

Voorzitter:	Prof. dr. ir. L. van Wijngaarden	Universiteit Twente TNW
Promotor:	Prof. dr. rer. nat. D. Lohse	Universiteit Twente TNW
Leden:	Prof. dr. ing. D.H.A. Blank	Universiteit Twente TNW
	Prof. dr. H.J.H. Clercx	Technische Universiteit Eindhoven
	Prof. dr. D.P. Lathrop	University of Maryland
	Prof. dr. ir. L. Lefferts	Universiteit Twente TNW
	Prof. dr. ir. Th.H. van der Meer	Universiteit Twente CTW
	Prof. dr. ir. G. Ooms	Technische Universiteit Delft

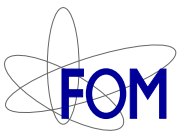

The research described in this thesis is part of the research program of the "Stichting voor Fundamenteel Onderzoek der Materie" (FOM), which is financially supported by the "Nederlandse Organisatie voor Wetenschappelijk Onderzoek" (NWO). It was carried out at the Physics of Fluids research group of the faculty of Science and Technology of the University of Twente.

Nederlandse titel:
Het effect van bellen op turbulente stromingen

Publisher:
Ramon van den Berg, Physics of Fluids, University of Twente,
P.O. Box 217, 7500 AE Enschede, The Netherlands
pof.tnw.utwente.nl

Cover design: Ramon van den Berg
Photo courtesy cover: Tom Koritschan
Print: Gildeprint B.V., Enschede

ISBN-10: 90-365-2421-0
ISBN-13: 978-90-365-2421-6

THE EFFECT OF BUBBLES ON DEVELOPED TURBULENCE

PROEFSCHRIFT

ter verkrijging van
de graad van doctor aan de Universiteit Twente,
op gezag van de rector magnificus,
prof. dr. W. H. M. Zijm,
volgens besluit van het College voor Promoties
in het openbaar te verdedigen
op donderdag 21 december 2006 om 15.00 uur

door

Thomas Hendrik van den Berg
(Ramon)

geboren op 2 juni 1976

te Reeuwijk

Dit proefschrift is goedgekeurd door de promotor:
prof. dr. rer. nat. Detlef Lohse

Contents

1 Introduction

1.1 What is turbulence?

It is hard trying to imagine what ordinary life would look like in the absence of turbulence. Being such a common aspect of daily life, it is hardly even noticed how omnipresent turbulence actually is. For instance: stirring milk in your coffee would be quite an adventurous task in the absence of turbulence. The normal way is to whisk a few turns with a spoon in your coffee and the developing turbulent structures in the coffee and milk will soon make the fluids completely mixed. Without turbulence one would have to keep on stirring to basically fold the different coffee and milk layers over each other to reach the desired mixture. Of course, Brownian motion, the random movement of molecules could also do the trick, but that would certainly be a lengthy procedure, after which the coffee would at least be cold, if not already completely evaporated.

Figure 1.1: Daily life turbulence

Turbulence really *is* everywhere: in your coffee, in air, in stellar cloud formations, in your arteries, pipelines, combustion in car engines, the air flow around this car while driving, flow around a ship, in rising smoke from a chimney, ocean streams or clouds passing over an island (see Fig. 1.2). The interactions of us humans with turbulence can be rather useful like the aforementioned coffee, or unwanted like tornadoes or experiencing a bumpy ride in an airplane due to strong turbulence.

Apparently, turbulence is a fairly familiar phenomenon, but it never-

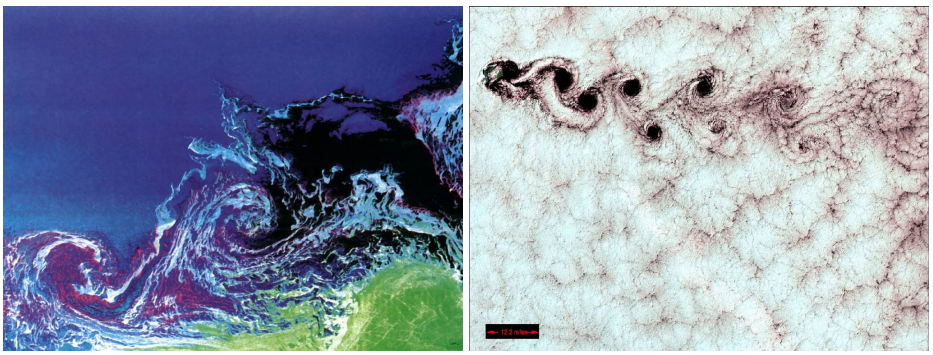

Figure 1.2: Ocean stream in the Wendell Sea (left) and Von Kármán vortices developing in the clouds over Tenerife (right).

theless is not so straightforward to give a precise and accurate definition, making it a loved topic of research. Leonardo da Vinci was one of the first known to study it by placing obstructions in water and sketch the result, comparing it with the curls in an old mans beard as he states: *'Observe the motion of the surface of the water, which resembles that of hair, which has two motions, of which one is caused by the weight of the hair, the other by the direction of the curls; thus the water has eddying motions, one part of which is due to the principal current, the other to random and reverse motion.'*

Centuries later, Osborne Reynolds called it '*sinuous motion*' (which it certainly is not), while Taylor and Von Kármán defined it as *'Turbulence is an irregular motion which in general makes its appearance in fluids, gaseous or liquids, when they flow past solid surfaces or even when neighboring streams of the same fluid pass or over one another.'*

Figure 1.3: da Vinci's sketches comparing the beard of an old man with the turbulent structures observed in water.

Telling what turbulence is not, is actually a lot easier, because a flow of fluids, either gaseous or liquid, can be roughly divided in two different types: turbulent and laminar. Laminar flow is typically smooth and regular, while a turbulent flow is, simply stated, not. The physical quantities like velocity, temperature and pressure are for a turbulent flow, in contrast to the laminar case, fluctuating in

sharp and irregular peaks, both in space and time. This gives us the first out of four general properties of turbulence:

- *Turbulence is random.*
  This means that the velocity, temperature, and pressure of the fluid at any given point at any time can not be predicted. Nevertheless, the averages over space, time or ensemble do show regular behavior. One can compare this with throwing a die. One knows that the chances on throwing a four in the next throw of the die are $\frac{1}{6}$, but one does not know what the next throw actually will be and neither can one predict an individual realization, even after knowing an indefinite amount of previous outcomes. The only certainty is that *on average* every number of the die will show up in $\frac{1}{6}$ of the total number of throws. This is called a stochastic process, and so is turbulence.

- The second property: *Turbulence is intermittent.*
  Although turbulence is a random process, it has some deviations from 'real' Gaussian random processes which are normally distributed. If we go back to the previous example of the die, if one throws two dices, on average one expects to throw a 7 as a total for the two dices most of the times, and 2 or 12 to show up less often. For turbulence the 'outliers' (so the high and low values) tend to show up more often than ordinary chance would predict. It is thus also a way to investigate whether or not a process is turbulent or ordinary chaos.

- The third property: *Turbulence shows universal behavior.*
  Given that the length scales one is investigating are larger than those for which viscous effects play a role and smaller than the length scale on which the turbulence is driven vortices in developed turbulence look and behave all the same, either smoke rising out of chimney, or water in a channel.

- The fourth property: *Turbulence decays without energy input.*
  Turbulence needs energy input, or it will decay to a laminar state.

The last property is a strong one and practically the key to understanding turbulence! When energy is added to a flow, this energy can only be dissipated in the bulk of the flow through viscous motion on the molecular scale leading eventually to a rise in temperature of the liquid. However, the large scale fluctuations at this point have no effect on these small scales. The large scale fluctuations or vortices have to break down to be

able to end up in the small sizes where viscous effects start to play a role in dissipation. This idea of an energy cascade was proposed by Richardson who stated that
1) Vorticity is created on large scales by some driving mechanism which feeds energy to the fluid.
2) Shear instability causes smaller vortices to be shed from the larger ones.
3) This process continues on smaller scales.
4) Until dissipation dampens the vortices and converts the kinetic energy into thermal energy.

Or stated in other words by Richardson:
Big whorls have little whorls
that feed on their velocity,
and little whorls have lesser whorls
and so on to viscosity.

Figure 1.4: Turbulence in the night sky by Vincent van Gogh

Apparently viscosity is an important factor in turbulent flows. Viscosity is best described as a liquids resistance to flow. One can visualize this best by having two plates parallel to each other with a liquid confined between these two plates. These plates are of infinite size, so no boundary effects to worry about and the bottom plate is fixed. If we start to move the top plate parallel to the bottom one, with the liquid in between, this will require a certain amount of force. The force needed to move the plates is proportional to the viscosity of the liquid. It might be intuitively clear that water must have a lower viscosity than for instance oil, or syrup. So, how easily can turbulent structures form?

This is quantified by the Reynolds number: the ratio between the inertial and viscous forces,

$$Re = \frac{UL}{\nu} \tag{1.1}$$

Here U is the flow velocity, L the typical length scale (the size of the channel for instance) and ν the kinematic viscosity. The higher the Reynolds number, the stronger the forcing on the fluid, and hence the stronger the turbulence. As a rough rule of thumb we can state that turbulence

starts to develop at a Reynolds number of ≈ 2300 for a channel flow.

1.2 Energy dissipation

If we go back to the example of the two plates moving parallel to each other with a liquid confined in between, there is some force exerted on the fluid, which causes the fluid to move. This force is counteracted by the viscous force. By calculating the so called drag force we can quantify this. The drag force on an obstacle is commonly written as

$$F_d = \frac{1}{2} C_d(Re) \rho U^2 A, \tag{1.2}$$

where C_d is the drag coefficient which is dependent on the Reynolds number, ρ is the density of the medium, U is the flow velocity, and A is the cross-sectional area.

This energy put in a flow must be dissipated and this happens with a certain rate: the energy dissipation rate ϵ. This is the amount of energy per second (or Power) per kilogram dissipated in the liquid. Here the work done per second is $F \times U$ while the mass of the body moving is $A \times L \times \rho$, assuming a fluid body of cross-sectional area A and length L.

In our example we get for the dissipation rate

$$\epsilon = \frac{FU}{\rho AL} = \frac{1}{2} C_d \frac{U^3}{L} \sim \frac{U^3}{L}. \tag{1.3}$$

So, the energy dissipation rate ϵ scales as $\frac{U^3}{L}$. It has the dimension $\frac{m^2}{s^3}$. Together with the viscosity ν and Reynolds number Re these three quantities are the prime factors in describing the nature of a turbulent flow. In this example we used the drag, but any measure of power holds, as long as it is dissipated in the flow.

1.3 Taylor-Couette Flow

The drag coefficient is of special interest as it is a quantification of how efficient a liquid is in dissipating energy, but doing research on infinite long plates is rather unpractical. Furthermore: the mass of the liquid under investigation has to be well known: we need to know how much power is put in what amount of liquid to get the energy dissipation rate.

An excellent setup to investigate the behavior of dissipation rate as a function of Reynolds number is a so called Taylor-Couette setup. This consists of two concentric cylinders, with a liquid confined in the gap between these two cylinders. We rotate one of the two cylinders and measure the resistive force of the liquid on the cylinders. Two concentric cylinders are a good approximation of the infinite long plates. The gap between the cylinders needs to be substantially smaller than the length of the cylinders to diminish the end wall effects and the radii of the two cylinders need to be large compared to the gap width, so it *behaves* like two parallel infinite plates at small scale.

By measuring the torque (or power) needed to rotate the inner cylinder at a certain rotation rate we can calculate at which velocity the flow is moving. Hence we can calculate the Reynolds number, and by knowing the torque, we know the power needed to reach that velocity, making it able to tell what the dependence of the torque (and so the energy dissipation rate) is on the Reynolds number. Here the Reynolds number is:

$$Re = \frac{UL}{\nu} = \frac{\Omega a(b-a)}{\nu}.$$

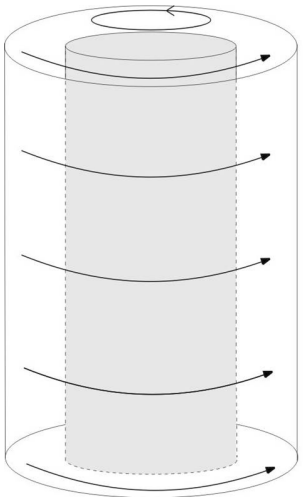

Figure 1.5: A typical Taylor-Couette cell, the inner cylinder is rotating with rotation rate Ω, the inner cylinder radius is a, the outer cylinder radius is b and fixed while the total cylinder height is H.

One can make an estimation on the dependence of torque on Reynolds by recalling that the energy dissipation is the total power divided by the mass which should be proportional the the velocity cubed divided by the typical length scale, so in this case

$$\epsilon \sim \frac{U^3}{L} = \frac{(\Omega a)^3}{b-a}.$$

What can we expect for the torque as a function of Reynolds number? One can derive this estimate by recalling that the total power in a Taylor-Couette setup is approximately the torque times the inner cylinder rotation rate which should equal the mass of the liquid times the energy dissipation rate:

$$
\begin{aligned}
P &= m\epsilon = T\Omega, \\
T\Omega &= \pi(b^2 - a^2)H\rho \cdot \frac{(\Omega a)^3}{b-a}, \\
T &= \pi(b+a)H\rho\Omega^2 a^3.
\end{aligned}
$$

We can now get an elegant solution in transforming the dimensional torque T to the non dimensional torque G

$$
\begin{aligned}
G &= \frac{T}{\nu^2 H\rho} = \frac{\pi(b+a)\Omega^2 a^3}{\nu^2} \\
&= \frac{\pi a(b+a)}{(b-a)^2} Re^2
\end{aligned}
$$

So, the torque G scales as Re^2 *assuming we have fully developed isotropic turbulence!* Regrettably, we do not. The boundary layers are smooth and there is a transition region from the wall where the fluid must have a relative low velocity in the frame of reference of the respective cylinder, due to the no-slip condition.

1.4 Guide through the Taylor-Couette part

In this thesis the first part is dedicated to the influence of the walls on the measured quantities in a Taylor-Couette cell. As the boundaries in Taylor-Couette are smooth, we expect a transition from the laminar boundary layer to a turbulent bulk flow. What would happen if we ruin the laminar boundary layer by roughening the walls and by doing so making the boundary layer more turbulent than it otherwise would be?

As will be shown in Ch. 2 the drag in such a system can be influenced quite drastically by roughening the cylinder walls, thus to effect the boundary layers. In subsequent chapters we investigate the effect of adding small bubbles in the Taylor-Couette setup. It is a well known effect that some small bubbles are able to drastically reduce the drag, of even up to 60% as compared to the no-bubble case, but why this occurs, is unknown. Its applications are obvious: if we would cover a hull of a ship

with small bubbles, it could possible save up to 60% of its fuel, leading to large savings, and environmental benefits. In Ch. 3 we try to find why these bubbles have drag reducing properties while in Ch. 4 we combine the two experiments to investigate if bubbles will still reduce the drag in a rough wall experiment, answering the question whether or not the observed drag reduction has its origin in the laminar boundary layer or in the turbulent bulk flow.

1.5 Kolmogorov's theory

The Taylor-Couette Setup is a great setup to investigate *global* properties: like the overall drag, while keeping the Reynolds number constant. However, we cannot get the influence of for instance bubbles on the energy cascade as the bubbles tend to accumulate near the inner wall due to the centrifugal forcing. For clear statements on the effect of bubbles on the energy cascade, one needs a different setup.

Andreii Kolmogorov was a Russian mathematician interested in stochastic processes. He extended his research later on to the motion of planets and the turbulent air jet from the exhaust of an air plane. In 1941, he published two papers following out of his research on the turbulent air jet which quickly showed to be of fundamental importance. These two papers are often called a magnificent piece of applied mathematical analysis. In short: he founded basically the mathematical analysis of turbulence.

As stated before, viscosity does not play a role until the last step in the cascade, where viscous forces dissipate the energy. So, we can define three different parts: the first is called the integral scale, where energy input into the flow is taking place (thus consisting of the largest structures). At the final stage the energy is dissipated and this range is consequently called the dissipative scale, consisting of the smallest structures of the flow. The section in between, the actual energy cascade part, is called the inertial regime. This is called a regime, as this is a range of different sized vortices.

Obviously, viscosity does not play a role until the vortices reach the dissipative scale. Therefore, in the inertial regime this energy cascade can only be depended on the length scale and the energy dissipation.

We define a wave number k for a vortex of length ℓ by $k = \frac{2\pi}{\ell}$. Kolmogorov's idea was that apparently this energy spectrum $E(k)$ only depends on the wave number for a certain sized vortex and the energy dissipation per unit volume, ϵ,

$$E(k) \propto \epsilon^{\alpha} k^{\beta}. \tag{1.4}$$

The dimension of energy spectrum E is $\frac{m^3}{s^2}$, the wave number k is $\frac{1}{m}$ and dissipation rate ϵ is $\frac{m^2}{s^3}$. Solving this for the α and β gives

$$E \propto \epsilon^{2/3} k^{-5/3}. \tag{1.5}$$

The beauty of this simple equation cannot be over-stressed. Apparently the energy cascades through the vortices via a powerlaw with exponent $-5/3$. This is still known as the Kolmogorov-41 theory, or more concise K-41.

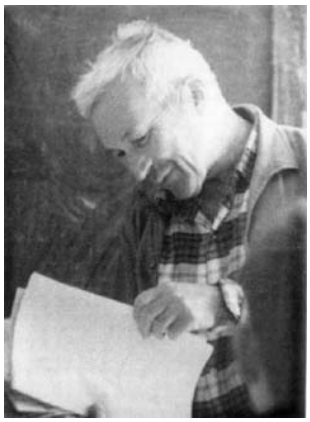

Figure 1.6: Andreii Kolmogorov.

Dimensional analysis can also be used to derive at what wave number the transfer to the dissipative regime actually takes place. In the dissipative regime, only the energy dissipation rate ϵ and the viscosity ν play a role. If so, we can derive by dimensional analysis at what wave number this takes place:

$$k_\eta \propto \epsilon^{\gamma} \nu^{\delta}. \tag{1.6}$$

Here k_η is the wave number at which the dissipative regime starts. As the dimension of k_η is $\frac{1}{m}$, of ν is $\frac{m^2}{s}$ and for the dissipation rate ϵ it is $\frac{m^2}{s^3}$ one finds as a solution

$$k_\eta \propto \epsilon^{1/4} \nu^{-3/4}. \tag{1.7}$$

Therefore, if we increase the viscosity ν, k_η will decrease, giving larger vortices who are able to dissipate their kinetic energy into thermal energy. This is to be expected: higher viscosity can dissipate larger vortices.

1.6 Energy Spectra

The energy cascade is a topic of a lot of research, especially what the effect of bubbles on the spectra will be. Are the turbulent spectra changed by the addition of bubbles in the flow? And if so, how? This kind of research cannot be done in a Taylor-Couette experiment, as the turbulence generated in it is by far not isotropic and homogenous. To investigate this

we used the so called Twente Water Tunnel which is depicted in Fig.1.6. This is a water tunnel with a measurement section of 2 meters high, and a surface of 0.45x0.45 meter. We use an active grid, consisting of square peddles placed on 24 rods which are rotating in double random mode: random in speed as well as direction of rotation. This way we are able to reach high Reynolds number homogenous isotropic turbulence.

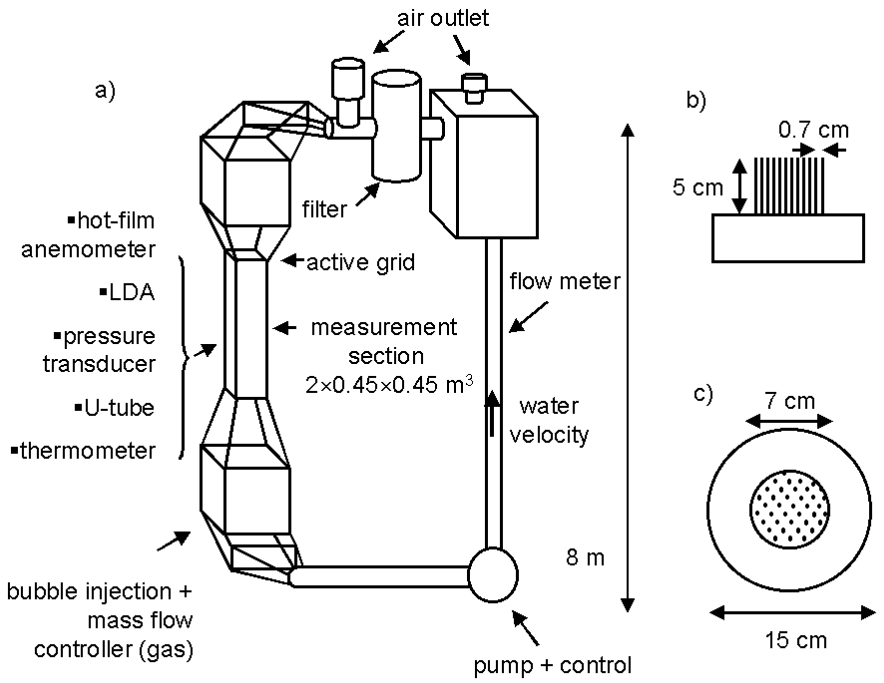

Figure 1.7: On the left a schematic picture of the Twente Water Tunnel, with the measurement section depicted and on the right the bubble islands used to inject the bubbles into the flow.

The velocity fluctuations in the water tunnel are measured by means of constant temperature anemometry (CTA). This involves a heated element which is kept constant in resistance, and hence temperature. By measuring the voltage over this element this can be linked directly to the heat flux from this element to the surrounding flow as a higher velocity will lead to a stronger cooling of the element, and hence a higher voltage is needed to keep the temperature constant. In Fig. 1.7 an example is given of the signal itself (in the inset) and the power spectra measured in this tunnel, clearly showing the inertial regime where the energy decays

via the $-5/3$ power law. Although CTA is a fast and accurate method, it is not measuring the actual flow speed, only the fluctuations. Therefore we have to calibrate the measured voltage. This is done by Laser Doppler Anemometry (LDA), which measures the Doppler Shift of laser light reflected by moving particles in the flow.

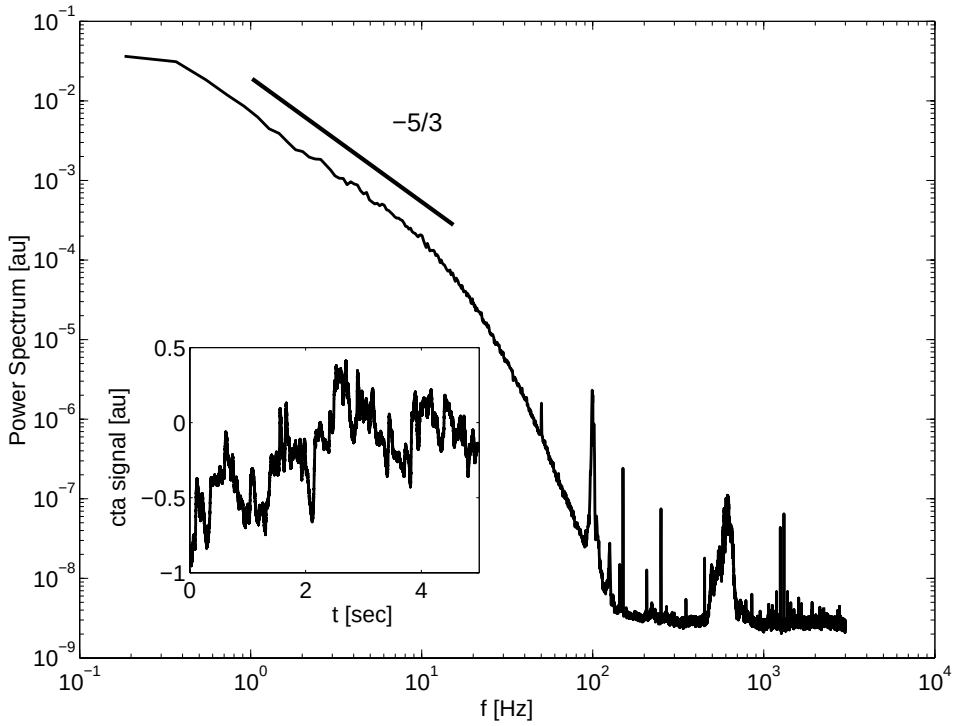

Figure 1.8: An example of the power spectrum versus frequency which clearly shows the inertial regime with the $-5/3$ behavior. In the inset a typical turbulent signal is shown.

This gives rise to the following problems: although the LDA gives clear and correct speeds of the flow, the data rate is too low to be able to make clear statistical statements on the energy spectrum of the flow, as a measurement can only be done whenever a particle is coincidentally moving through the focal field of the laser bundles. Furthermore: the medium has to have a clear field of view, so the datarate drops drastically in a two phase medium which makes the flow opaque.

The constant temperature anemometer on the other hand is a fast and precise way of measuring the qualitative properties of the flow, but not the actual flow velocities as one needs to calibrate. Furthermore: the bubble probe interactions are influencing the measurements and have to removed from the signal, making calibration cumbersome.

1.7 Guide through the Twente Water Tunnel Part

In the second part of the thesis, on the Twente Water Tunnel, we start with a summary of experiments, both numerically and experimentally. This can be found in Ch. 5. The effects of microbubbles on the turbulent spectra is discussed in Ch. 6. The numerical results given in Ch. 5 show bubble clustering due to the strong lift force present in the turbulent vortices. In Ch. 7 we verified if this behavior could be found in experimental conditions.
Some suggestions for improvement on the used experimental probes are found. A new probe is designed, combining an optical fibre and a conical hot film probe which is beneficial for removal of the bubble probe interactions from the signal. The specifications and working principles can be found in Ch. 8.

Finally, we summarize the conclusions in Ch. 9.

Part I

Taylor-Couette Flow

2

Smooth and rough boundaries in turbulent Taylor-Couette flow[§]

We examine the torque required to drive the smooth or rough cylinders in turbulent Taylor-Couette flow. With rough inner and outer walls the scaling of the dimensionless torque G is found to be consistent with pure Kolmogorov scaling $G \sim Re^2$. The results are interpreted within the Grossmann-Lohse theory for the relative role of the energy dissipation rates in the boundary layers and in the bulk; as the boundary layers are destroyed through the wall roughness, the torque scaling is due only to the the bulk contribution. For the case of one rough and one smooth wall we find that the smooth cylinder dominates the dissipation rate scaling, i.e., there are corrections to Kolmogorov scaling. A simple model based on an analogy to electrical circuits is advanced as a phenomenological organization of the observed relative drag functional forms. This model leads to a qualitative prediction for the mean velocity profile within the bulk of the flow.

2.1 Introduction

The relation between global transport properties and the external driving forces is the focus of interest for various turbulent flows. Examples include Rayleigh-Bénard convection where the heat flux is studied as a function of the temperature difference between top and bottom wall, pipe flow where the mean flow is studied as a function of the pressure drop, and Taylor-Couette flow where the required torque is studied as a function of the cylinder rotation speed. For many of these examples strict upper bounds exist (see e.g. refs. [1] for Rayleigh-Bénard flow or refs. [2] for

[§] see: Thomas H. van den Berg, Charles R. Doering, Daniel P. Lathrop, and Detlef Lohse, *Smooth and rough boundaries in turbulent Taylor-Couette flow*, Phys. Rev. E. **68**, 036307 (2003).

Taylor-Couette flow), but no exact calculation yields the flux-forcing dependence.

To better understand the relation between the global transport properties and the driving forces it is important to examine the role of the flow structure and boundary conditions. For Rayleigh-Bénard convection this has been done by employing rough boundary conditions [3–9] or by varying the aspect ratio or the Prandtl number [10–12]. Also for pipe flow the effect of rough boundary layers on the global transport efficiency has long been studied and parameterized in the roughness dependence of the skin friction coefficient [13, 14].

For Taylor-Couette flow the effect of two rough walls has been examined by Cadot *et al.* [15]. Their main finding is that the total energy dissipation rate ϵ scales as

$$\epsilon \sim \frac{U^3}{(b-a)}, \tag{2.1}$$

where b is the outer radius, a the inner radius, and U is the velocity of the inner cylinder. This rough-wall result is consistent with Kolmogorov's expectation of a residual dissipation at zero viscosity for fully developed turbulence [16], but in contrast to the smooth-wall result, where corrections to (2.1) are known to occur [17–19].

2.2 Experiments

2.2.1 Setup

The aim of the present study is to extend the results by Cadot *et al.* to the situation when only *one* of the cylinders is rough. Private communication with some knowledgable colleagues showed a lack of consensus on the answer to the following question: which boundary layer dominates the scaling, i.e., would the dissipation dependence show corrections to the Kolmogorov expectation (2.1) for one rough and one smooth wall? The analysis in [20] shows that the turbulent Kolmogorov scaling in (2.1) is an upper bound for smooth walls, but it can also be extended to prove that it is also a rigorous upper limit on ϵ for one rough and one smooth wall [21]. Hence this experimental question is also of interest to interpret the upper bound results.

One argument considered prior to our empirical results involved the fluctuations. The level of velocity fluctuations in the system might be set

by the boundary generating the largest disturbances. The resulting fluctuations would effect Reynolds stresses which would dominate the momentum transport, and therefore the dissipation. The rough wall would generate the largest level of the fluctuations, so this could be used to argue that it dominates in the overall behavior of the total dissipation of the system.

That view turns out to be empirically incorrect, which may be understood using the Grossmann-Lohse theory for the relative role of energy dissipation rate into the boundary layers and in the bulk. This theory has been developed for Rayleigh-Bénard convection [22–24], but also applied to Taylor-Couette and pipe flow [25]. The central idea is to split the total energy dissipation rate ϵ (and for the Rayleigh-Bénard case also the thermal dissipation rate) into a boundary layer (BL) and a bulk contribution,

$$\epsilon = \epsilon_{BL} + \epsilon_{bulk}. \tag{2.2}$$

The total energy dissipation rate ϵ in Taylor-Couette flow can be rigorously related with the dimensionless torque G, namely [19]

$$\epsilon = \frac{\nu^2 G \Omega}{\pi(b^2 - a^2)}. \tag{2.3}$$

Here $G = T/\rho\nu^2 L$ is the dimensionless torque, T the torque, ρ the fluid density, ν its kinematic viscosity, L the length of the cylinders, and Ω the angular rotation rate. The Reynolds number Re is defined as
$Re = \Omega a(b-a)/\nu$. Following ref. [22], the energy dissipation rate in the bulk is estimated as

$$\epsilon_{bulk} \sim \frac{U^3}{(b-a)} \tag{2.4}$$

and that in the BL as

$$\epsilon_{BL} \sim \nu \frac{U^2}{\lambda_u^2} \frac{\lambda_u}{b-a} \tag{2.5}$$

where $\lambda_u \sim (b-a)/\sqrt{Re}$ is the thickness of a laminar boundary layer assumed to be of Blasius-Prandtl type[†]. With these two estimates we obtain

$$G = c_1 Re^{3/2} + c_2 Re^2. \tag{2.6}$$

[†]Ref. [25] distinguishes between the imposed velocity U and the typical velocity difference U_w between the turbulent and the laminar (linear) profile, in order to better describe the experimental data. There a power law relation $U_w/U \sim Re^{\xi}$ was used, with a best fit of $\xi = -0.051$. Here, we drop this distinction and assume $U = U_w$, for simplicity and as $\xi = 0$ seems to satisfactorily describe the data.

Table 2.1: Results from a power law fit $G = cRe^{\alpha}$. In the last line we have fixed the exponent $\alpha = 2$.

case	c	α
ss	2.14	1.67
sr	0.79	1.81
rs	0.48	1.88
rr	0.21	2.08
rr'	0.57	2

The first term originates from contribution of the laminar boundary layers, the second one from that of the bulk. For the smooth-wall case, the Grossmann-Lohse theory accounts for the Rayleigh Ra (and Prandtl) number dependence of the experimentally found Nusselt Nu (and Reynolds) number for the Rayleigh-Bénard case. For the Taylor-Couette case, it also gives the Reynolds number dependence of the dimensionless torque G.

How do these considerations in convection extend to the rough-wall cases? In Rayleigh-Bénard flow, for large enough roughness and Ra, the laminar boundary layers are expected to break down and become turbulent. This results in the ultimate scaling regime, $Nu \sim Ra^{1/2}Pr^{1/2}$, in which the total dissipation rate scales soley with the dissipation rate in the bulk, due to the lack of laminar boundary layers [22]. The scaling exponent $1/2$ in the Ra-Nu dependence had been predicted earlier [26, 27] for thermal convection. The $1/2$ scaling exponent is also found [28] in numerical simulations in which the boundary layers have been eliminated and replaced by periodic boundary conditions. Rough-wall experiments on Rayleigh-Bénard convection by Roche *et al.* [9] also find a transition towards the $Nu \sim Ra^{1/2}$ scaling law, the upper bound result [1].

2.2.2 Results

For the rough-wall Taylor-Couette experiment the corresponding expectation is $G \sim Re^2$ for large enough roughness or Reynolds number, yielding again the upper bound result [2]. This has been observed experimentally by Cadot *et al.* [15]. More specifically, we expect the boundary layer influence to become relatively smaller when one of the walls is roughened. That is, the ratio of the bulk to boundary layer contributions to the energy dissipation rate should increase and this is observed in the data.

Table 2.2: Results from a linear regression of to the experimental data of $G/Re^{3/2} = c_1 + c_2 Re^{1/2}$. *In the last line we have enforced* $c_1 = 0$. *In the second but last line there is hardly any contribution from the laminar BL, so* c_1 *gets an ill-defined value.*

case	c_1	c_2	$\epsilon_{bulk}(10^5)/\epsilon_{BL}(10^5)$
ss	6.69	0.02	0.95
sr	14.10	0.05	1.11
rs	12.40	0.10	2.55
rr	-12.80	0.76	-18.80
rr'	0	0.57	∞

The experimental apparatus consists of a rotating inner cylinder, of radius $a = 16$ cm, and a stationary outer cylinder of radius $b = 22$ cm, yielding a radius ratio of $\eta = a/b = 0.73$. The height of the gap was $L = 69.5$ cm, giving an aspect ratio of $\Gamma = L/(b-a) = 11.6$. The inner cylinder was especially instrumented to measure the torque on a 40.64 cm central section using strain gauges. This apparatus is described in more detail in references [17, 19]. Our measurements span a Reynolds number, $Re = \Omega a(b-a)/\nu$, range of $10^4 < Re < 10^6$, where Ω is the inner cylinder rotation rate. Three fluids were used; water and water-glycerin mixtures of viscosities $\nu = 0.01, 0.10$, and 0.26 cm^2/s respectively. Either the inner, the outer, or both of the cylinders were roughened by attaching 16 vertical strips of square cross-section (0.3 cm on edge) which were equally spaced in azimuthal angle, similar to the procedure used in [15].

Four cases are analyzed: (ss) smooth inner and outer wall, (sr) smooth inner and rough outer wall, (rs) rough inner and smooth outer wall, and (rr) rough inner and outer wall. The maximum rotation rate achieved in each case was determined approximately by the available motor torque.

Figure 2.1a shows G vs. Re for the four cases. Fitting a power law

$$G = cRe^{\alpha} \tag{2.7}$$

gives the exponents shown in table 2.1. It is clearly seen that the approximate power law exponent α increases with the roughness of the walls and is consistent with $\alpha = 2$ in the rr-case.

The alternative way to represent the data is that according to the Grossmann-Lohse theory, namely $G/Re^{3/2}$ vs $Re^{1/2}$, see Fig. 2.2. From a linear regression to those data the coefficients c_1 and c_2 of Eq. (2.6) can directly

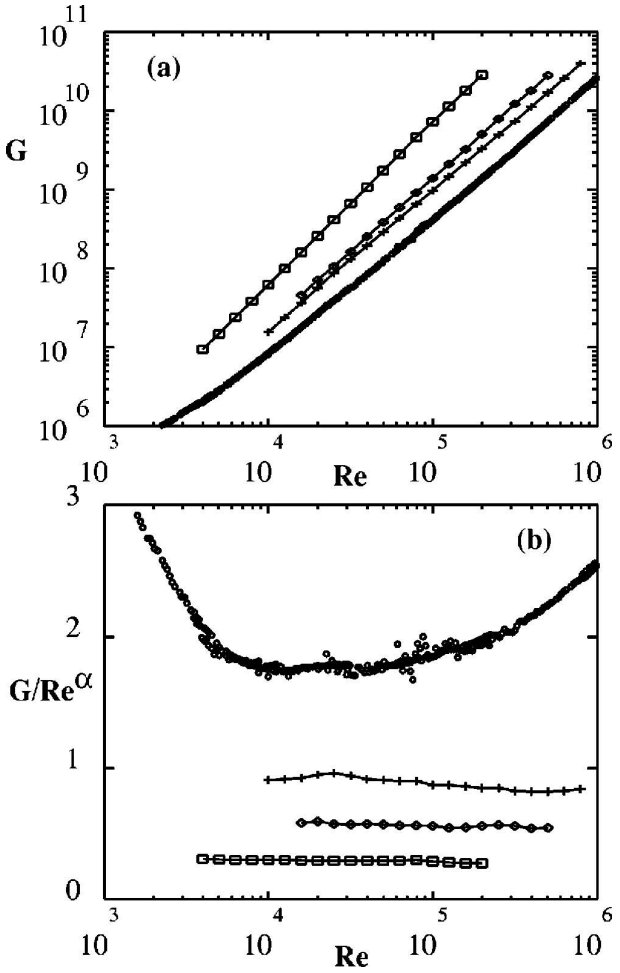

Figure 2.1: (a) The dimensionless torque $G = T/\rho\nu^2 L$ shows a dependence on Reynolds number (dimensionless forcing $R = \Omega a(b-a)/\nu$) close to Kolmogorov scaling $G \sim R^2$. The four cases shown differ on the condition of the cylinders: ∘ (ss) both cylinders smooth; + (sr) smooth inner, rough outer; ⋄ (rs) rough inner, smooth outer; and □ (rr) both walls rough. The deviations from that scaling indicate the importance and structure of the boundary layers. (b) Compensated plots G/Re^{α} dependence on Reynolds number.

be obtained, see table 2.2. The expectation discussed above that ratio of the laminar BL contribution $c_1 Re^{3/2}$ and the turbulent bulk contribution $c_2 Re^2$ becomes less when one wall is roughened and becomes close to

zero when both walls are roughened is observed. As for the rr-case the laminar BLs should be completely vanished for large enough Re number, we also tried the one-parameter fit $G = c_2 Re^2$ which well describes the data.

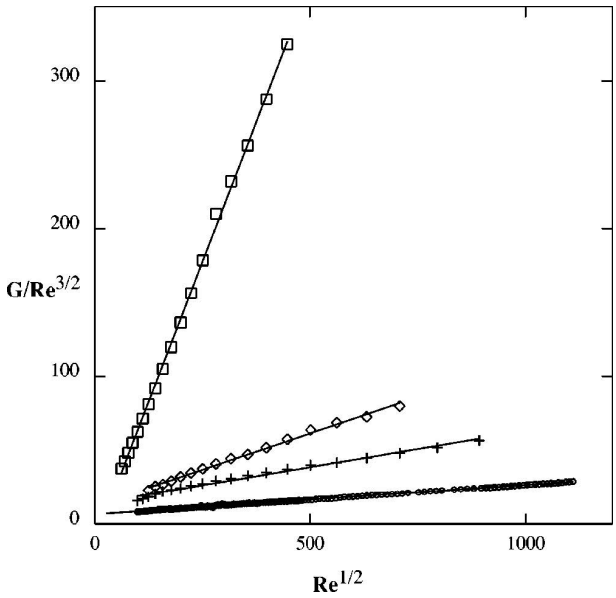

Figure 2.2: A test of the scaling prediction Eq. 6; $G/Re^{3/2}$ vs $Re^{1/2}$ for the four case (∘) ss, (+) sr, (◇) rs, and (□) rr, bottom to top. A linear regression to these data gives the coefficients c_1 and c_2 in Eq. (2.6) as shown in Table 2.2.

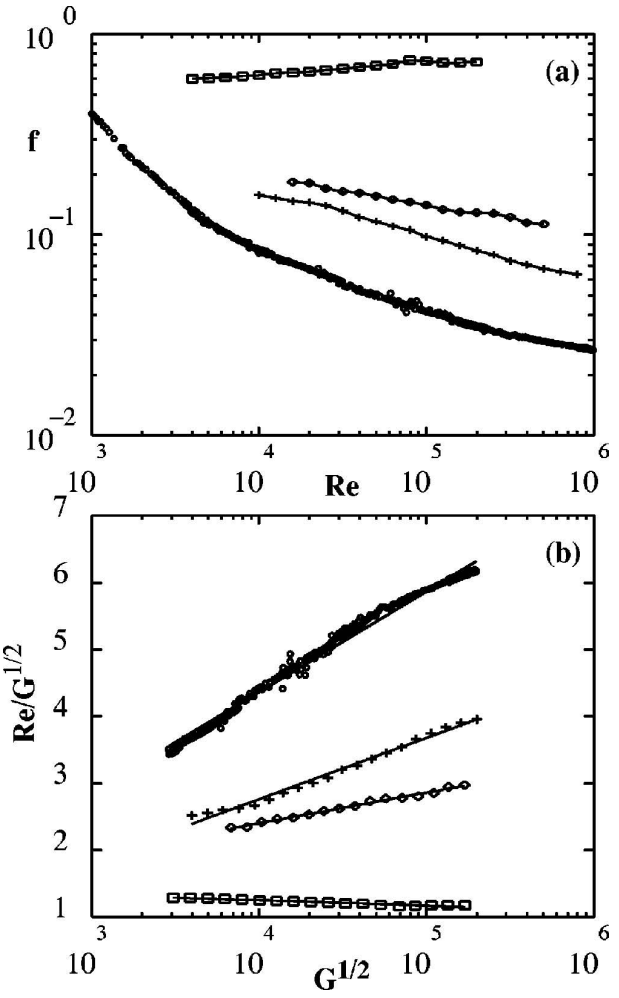

Figure 2.3: (a) Skin friction coefficient f vs Reynolds number Re for the four cases ($\circ$) ss, ($+$) sr, ($\diamond$) rs, and ($\square$) rr, bottom to top. For the ss-case the data are well described by the skin friction law (2.8) (solid line, see also table 2.3), as extensively discussed in refs. [17–19]. In the rr-case f becomes independent of Re for large enough Re. The cases rs and sr with one rough wall only are in between these these extreme cases. Due to the persistence of one smooth wall and the corresponding boundary layer f still depends on Re for large Re. (b) Same data as in (a), but now plotted as $1/\sqrt{f} = Re/\sqrt{G}$ vs $\log_{10}(Re\sqrt{f})$. If Eq. (2.8) is right, this type of plot results in a straight line.

Table 2.3: Results from fitting the Prandtl-von Karman friction law (2.8) to the experimental data. The cases with rough walls has the largest error in the fit, as this model is least suitable for that case.

case	c_1'	c_2'	fit error
ss	1.51	-1.66	0.01
sr	0.92	-0.92	0.01
rs	0.46	0.58	0.01
rr	-0.08	1.57	0.05

We also test the Prandtl-von Kármán skin friction law for this data. For the friction coefficient $f = G/Re^2$ it holds for smooth boundaries [13, 18, 19, 25]

$$\frac{1}{\sqrt{f}} = c_1' \log_{10}(Re\sqrt{f}) + c_2'. \tag{2.8}$$

The two constants c_1' and c_2' can be connected to the von Kármán constant [19]. This friction law (2.8) well fits the data for the ss-case (see Fig. 2.3). For the case with rough walls a roughness lengthscale must be introduced, see section 7.2 of [14]. For large enough roughness and large enough Re the skin friction coefficient f then becomes independent of the Reynolds number, as indeed observed from Fig. 2.3a.

2.3 Momentum Model

How can one rationalize the observed dependencies of the torques in the four different cases (rr, sr, rs, and ss)? We have attempted to do so by employing a circuit analogy. The torque, and therefore dissipation, is determined by the flux of angular momentum transported radially through the fluid from the inner cylinder to the outer cylinder. The conserved quantity is the torque, i.e., the torque on both cylinders—or through any concentric cylinder in between—is the same. This is analogous to the current in a series circuit, where the resistors are analogous to the boundary layers. The smooth boundaries are poor conductors (or large resistors) for angular momentum relative to rough walls. In this analogy, it is clear that the larger resistance dominates the total resistance in a series circuit.

The implication is that the smooth wall sustains a relatively large angular momentum gradient while only communicating a relatively small

torque. Those cases with one rough and one smooth wall should therefore have the fluid coupling strongly to the rough wall whether it is rotating or not. The angular velocity (say at mid gap) would be biased toward the rough wall relative to the smooth-smooth case. Although we did not observe the mean angular velocity in this experiment, this hypothesis could be tested in future experiments.

The circuit analogy leads to a simple analytical model for the coupling of multiple boundaries in series. We propose a hydrodynamic Ohms' law:

$$Z(R)T = \Delta U \tag{2.9}$$

where the velocity difference ΔU designates the (angular) momentum drop across the layer, T the communicated torque, and Z the impedance of the boundary layer. The impedance Z depends not only on the Reynolds number, but also on the nature, smooth or rough, of the wall. We then calculate the total velocity drop between cylinders as the drop across the inner boundary layer plus the drop across the outer boundary layer, ignoring any core region:

$$\Delta U_{in} + \Delta U_{out} = \Delta U_{total} \tag{2.10}$$

so that

$$TZ_{in}(R) + TZ_{out}(R) = TZ_{total}(R). \tag{2.11}$$

The torques are equal between the two layers so we obtain $Z_{total} = Z_{in} + Z_{out}$ as in series resistances.

The characteristic impedances of the outer and inner boundaries would be different, even if both smooth or rough, due to geometric differences. Still, we can test this hypothesis of additive impedances by examining the four cases:

$$Z_{ss} = Z_{s,inner} + Z_{s,outer}, \tag{2.12}$$

$$Z_{sr} = Z_{s,inner} + Z_{r,outer}, \tag{2.13}$$

$$Z_{rs} = Z_{r,inner} + Z_{s,outer}, \tag{2.14}$$

$$Z_{rr} = Z_{r,inner} + Z_{r,outer}. \tag{2.15}$$

These four equations result in the two expressions which contain measurable quantities only, namely

$$Z_{ss} + Z_{rr} = Z_{rs} + Z_{sr} \tag{2.16}$$

and

$$Z_{rr} - Z_{ss} = Z_{rs} - Z_{sr}. \tag{2.17}$$

These relationships indicate how the rough and smooth boundary layers may be combined in arbitrary series circuits of momentum transfer if the involved impedances are known. Note that expression (2.17) would even hold *with* the bulk contribution to the impedance in Eqs. (2.10) to (2.15), as this bulk contribution would cancel out.

We test the relationships in Eqs. (2.16) and (2.17) with the experimental data in Fig. 2.4. We plot the ratios of the lhs and the rhs of these equations. The ratio of the sums $(Z_{rs} + Z_{sr})/(Z_{ss} + Z_{rr})$ falls less than 10% below the theoretical expection 1 over nearly three orders of magnitude in the Reynolds number. The residuals show a deviation diminishing at higher Reynolds numbers (smaller total impedances) possibly indicating that some communication between the boundary layers is not captured in this simple model. The ratio of the difference $(Z_{rs} - Z_{sr})/(Z_{rr} - Z_{ss})$ is increasing with Re, but still is about a factor of five smaller than 1, showing quantitative shortcomings of our simplistic model.

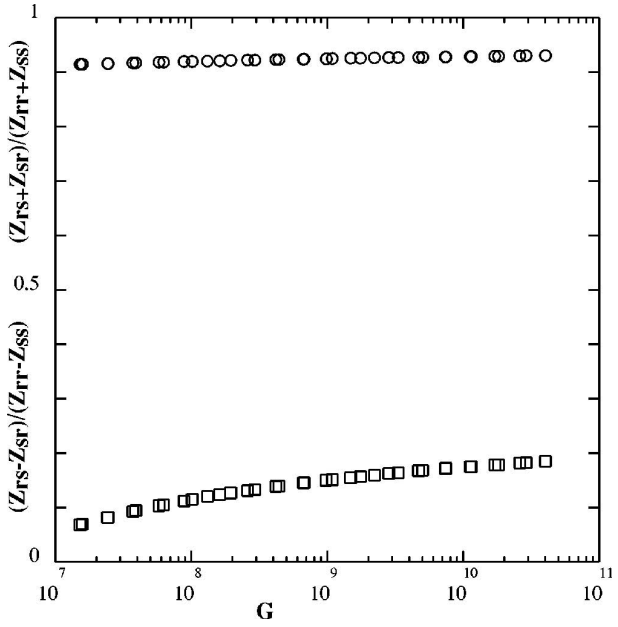

Figure 2.4: A test of the impedance model for the boundary layers. $(Z_{rs} + Z_{sr})/(Z_{rr} + Z_{ss})$ *and* $(Z_{rs} - Z_{sr})/(Z_{rr} - Z_{ss})$ *vs.* G*. Both ratios would be one if the impedence model would exactly work. The data used for this test comes from the fitted Prandtl-von Kármán forms shown in Fig. 2.3 (as data are needed at precisely the same Torques for each case).*

Nevertheless, this circuit analogy could be used to make predictions for systems with different combinations of rough and smooth walls where the momentum must pass through a series of such boundary layers. One could even extend the model to make predictions about nested cylindrical systems, whose interior cylinders could rotate freely. How this model could be extended to systems with the momentum passing through heterogeneous boundary layers in parallel is uncertain—and would likely only be possible in quite simple geometric situations.

2.4 Conclusion

In conclusion, we have measured the Reynolds number dependence of the dimensionless torque G in turbulent Taylor-Couette flow with rough walls, finding $G \sim Re^2$ which corresponds to the strict upper bound result [2]. The results for the four examined cases of rough (r) and smooth (s) walls; ss, sr, rs, and rr. The data are interpreted within the Grossmann-Lohse theory, strengthening the analogy between Taylor-Couette and Rayleigh-Bènard flow (also explored for turbulent flows in [29]). Perhaps surprisingly, we conclude that it is the smoothest wall that dominates the observed scalings, acting as the rate limiting step for momentum transfer.

References

[1] L.N. HOWARD, *Heat transport by turbulent convection*, J. Fluid Mech. 17, 405-432 (1963);
C.R. DOERING AND P. CONSTANTIN, *Variational bounds on energy dissipation in incompressible flows. III. Convection.*, Phys. Rev. E 53, 5957 (1996).

[2] L.N. HOWARD, *Bounds on flow quantities.*, Ann. Rev. Fluid Mech. 4, 473 (1972);
C.R. DOERING AND P. CONSTANTIN, *Variational bounds on energy-dissipation in incompressible flows - shear-flow*, Phys. Rev. E 49, 4087 (1994).

[3] Y. SHEN, P. TONG, AND K.-Q. XIA, *Turbulent convection over rough surfaces*, Phys. Rev. Lett. **76**, 908 (1996).

[4] K.-Q. XIA AND S.-L. LUI, *Turbulent thermal convection with an obstructed sidewall*, Phys. Rev. Lett. **79**, 5006 (1997).

[5] Y. B. DU AND P. TONG, *Enhanced heat transport in turbulent convection over a rough surface*, Phys. Rev. Lett. **81**, 987 (1998).

[6] Y. B. DU AND P. TONG, *Turbulent thermal convection in a cell with ordered rough boundaries*, J. Fluid Mech. **407**, 57 (2000).

[7] Y. B. DU AND P. TONG, *Temperature fluctuations in a convection cell with rough upper and lower surfaces*, Phys. Rev. E **63**, 046303 (2001).

[8] S. CILIBERTO AND C. LAROCHE, *Random roughness of boundary increases the turbulent convection scaling exponent*, Phys. Rev. Lett. **82**, 3998 (1999).

[9] P. E. ROCHE, B. CASTAING, B. CHABAUD, AND B. HEBRAL, *Observation of the 1/2 power law in Rayleigh-Bènard convection*, Phys. Rev. E **63**, 045303 (2001).

[10] G. AHLERS AND X. XU, *Prandtl-number dependence of heat transport in turbulent Rayleigh-Bènard convection*, Phys. Rev. Lett. **86**, 3320 (2001).

[11] K.-Q. XIA, S. LAM, AND S. Q. ZHOU, *Heat-flux measurement in high-Prandtl-number turbulent Rayleigh-Bènard convection*, Phys. Rev. Lett. **88**, 064501 (2002).

[12] R. VERZICCO AND R. CAMUSSI, *Prandtl number effects in convective turbulence*, J. Fluid Mech. **383**, 55 (1999).

[13] L. D. LANDAU AND E. M. LIFSHITZ, *Fluid Mechanics*, Pergamon Press, Oxford (1987).

[14] S. B. POPE, *Turbulent Flow*, Cambridge University Press, Cambridge (2000).

[15] O. CADOT *et al.*, *Energy injection in closed turbulent flows: Stirring through boundary layers versus inertial stirring*, Phys. Rev. E **56**, 427 (1997).

[16] U. FRISCH, *Turbulence*, Cambridge University Press, Cambridge (1995).

[17] D. P. LATHROP, J. FINEBERG, AND H. L. SWINNEY, *Turbulent-flow between concentric rotating cylinders at large Reynolds number*, Phys. Rev. Lett. **68**, 1515 (1992).

[18] D. P. LATHROP, J. FINEBERG, AND H. L. SWINNEY, *Transition to shear-driven turbulence in Couette-Taylor flow*, Phys. Rev. A **46**, 6390 (1992).

[19] G. S. LEWIS AND H. L. SWINNEY, *Velocity structure functions, scaling, and transitions in high-Reynolds-number Couette-Taylor flow*, Phys. Rev. E **59**, 5457 (1999).

[20] C.R. DOERING AND P. CONSTANTIN, *Energy-dissipation in shear driven turbulence*, Phys. Rev. Lett. **69**, 1648 (1992).

[21] P. CONSTANTIN AND C.R. DOERING, unpublished.

[22] S. GROSSMANN AND D. LOHSE, *Scaling in thermal convection: a unifying theory*, J. Fluid. Mech. **407**, 27 (2000).

[23] S. GROSSMANN AND D. LOHSE, *Thermal convection for large Prandtl numbers*, Phys. Rev. Lett. **86**, 3316 (2001).

[24] S. GROSSMANN AND D. LOHSE, *Prandtl and Rayleigh number dependence of the Reynolds number in turbulent thermal convection*, Phys. Rev. E **66**, 016305 (2002).

[25] B. ECKHARDT, S. GROSSMANN, AND D. LOHSE, *Scaling of global momentum transport in Taylor-Couette and pipe flow*, Eur. Phys. J. B **18**, 541 (2000).

[26] R. H. KRAICHNAN, *Turbulent thermal convection at arbitrary Prandtl number*, Phys. Fluids **5**, 1374 (1962).

[27] E. A. SPIEGEL, *Convection in stars 1. Basic Boussinesq convection*, Ann. Rev. Astron. Astrophys. **9**, 323 (1971).

[28] D. LOHSE AND F. TOSCHI, *Ultimate state of thermal convection*, Phys. Rev. Lett. **90**, 034502 (2003).

[29] B. DUBRULLE AND F. HERSANT, *Momentum transport and torque scaling in Taylor-Couette flow from an analogy with turbulent convection*, Eur. Phys. J. B. **26**, 379 (2002).

3

Drag reduction in Taylor-Couette Turbulence §

In Taylor-Couette flow the total energy dissipation rate and therefore the drag can be determined by measuring the torque on the system. We do so for Reynolds numbers between $Re = 7 \cdot 10^4$ and $Re = 10^6$ after having injected (i) small bubbles ($R = 1mm$) up to a volume concentration of $\alpha = 5\%$ and (ii) buoyant particles ($\rho_p/\rho_l = 0.14$) of comparable volume concentration. In case (i) we observe a crossover from little drag reduction at smaller Re to strong drag reduction up to 20% at $Re = 10^6$. In case (ii) we observe at most little drag reduction throughout. Several theoretical models for bubbly drag reduction are discussed in view of our findings.

3.1 Introduction

While turbulent drag reduction by polymers has fascinated the physics community for some time [1–4], it is less known that also a relatively small amount of bubbles can considerably reduce the drag [5–8]. This drag reduction method is feasible in application to ships [9]. For example, in ref. [5] 80% drag reduction was achieved by injecting micro bubbles in the turbulent boundary layer of a submerged body. Under more realistic conditions for ships, drag reduction of about 32% has been achieved [10]. This could lead to substantial fuel saving for commercial ships.

While it is understood that the drag reduction effect is due to the modification of the turbulent boundary layer through the bubbles, a detailed and accepted explanation of the effect is lacking. Recently, numerical simulations succeeded in qualitatively reproducing drag reduction [11–

§See: Thomas H. van den Berg, Stefan Luther, Daniel P. Lathrop, and Detlef Lohse, *Drag reduction in Taylor-Couette Turbulence*, Phys. Rev. Let. **94**, 044501 (2005).

15]. From these simulations several different theoretical explanations of the effect arose: Ferrante and Elghobashi [12] performed a simulation with point bubbles (corresponding to a bubble radius of $R_b \simeq 3.2 \cdot 10^{-3} y_0$) in a turbulent boundary layer (of inner length scale y_0). The inhomogeneous bubble distribution leads to an *effective compressibility* of the flow which induces an enhanced average flow off the wall. This flow pushes the dissipative structures further away from the wall, leading to a net drag reduction. This suggested mechanism gets less effective for larger bubbles (at given volume concentration α). Xu et al. [11] found in DNS for relatively large bubbles and void fractions up to 8% a transient drag reduction as bubbles disperse into the flow. Sugiyama et al. [15] extended the model of ref. [11], but found skin friction *enhancement* for rigid bubbles. Only by allowing for bubble deformation within a front-tracking scheme [16] a skin friction reduction up to 3% was found at *large* Reynolds numbers, whereas at small Reynolds number the drag was again enhanced [15]. Also Lu et al. [13] did simulations with up to 16 *deformable* and much larger bubbles than employed in ref. [12] (54 wall units diameter) in a 'minimal turbulent channel' ($Re = 4000$), again employing the front tracking technique [16]. They find that the deformable bubbles approaching the wall push high vorticity regions away from the wall, which leads to less drag. In their simulations Lu *et al.* [13] find drag reduction up to 15%. In contrast, non-deformable buoyant particles of equal size and buoyancy ratio as the bubbles can lead to a drag enhancement [13, 15]. Note that within the Ferrante-Elghobashi picture buoyant micro particles with the same density ratio as bubbles would also lead to drag reduction, as they imply an effective compressibility, too.

In order to shed more light on the issue of turbulent drag reduction, we performed experiments in turbulent bubble and buoyant particle Taylor-Couette flow. One advantage of the Taylor-Couette system is that statistical stationary states can be achieved easily. The second advantage of Taylor-Couette flow is that it is a *closed flow* system for which exact global energy balances hold. The total dissipation rate ϵ can directly be measured by measuring the required torque T on the system (to keep the inner cylinder at constant velocity), namely,

$$\epsilon = \frac{T\Omega}{\pi\rho L(b^2 - a^2)} = \frac{\nu^2 G\Omega}{\pi(b^2 - a^2)}, \tag{3.1}$$

where $G = T/\rho\nu^2 L$ is the dimensionless torque, $\rho = \rho_0(1-\alpha)$ the fluid density of the bubbly liquid, ρ_0 the fluid density of water, L the length of the cylinders, a, and b inner and outer cylinder radius, respectively, and

Ω the angular rotation rate. The kinematic viscosity ν is for the bubbly liquid, which we assume follows [17]

$$\nu = \nu_0(1 + \frac{5}{2}\alpha) \tag{3.2}$$

with ν_0 the viscosity of water. The relation (3.2) holds for small gas volume fractions and becomes more and more questionable for larger α, as discussed e.g. in ref. [18]. Here the relation (3.2) is only needed to define the flow Reynolds number as $Re = \Omega a(b-a)/\nu$.

To quantify the drag we take the drag coefficient which is the dimensionless energy dissipation rate $c_\epsilon = \epsilon(b-a)/U^3 = T/(\pi\rho L a^3(b+a)\Omega^2)$, where $U = a\Omega$ is the velocity of the inner cylinder. Note that the drag coefficient c_ϵ follows directly from the measured torque T and Ω, without making any assumption on the viscosity ν of the bubbly flow.

3.2 Experimental Setup

The experimental setup consists of a rotating inner cylinder of radius $a = 16cm$ and a stationary outer cylinder of radius $b = 22cm$. The total length of the inner cylinder is $L = 69.5cm$ giving an aspect ratio $\Gamma = L/(b-a) = 11.6$. The inner cylinder consists of three parts, with the torque measured on the middle part of the inner cylinder. The torque on the middle section is measured using strain gauges. The basic experimental setup is discussed in more detail in refs. [19–21]. Bubbles are injected by eight needles located at the lower part of the outer cylinder. The bubble size is dictated by the shear in the setup with stronger shear favoring slightly smaller bubbles [22]. Typical bubble diameters are between 0.5mm and 2mm. The typical boundary layer inner length scale is much smaller, $y_0 = \nu/u_* \approx 3\mu m$ with $u_* = \sqrt{\tau_w/\rho}$. Here, as in ref. [19], we have estimated τ_w as $\tau_w = T/2\pi a^2 L$.

An outlet is attached to the top plate which leads to an expansion barrel. By simultaneous measuring the weight difference (therefore volume difference) of the barrel, we are able to measure the volume averaged void fraction α of the setup, as injecting bubbles in the flow forces liquid to flow out on top.

For several constant Reynolds numbers we increased the void fraction and measured the torque on the inner cylinder as well as the rotation rate of the inner cylinder and the void fraction. Our Reynolds number range spans $7 \cdot 10^4 < Re < 10^6$ which is limited by the maximum available torque of the motor.

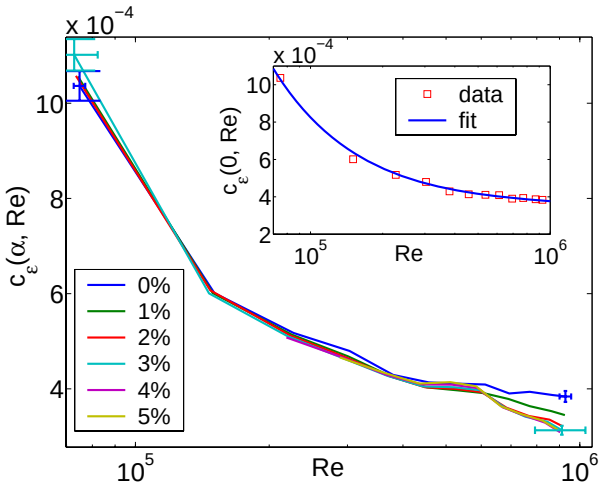

Figure 3.1: The drag coefficient $c_\epsilon(\alpha, Re)$ for volume concentrations α up to 0.05. The error bars in this and the subsequent figures result from an estimated relative error of 1% in the electronically controlled Ω and in T, and from an estimated absolute error of 0.5% for α. For clarity, error bars are only given for the first and the last data points of each curve. The inset shows $c_\epsilon(\alpha = 0, Re)$ for the single phase flow case ($\alpha = 0$) together with its fit Eq. (3.3) which nicely described the measured data. The fit parameters are $\beta = 3000$ and $c_{\epsilon,\infty} = 3.4 \cdot 10^{-4}$.

3.3 Results

3.3.1 Drag measurements with bubbles

In Fig. 3.1 we show the drag coefficient c_ϵ versus Re for various bubble volume concentrations α up to 5%. We see from Fig. 3.1 that the drag coefficient *decreases* for increasing α. To be able to better compare the drag coefficients $c_\epsilon(\alpha, Re)$ and $c_\epsilon(\alpha = 0, Re)$, we plot their *ratio* as function of Re in Fig. 3.2. Rather than using the individual data points $c_\epsilon(\alpha = 0, Re)$, the ratio is calculated by first fitting the data points for $c_\epsilon(\alpha = 0, Re)$ to [23]

$$c_\epsilon^{fit}(\alpha = 0, Re) = c_{\epsilon,\infty} \left\{ \left(\frac{3\beta^3}{8} \right)^{1/2} \frac{1}{Re} + \sqrt{1 + \frac{3\beta^3}{8} \frac{1}{Re^2}} \right\}, \tag{3.3}$$

and then calculating the ratio as $c_\epsilon(\alpha, Re)/c_\epsilon^{fit}(\alpha = 0, Re)$, which reduces the systematic error. The drag coefficient parametrization (3.3) had been

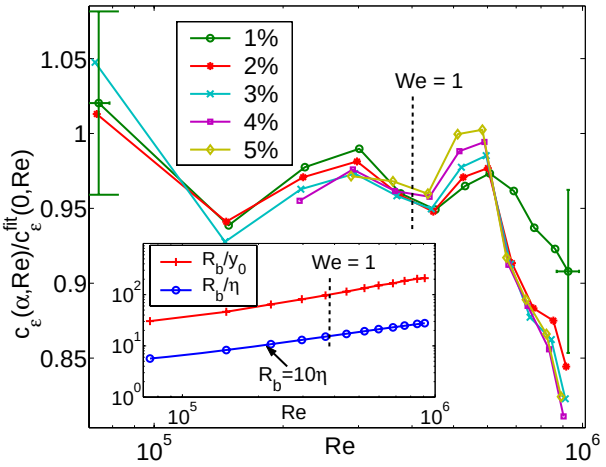

Figure 3.2: Ratio $c_\epsilon(\alpha, Re)/c_\epsilon^{fit}(0, Re)$ vs. Re for $0 \leq \alpha \leq 0.05$. The inset shows the ratios R_b/η (lower) and R_b/y_0 (upper) as function of Re.

suggested in ref. [23] as a crossover function from the viscous to the inertial regime. As seen from the inset of Fig. 3.1 the experimental data for $c_\epsilon(\alpha = 0, Re)$ are well described by this fit. For the physical meaning of the fit parameters β and $c_{\epsilon,\infty}$ we refer to ref. [23].

From Fig. 3.2 we can identify two regimes: a regime up to $Re \sim 6 \cdot 10^5$ with very little drag reduction of a few percent, and beyond that a regime of considerable drag reduction up to 20%. This is considerable for the relatively small volume concentration and presumably cannot be explained as a bulk effect because the mass change is at most only 5%. We therefore conclude that the bubbles indeed modify the turbulent boundary layers, as generally assumed [†].

To obtain some understanding of the crossover behavior observed in Fig. 3.2, we calculate how the Weber number $We = \rho u'^2 R_b/\sigma$ depends on the Reynolds number. Here, We is based on the velocity fluctuations $u' = ia\Omega$, where i is the turbulent intensity. We thus get

$$We = \frac{\rho}{\sigma}\frac{\nu^2 R_b}{(b-a)^2} i^2 Re^2 \approx 2 \cdot 10^{-9} i^2 Re^2, \tag{3.4}$$

with $\nu = 8 \cdot 10^{-7} m^2/s$, $\rho = 1000 kg/m^3$, $\sigma = 0.072 N/m$ (all for $30^o C$), and

[†]Note that in contrast the reduction of the energy dissipation rate observed in the numerical simulations of homogeneous turbulence [24] of course *is* a bulk effect. This is at most a 4% effect, comparable to the bubble volume concentrations in those simulations.

$R_b \approx 0.5$mm as it applies in our experiments. For the large $Re = 10^5$ – 10^6 $i \approx 0.06$ [20]. Eq. (3.4) thus predicts that the crossover from $We < 1$, where the bubbles are mainly spherical, to $We > 1$, where the bubbles are deformed, takes place at $Re_{We=1} \approx 4 \cdot 10^5$, very close to the observed transition in Fig. 3.2.

We also calculate the Kolmogorov length $\eta = \nu^{3/4}/\epsilon^{1/4}$ and y_0 and compare them with the typical bubble size, see inset of Fig. 3.2. Note that the given length scales η and y_0 can only be *averaged* lengths scales as their calculation is based on a global quantity (namely the torque); they in fact may depend on the position in the flow. In any case, one can judge from the inset of Fig. 3.2 that in the small Re regime $R_b \simeq 5\eta$, i.e., the flow around the bubble is smooth and the bubble indeed can be more or less spherical. In the large Re regime however $R_b \gg 10\eta$, and the bubbles can considerably deform and wobble.

We interpret the small Re regime with $We < 1$ as a regime in which the drag reduction mechanism suggested by Ferrante and Elghobashi [12] is dominant, namely, effective compressibility. For a given volume fraction this mechanism is most efficient for small bubbles. Since here our bubbles are large as compared to the tiny bubbles used in the Ferrante and Elghobashi simulations, we have only a small drag reduction effect. In the large Re regime with $We > 1$ however the dominant drag reduction effect seems to be the bubble deformability, as suggested by Lu et al. [13] and Sugiyama et al. [15]. For the large bubbles employed in this regime, the drag reduction indeed can be considerable, just as observed in our experiments.

3.3.2 Drag measurements with particles

To test this interpretation and to get more experimental information to either validate or falsify the theories on drag reduction, we repeated the torque measurements for turbulent Taylor-Couette flow, but now after having injected buoyant *particles* rather than bubbles. We took hollow glass spheres (Q-Cel hollow spheres from 'PQ corporation' [†]) with a mean radius of $R_p = 85\mu m$ and an effective density of $\rho_p/\rho_l = 0.14$. The result for the drag coefficient c_ϵ is shown in Fig. 3.3. We find that for *small* Re the (small) drag reduction is within error bars the same as for bubbly flow. For *large* Re however there is no drag reduction whatsoever for the buoyant particles. This finding is consistent with our above interpretation, as

[†] www.pqcorp.com

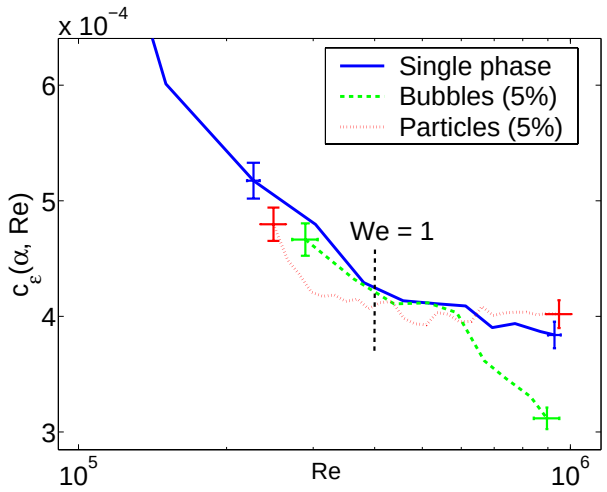

Figure 3.3: Drag coefficient $c_\epsilon(\alpha, Re)$ vs Re for single phase flow (solid), bubbly flow with $\alpha = 0.05$ (dashed), and buoyant particle flow with $\alpha = 0.05$ (dotted).

buoyant particles should show the drag reduction effect due to the effective compressibility [12], but not the one due to deformability [13, 15]. For large Re the drag coefficient is even slightly enhanced (see Fig. 3.3). This may be in accordance with Lu et al.'s [13] and Sugiyama et al.'s [15] predictions or it may be an effect due to the finite inertia of the particles, which have distinctively nonzero mass ($\rho_p/\rho_l = 0.14$) and which could counteract the effective compressibility drag reduction effect. To what degree this will be the case can only be answered by additional numerical simulations with such particles and/or by additional experiments with particles of different effective density.

Finally, we address drag reduction for larger bubble concentrations up to 10%. First of all, we note that strictly speaking the relation Eq. (3.2) will no longer be valid at gas volume concentration of 5% and beyond. Nevertheless, we decided to present the ratio $c_\epsilon(\alpha, Re)/c_\epsilon^{fit}(0, Re)$ as function of α for $0 \leq \alpha < 10\%$ in Fig. 3.4, in order to give the reader an idea on what may be going on for large α. Surprisingly, beyond $\alpha = 5\%$ the drag *increases* again. From Eq. (3.1) it is seen that this result means that for a larger gas volume fraction an increasing torque T is required to keep the inner cylinder running at constant angular velocity Ω! A possible explanation of this effect is as follows: Due to the centrifugal acceleration of the water gas bubbles accumulate close to the inner cylinder. Once the gas

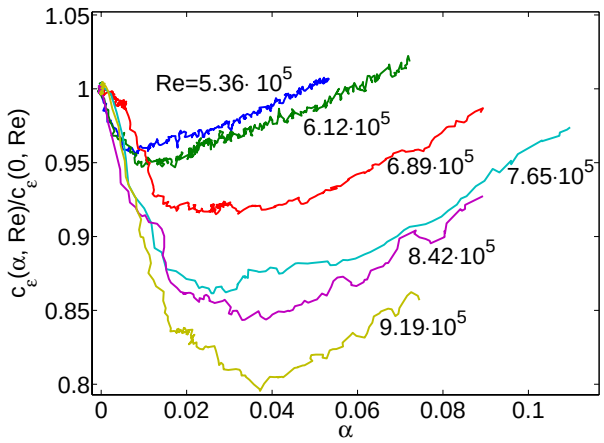

Figure 3.4: Ratio $c_\epsilon(\alpha, Re)/c_\epsilon^{fit}(0, Re)$ *versus* α *for various* Re.

fraction is too large (here beyond 5%), the gas layer at the inner cylinder may prevent an efficient forcing of the liquid between the cylinders. An *effective* Reynolds number (e.g., the Taylor-Reynolds number Re_λ) characterizing the degree of turbulence in the liquid may therefore be considerable smaller than suggested from $Re = \Omega a(b-a)/\nu$. For fixed Re_λ the ratio $c_\epsilon(\alpha, Re_\lambda)/c_\epsilon^{fit}(0, Re_\lambda)$ may in fact monotonously decrease as function of α. Unfortunately, presently we cannot measure Re_λ for our bubbly flow.

3.4 Conclusion

In conclusion, both the suggested effects for drag reduction in bubbly flow seem to contribute, namely effective flow compressibility [12] and bubble deformability [13, 15]. The relative importance of the effects depends on the bubble size and flow Reynolds number. For smaller bubbles or smaller Re the former is more important ($We < 1$), for larger bubbles or larger Re the latter ($We > 1$). In our experiments the crossover between the two regimes is around $Re \approx 6 \cdot 10^5$, corresponding to $R_b = 42\eta = 300y_0$. Clearly, further experiments and simulations with various bubble and particle sizes and density ratios are motivated by these intriguing observations. Moreover, obtaining information on the radial bubble and particle distribution, on the bubble shape, and on the importance of bub-

ble breakup would be useful. The closed flow Taylor-Couette cell seems to us to be a very suited system for further analysis of drag reduction in bubbly flow.

References

[1] P. S. VIRK, *Drag reduction fundamentals*, AIChE J. **21**, 625 (1975).

[2] N. S. BERMAN, *Drag reduction by polymers*, Ann. Rev. Fluid Dyn. **10**, 47 (1978).

[3] R. BENZI, E. S. C. CHING, I. PROCACCIA, AND N. HORESH, *Theory of concentration dependence in drag reduction by polymers and of the maximum drag reduction asymptote*, Phys. Rev. Lett. **92**, 078302 (2004).

[4] V. S. L'VOV, A. POMYALOV, I. PROCACCIA, AND V. TIBERKEVICH, *Drag reduction by polymers in wall bounded turbulence*, Phys. Rev. Lett. **92**, 244503 (2004).

[5] N. K. MADAVAN, S. DEUTSCH, AND C. L. MERKLE, *Reduction of turbulent skin friction by microbubbles*, Phys. Fluids **27**, 356 (1984).

[6] N. K. MADAVAN, S. DEUTSCH, AND C. L. MERKLE, *Measurements of local skin friction in a microbubble-modified turbulent boundary layer*, J. Fluid Mech. **156**, 237 (1985).

[7] C. MERKLE AND S. DEUTSCH, in *Frontiers in Experimental Fluid Mechanics – Lecture notes in Engineering, Vol. 46*, edited by M. G. el Hak (Springer, Berlin, 1989), p. 291.

[8] V. S. L'VOV, A. POMYALOV, I. PROCACCIA, AND V. TIBERKEVICH, *Drag reduction by microbubbles in turbulent flows: The limit of minute bubbles*, Phys. Rev. Lett. **94**, 174502, (2005).

[9] Y. KODAMA, A. KAKUGAWA, T. TAKAHASHI, AND H. KAWASHIMA, *Experimental study on microbubbles and their applicability to ships for skin friction reduction*, Int. J. Heat and Fluid Flow **21**, 582 (2000).

[10] T. TAKAHASHI *et al.*, 74th General meeting of SRI (2000).

[11] J. XU, M. R. MAXEY, AND G. E. KARNIADAKIS, *Numerical simulation of turbulent drag reduction using micro-bubbles*, J. Fluid Mech. **468**, 271 (2002).

[12] A. FERRANTE AND S. ELGHOBASHI, *On the physical mechanisms of drag reduction by polymers in a spatially developing turbulent boundary layer laden with microbubbles*, J. Fluid Mech. **503**, 345 (2004).

[13] J.C. LU, A. FERNANDEZ, AND G. TRYGGVASON, *The effect of bubbles on the wall drag in a turbulent channel flow*, Phys. Fluids **17**, 095102 (2005).

[14] K. SUGIYAMA, T. KAWAMURA, S. TAKAGI, AND Y. MATSUMOTO, in *Proceedings of the 4th Symposium on Smart Control of Turbulence* (2003).

[15] K. SUGIYAMA, T. KAWAMURA, S. TAKAGI, AND Y. MATSUMOTO, in *Proceedings of the 5th Symposium on Smart Conrol of Turbulence*, (2004).

[16] S. O. UNVERDI AND G. TRYGGVASON, *A front-tracking method for viscous, incompressible, multi-fluid flows*, J. Comput. Phys. **100**, 25 (1992).

[17] A. EINSTEIN, *A new determination of the molecular dimensions*, Ann. Phys. **19**, 289 (1906).

[18] A. ACRIVOS, *Shear-induced particle diffusion in concentrated suspensions of noncolloidal particles*, J. Rheol. **39**, 813 (1995).

[19] D. P. LATHROP, J. FINEBERG, AND H. L. SWINNEY, *Turbulent-flow between concentric rotating cylinders at large Reynolds-number*, Phys. Rev. Lett. **68**, 1515 (1992).

[20] G. S. LEWIS AND H. L. SWINNEY, *Velocity structure functions, scaling and transitions in high-Reynolds-number Taylor-Couette flow*, Phys. Rev. E **59**, 5457 (1999).

[21] T. H. VAN DEN BERG, C. DOERING, D. LATHROP, AND D. LOHSE, *Smooth and rough boundaries in turbulent Taylor-Couette flow*, Phys. Rev. E **68**, 036307 (2003).

[22] F. RISSO AND J. FABRE, *Oscillations and breakup of a bubble immersed in a turbulent field*, J. Fluid Mech. **372**, 323 (1998).

[23] D. LOHSE, *Crossover from high to low-Reynolds-number turbulence*, Phys. Rev. Lett. **73**, 3223 (1994).

[24] I.M. MAZZITELLI, D. LOHSE, AND F. TOSCHI, *The effect of microbubbles on developed turbulence*, Phys. Fluids **15**, L5 (2003); J. Fluid Mech. **488**, 283 (2003).

4

Bubbly turbulent drag reduction is a boundary layer effect §

In Ch. 3 we showed that in turbulent Taylor-Couette flow the injection of bubbles reduce the overall drag [1]. On the other hand, as was shown in Ch. 2, rough walls enhance the overall drag [2]. In this work we inject bubbles into turbulent Taylor-Couette flow with rough walls (with a Reynolds number up to $4 \cdot 10^5$*), finding an enhancement of the dimensionless drag as compared to the case without bubbles. The dimensional drag is unchanged. As in the rough-wall case no smooth boundary layers can develop, the results demonstrate that bubbly drag reduction is a pure boundary layer effect.*

4.1 Introduction

Turbulent drag reduction can be achieved either by polymers [3–7] or by bubbles [1, 7–13] or a combination of both [15]. The phenomenon has huge potential for applications in the naval transport sector [14]. Even a small reduction of a few percent on the fuel consumption of ships means a considerable annual saving. One drag reduction method is to reduce the skin friction through micro-bubble injection at the ships' hull. Using this, a research team in Japan has found drag reduction on their experimental ship, the Seiun-Maru, of up to 5% [16] and in the USA reductions of 5 to 15% were achieved on a surface effect Catamaran fitted with a microbubble drag reduction system [17].

A generally accepted explanation of the effect is lacking. Several theories are competing: Based on numerical simulations Ferrante et al. [18] argue that the microbubbles in a spatially developing turbulent boundary

§See: Thomas H. van den Berg, Dennis P. M. van Gils, Daniel P. Lathrop, and Detlef Lohse, *Bubbly turbulent drag reduction is a boundary layer effect*, submitted to PRL (2006)

layer push the developing stream-wise vortices away from the wall, leading to less dissipation in the boundary layer. Numerical simulations by Lu et al. [19] show that deformable bubbles lead to a significant reduction of the drag by the suppression of stream-wise vorticity. Van den Berg *et al.* [1] showed that both mechanisms contribute, though the deformability of the bubbles seems to be of main importance, leading to stronger drag reduction. Lo *et al.* [20] conclude that bubble volume oscillations and thus the compressibility of the bubble-water mixture play an important role for the drag reduction.

In this paper we want to investigate the effect of the wall roughness on bubbly drag reduction: First, because for practical applications rough walls are more realistic than smooth ones. Second, in order to get more insight into the mechanism of bubbly drag reduction and in particular to probe whether boundary layer (BL) effects play a role. Rough walls drastically modify the dynamics in the laminar BLs and trigger the development of turbulent BLs. Indeed, roughening the walls in a single-phase flow Taylor-Couette setup the overall drag could be increased by a factor of 50 [2, 21]. Moreover, the drag scales more steeply with the Reynolds number as compared to the smooth-wall case [2, 21], in coherence with what one would expect when transferring the ideas of the unifying scaling theory for thermal convection [22] to the Taylor-Couette case [23].

The effect of bubbles on the drag within a turbulent water tunnel with rough walls has been examined in Refs. [24]. In these experiments the drag force was directly measured with a drag balance, as a function of the position and of the (injected) gas flow rate. In spite of the wall roughness the addition of bubbles reduced the drag, similarly as the addition of polymers reduced the drag in such water tunnel experiments [24, 25]. In these experiments [24, 25] wavy structures or grits were attached to the surfaces of the walls. In the polymeric case [25] the effect was even stronger than for the smooth-wall case, presumably because of the higher absolute drag for the rough-wall case. In contrast, Cadot *et al.* [26] did not find any polymeric drag reduction for *inertially forced* (with baffles) turbulence. They concluded that the polymeric drag reduction effect observed in the smooth wall case is solely related to a diminution of the dissipation in the viscous boundary layer where most of the energy is dissipated. This is consistent with the present theoretical understanding of polymeric drag reduction, see e.g. Ref. [6, 27] and references therein.

4.2 Experiments

4.2.1 Theory

To measure the potential drag reduction effect of bubbles in turbulence in a system with rough walls, we again choose the Taylor-Couette geometry, just as we did in Ref. [2] for the effect of rough walls only and in Ref. [1] for the effect of bubbles only. The advantage of the Taylor-Couette system is that it is *closed* which makes it possible to deduce the overall dissipation rate ϵ from the well-controlled energy input rate determined by the torque. Moreover, statistically stationary states are easy to achieve. Thus by measuring the torque on the inner cylinder (rotating with fixed angular velocity Ω) the total energy dissipation rate of the flow can be deduced, which in turn is a measure of the drag:

$$\epsilon = \frac{T\Omega}{\pi\rho L(b^2-a^2)} = \frac{\nu^2 G\Omega}{\pi(b^2-a^2)}. \tag{4.1}$$

Here T is the torque, $G = T/\rho\nu^2 L$ its non-dimensionalized form, ρ is the density of the liquid, and ν the kinematic viscosity. The height of the cylinder is L and the inner and outer radii are a and b, respectively. The drag coefficient c_ϵ follows from non-dimensionalization,

$$c_\epsilon = \frac{\epsilon(b-a)}{\Omega^3 a^3} = \frac{T}{\pi\rho L\Omega^2 a^3(b+a)}. \tag{4.2}$$

4.2.2 Experimental Setup

The Taylor-Couette setup used for these experiments is described in detail in Refs. [1, 2, 28]. Here we only briefly summarize its specifications and refer to the mentioned papers for more information. The setup has an inner cylinder with radius $a = 16cm$ and an outer cylinder with radius $b = 22cm$; the liquid-containing gap is thus $6cm$. The outer cylinder is stationary, the inner one can rotate to frequencies up to 16Hz, resulting in a maximum $Re \approx 10^6$ for the single-phase water case. The total length is $L = 69.5cm$, resulting in an aspect ratio of $\Gamma = L/(b-a) = 11.6$. To minimize the effects of the top and bottom boundaries, the inner cylinder consists of three parts, with a measuring section in the middle. The length of this section is 40cm. It is attached to the inner shaft by low friction bearings. The actual torque on this part is measured by means of a load cell and strain gauges which are measured by means of a lock-in amplifier.

The top and bottom sections of the fluid volume serve as heat sinks in order to maintain a constant temperature of the working liquid. In this way we were able to keep the temperature constant within a tenth of a degree. Therefore we assume the dynamic viscosity and the density to remain constant. In the experiments with rough walls the roughening was achieved by attaching 16 square perspex rods (thickness 3mm) equally spaced in azimuthal angle on the inner and outer cylinder, as in Refs. [2, 21].

The air bubbles are injected into the turbulent flow through eight needles located at the bottom of the outer cylinder. The void fraction α was estimated by measuring the excess volume pushed out of the system because of the added gas as in Ref. [1]. The bubble size is dictated by the strength of the shear and is typically in the range of 2mm to 0.5mm [29]. The boundary layer inner length scale is significantly smaller, $y_0 = \nu/u_* \approx 3\mu m$, with $u_* = \sqrt{\tau_w/\rho}$ and the shear stress τ_w being estimated as [28] $\tau_w = T/\pi a^2 L$.

Due to centrifugal forces the air bubbles tend to accumulate near the inner cylinder which eventually would lead to a decoupling of the working liquid from the inner cylinder. However, when limiting the void fractions to values of up to 8% the decoupling can be prevented.

When injecting bubbles into the flow, the kinematic viscosity and density are changed. The kinematic viscosity for a bubbly liquid is assumed to obey [30]

$$\nu = \nu_0(1 + \frac{5}{2}\alpha) \tag{4.3}$$

where $\nu_0 = \nu(\alpha = 0)$. Another reason to limit ourselves to low overall gas fractions of up to 8% is that relation (4.3) becomes more and more questionable for larger gas fractions (see e.g. Ref. [31]) – but note that the *local* gas concentration can be higher than 8% due to bubble accumulation in the vortices. The flow Reynolds number is defined with the viscosity of the bubbly liquid,

$$Re = \frac{\Omega a(b-a)}{\nu} = \frac{\Omega a(b-a)}{\nu_0(1+\frac{5}{2}\alpha)}. \tag{4.4}$$

Altogether, we had four different experimental settings: smooth walls with single phase liquid, smooth walls with two phase liquid, rough walls with single phase liquid, and rough walls with two phase liquid. The Reynolds number range spans $1 \cdot 10^5 < Re < 4 \cdot 10^5$, which is limited by the maximum available torque of the motor.

The experimental procedure was as follows: We first measured the dimensionless drag without bubble injection as a function of Reynolds number, $c_\epsilon(\alpha = 0, Re)$. The resulting data are fitted by a spline or in the smooth wall case by a crossover function [1, 32], leading to two curves $c_\epsilon^{fit}(\alpha = 0, Re)$, namely one for the smooth-wall case (shown in the inset of Fig. 4.1a) and one for the rough-wall case. We then kept the rotation rate of the inner cylinder constant and slowly increased the void fraction while continuously measuring both α and the torque.

4.2.3 Results

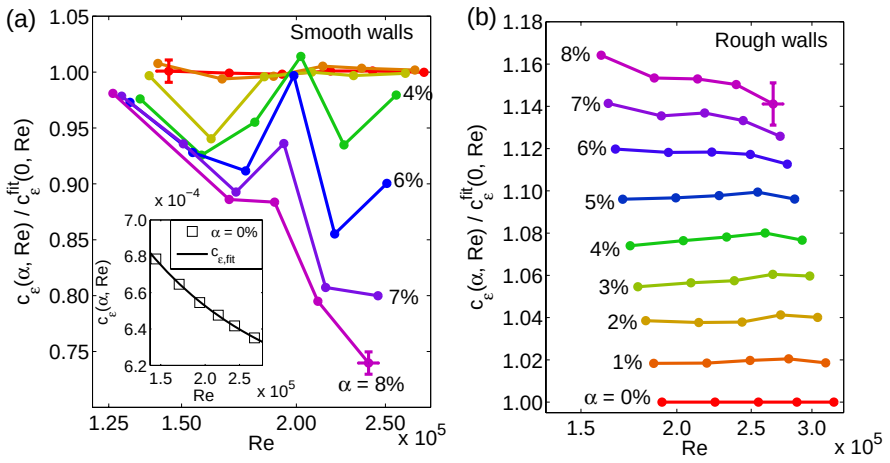

Figure 4.1: Compensated drag coefficient $c_\epsilon(\alpha, Re)/c_\epsilon^{fit}(0, Re)$ vs. Reynolds number for increasing void fractions α for the smooth wall case (a) and the rough wall case (b). While in the smooth wall case (a) the drag decreases up to 25%, in the rough wall case (b) the bubble injection leads to a drag enhancement.

In Fig. 4.1a we show the compensated drag coefficient $c_\epsilon(\alpha, Re)/c_\epsilon^{fit}(0, Re)$ vs. Reynolds number for increasing void fractions α for the smooth-wall case. After a certain threshold in α of about 2% a strong drag reduction of up to 25% can be observed, as compared to the single phase case.

For the rough-wall case the behavior is very different, as can be seen from Fig. 4.1b. In contrast to the smooth-wall case, the drag coefficient increases with increasing void fraction α, even up to 16% for the 8% void fraction case. We conclude that the wall roughness prevents bubbly drag

reduction. Apparently, drag reduction by bubbles is a boundary layer effect, just as polymeric drag reduction [26]. In the rough-wall case the structure of the viscous BLs seems to be so strongly modified that the mechanism for bubbly drag reduction can no longer be active.

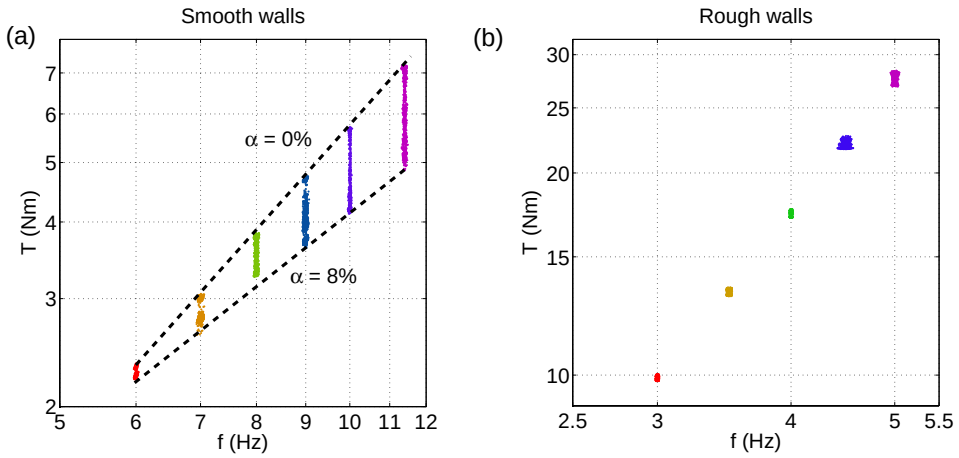

Figure 4.2: Torque (in Nm) versus the rotation rate (in Hz) of the inner cylinder for increasing void fractions: (a) smooth-wall case and (b) rough-wall case. In (a) a decrease of dimensional torque with increasing void fraction α can be seen. For the rough walled case (b) the dimensional torque seems to be independent of the void fraction.

4.2.4 Dimensional torque results

We point the reader to some interpretation ambiguities on what drag reduction means. In Fig. 4.2 we present the data for the rough and the smooth wall cases in their *dimensional* form. For the smooth-wall case (Fig. 4.2a) with increasing void fraction a reduction in the required torque for constant rotation rate is observed, just as expected. However, in the rough-wall case (Fig. 4.2b) the *dimensional* torque does not seem to depend on the (increasing) void fraction. This mean that *only when compensating for the change in density and viscosity* the rough-wall results can be interpreted as drag increase through bubble injection. The smooth wall case is free of this interpretation ambiguity: Both the dimensional and the dimensionless drag decrease with increasing void fraction α.

In order to compare our results with theoretical approaches [20] it

would be of prime interest to know the bubble concentration profile, both in the smooth and in the rough wall case. Corresponding measurements are on their way.

4.3 Conclusion

In conclusion, we have measured the drag for bubbly turbulence in a Taylor-Couette system for smooth and rough walls. For the smooth-wall case a strong reduction in drag coefficient was found, in agreement with our earlier experimental results [1] and in agreement with theory [20]. For the rough-wall case we found an enhancement of the dimensionless drag coefficient with increasing void fraction, whereas the dimensional torque did not change. Independent of these interpretation ambiguities, the general conclusion is quite clear: There is no drag reduction for Taylor-Couette turbulence with rough-walls whereas a strong drag reduction is observed for the smooth-wall case. Bubbly drag reduction is hence a boundary layer effect.

Through our results one can understand why growth of barnicals or other organic material at the ship hull or its corrosion drastically degrade the drag reduction effect of injected bubbles: The roughness caused by the organic material or by the corrosion destroys the smooth BL and therefore the mechanism leading to bubbly drag reduction.

References

[1] T. H. VAN DEN BERG, S. LUTHER, D. P. LATHROP, AND D. LOHSE, *Drag reduction in Taylor-Couette turbulence*, Phys. Rev. Lett. **94**, 044501 (2005).

[2] T. H. VAN DEN BERG, C. DOERING, D. LOHSE, AND D. P. LATHROP, *Smooth and rough boundaries in turbulent Taylor-Couette flow*, Phys. Rev. E **68**, 036307 (2003).

[3] P. S. VIRK, *Drag reduction fundamentals*, AIChE J. **21**, 625 (1975).

[4] N. S. BERMAN, *Drag reduction by polymers*, Ann. Rev. Fluid Dyn. **10**, 47 (1978).

[5] R. BENZI *et al.*, *Theory of concentration dependance in drag reduction by polymers and of the maximum drag reduction asymptote*, Phys. Rev. Lett. **92**, 078302 (2004).

[6] V. S. L'VOV, A. POMYALOV, I. PROCACCIA, AND V. TIBERKEVICH, *Drag reduction by polymers in wall bounded turbulence*, Phys. Rev. Lett. **92**, 244503 (2004).

[7] S. PAL, S. DEUTSCH, AND C. L. MERKLE, *A comparison of shear-stress fluctuation statistics between microbubble modified and polymer modified turbulent boundary-layers*, Phys. Fluids **A1**, 1360 (1989).

[8] J. XU, M. R. MAXEY, AND G. E. KARNIADAKIS, *Numerical simulation of turbulent drag reduction using microbubbles*, J. Fluid Mech. **468**, 271 (2002).

[9] K. SUGIYAMA, T. KAWAMURA, S. TAKAGI, AND Y. MATSUMOTO, in *Proceedings of the 4th Symposium on Smart Control of Turbulence* (2003); and in *Proceedings of the 5th Symposium on Smart Control of Turbulence*.

[10] N. K. MADAVAN, S. DEUTSCH, AND C. L. MERKLE, *Reduction of turbulent skin friction by microbubbles*, Phys. Fluids **27**, 356 (1984); *Measurements of local skin friction in a microbubble-laden turbulent boundary layer*, J. Fluid Mech. **156**, 237 (1985).

[11] C. L. MERKLE AND S. DEUTSCH, in *Frontiers in Experimental Fluid Mechanics – Lecture notes in Engineering, Vol. 46*, edited by M. G. el Hak (Springer, Berlin, 1989), p. 291.

[12] V. S. L'VOV, A. POMYALOV, I. PROCACCIA, AND V. TIBERKEVICH, *Drag reduction by microbubbles in turbulent flows: The limit of minute bubbles*, Phys. Rev. Lett. **94**, 174502 (2005).

[13] W. C. SANDERS *et al.*, *Bubble friction drag reduction in a high-Reynolds-number flat-plate turbulent boundary layer*, J. Fluid Mech. **552**, 353 (2006).

[14] Y. KODAMA, A. KAKUGAWA, T. TAKAHASHI, AND H. KAWASHIMA, *Experimental study on microbubbles and their applicability to ships for skin friction reduction*, Int. J. Heat and Fluid Flow **21**, 582 (2000).

[15] S. DEUTSCH, A. A. FONTAINE, M. J. MOENY, AND H. L. PETRIE, *Combined polymer and microbubble drag reduction on a large flat plate*, J. Fluid Mech. **556**, 309 (2006).

[16] Y. KODAMA, A. KAKUGAWA, S. NAGAYA, AND T. KAWAMURA, Report of 24th US-Japan Joint Meeting, Marine Facilities Panel of the U.S./Japan Cooperative Program in Natural Resources (2001).

[17] R. LATORRE, A. MILLER, AND R. PHILIPS, *Microbubble drag reduction for high speed craft*, Trans. SNAME **110**, 259 (2002).

[18] A. FERRANTE AND S. ELGHOBASHI, *On the physical mechanisms of drag reduction by polymers in a spatially developing turbulent boundary layer laden with microbubbles*, J. Fluid Mech. **503**, 345 (2004).

[19] J. C. LU, A. FERNANDEZ, AND G. TRYGGVASON, *The effect of bubbles on the wall drag in a turbulent channel flow*, Phys. Fluids **17**, 095102 (2005).

[20] T. S. LO, V. S. L'VOV, AND I. PROCACCIA, *Drag reduction by compressible bubbles*, Phys. Rev. E **73**, 036308 (2006).

[21] O. CADOT *et al.*, *Energy injection in closed turbulent flows: Stirring through boundary layers versus inertial stirring*, Phys. Rev. E **56**, 427 (1997).

[22] S. GROSSMANN AND D. LOHSE, *Scaling in thermal convection: an unifying theory*, J. Fluid. Mech. **407**, 27 (2000); *Thermal convertion for large Prandtl numbers*, Phys. Rev. Lett. **86**, 3316 (2001); *Prandtl and Rayleigh number dependence of the Reynolds number in turbulent*

thermal convection, Phys. Rev. E **66**, 016305 (2002); *Fluctuations in turbulent Rayleigh-Bénard convection: the role of plumes,* Phys. Fluids **16**, 4462 (2004).

[23] B. ECKHARDT, S. GROSSMANN, AND D. LOHSE, *Scaling of global momentum transport in Taylor-Couette and pipe flow,* Eur. Phys. J. B **18**, 541 (2000); Europhys. Lett., submitted (2006).

[24] S. DEUTSCH, M. MOENY, A. A. FONTAINE, AND H. L. PETRIE, *Microbubble drag reduction in rough walled turbulent boundary layers with comparison against polymer drag reduction,* Exp. in Fluids **37**, 731 (2004).

[25] M. VLACHOGINANNIS AND T. J. HANRATTY, *Influence of wavy structured surfaces and large scale polymer structures on drag reduction,* Exp. in Fluids **36**, 685 (2004).

[26] O. CADOT, D. BONN, AND S. DOUADY, *Turbulent drag reduction in a closed flow system: Boundary layer versus bulk effects,* Phys. Fluids **10**, 426 (1998).

[27] R. BENZI *et al., Maximum drag reduction asymptotes and the cross-over to the Newtonian plug,* J. Fluid Mech. **551**, 185 (2006).

[28] D. P. LATHROP, J. FINEBERG, AND H. L. SWINNEY, *Turbulent flow between concentric rotating cylinders at large Reynolds numbers,* Phys. Rev. Lett. **68**, 1515 (1992);
G. S. LEWIS AND H. L. SWINNEY, *Velocity structure functions, scaling, and transitions in high-Reynolds number Couette-Taylor flow,* Phys. Rev. E **59**, 5457 (1999).

[29] F. RISSO AND J. FABRE, *Oscillations and breakup of a bubble immersed in a turbulent field,* J. Fluid Mech. **372**, 323 (1998).

[30] A. EINSTEIN, *A new determination of the molecular dimensions,* Ann. Phys. **19**, 289 (1906).

[31] A. ACRIVOS, *Shear-induced particle diffusion in concentric suspensions of non-colloidal particles,* J. Rheol. **39**, 813 (1995).

[32] D. LOHSE, *Crossover from high to low-Reynolds number turbulence,* Phys. Rev. Lett. **73**, 3223 (1994).

Part II

Twente Water Tunnel

5

Turbulent Bubbly Flow[§]

The effect of bubbles on fully developed turbulent flow is investigated numerically and experimentally summarizing the results of our Refs. [1–4]. On the numerical side we simulate Navier-Stokes turbulence with a Taylor-Reynolds number of $Re_\lambda \approx 60$, a large scale forcing, and periodic boundary conditions. The point-like bubbles follow their Lagrangian pathes and act as point forces on the flow. As a consequence, the spectral slope is less steep as compared to the Kolmogorov case. The slope decrease is identified as a lift force effect. On the experimental side we do hot-film anemometry in a turbulent water channel with $Re_\lambda \approx 200$ in which we have injected small bubbles up to a volume percentage of 3%. Here the challenge is to disentangle the bubble spikes from the hot-film velocity signal. To achieve this goal we have developed a pattern recognition scheme. Furthermore, we injected microbubbles up to a volume percentage of 0.3%. Both in the counter flowing situation with small bubbles and in the co-flow situation with microbubbles we obtain a less spectral slope, in agreement with the numerical result.

5.1 Introduction

Turbulent bubbly flows are ubiquitous in nature and in many technical applications. Two basic questions arise when dealing with turbulent bubbly flow: (i) How do bubbles move within the flow? and (ii) How do they affect the turbulence? This work will therefore focus on two observables:

- The *bubble distribution* in the fluid: In turbulent flow initially uniformly distributed bubbles cluster in regions of low pressure and

[§]See: Thomas H. van den Berg, Stefan Luther, Irene M. Mazzitelli, Judith M. Rensen, Federico Toschi, and Detlef Lohse, *Turbulent Bubbly Flow*, Journal of Turbulence **7** (14), 1-12 (2006). T.H. van den Berg is responsibly for part of the experimental results.

high vorticity [5, 6]. Also experiments with isolated vortices [7] confirm that bubbles are trapped by them and, moreover, tend to collect on their downflow side.

- The *spectral information:* The effect of bubbles on the turbulence spectrum has been investigated experimentally [8, 9]. Lance & Bataille found that relatively large bubbles modify the inertial range scaling. The Kolmogorov energy spectrum power law $-5/3$ is substituted by a $-8/3$ slope with increasing bubble concentration [8]. It is argued that the steeper spectrum originates from immediate dissipation of the energy production within the bubbles' wakes. In contrast Mudde et al. [9] found the classical $-5/3$ power law in a bubble column even for a gas volume fraction of 25%. Numerical work [10, 11] shows that two-way coupled microbubbles can reduce the turbulent energy in decaying turbulence (depending on the initial bubble distribution) and in turbulent mixing layers under certain conditions.

In this paper, we first numerically analyze how microbubbles move in and act on three-dimensional developed turbulence [1, 2]. The aim is to demonstrate that above mentioned energy reduction process is rather general and to highlight the role of the *lift force* therein, which had not been taken into account in refs. [10, 11]. We then compare the spectra with the experimental results [3, 4]. For small bubbles with a radius of 20η we find a less steep spectral slope as compared to the Kolmogorov classical $-5/3$ power law [3]. This effect is found to be consistent with our numerical simulations: we find an increase of energy for two-phase flow as compared to single-phase flow. This enhancement is more pronounced on small scales than on large scales, leading to a less steep slope, just as numerically found. However, here extra pumping was required to overcome buoyancy. In contrast for microbubbles [4] with a radius of 1η and a void fraction of 0.3% no extra pumping was required, allowing for a direct comparison with our numerical results. We find a spectral reduction at large scales and an enhancement at small scales, just as in the numerics.

5.2 Numerical simulation

5.2.1 Forces on the bubble

The microbubbles are assumed to be spherical with fixed radius a, which is small compared to the scales on which the flow varies, and their density

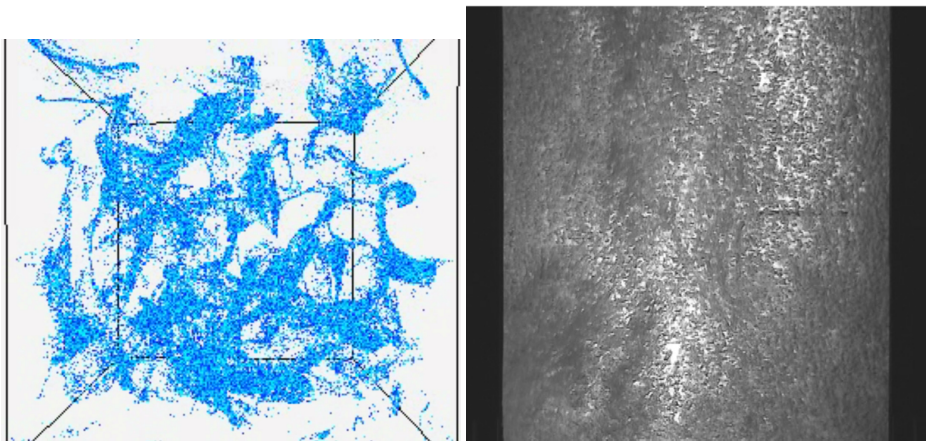

Figure 5.1: (a) Numerical bubble distribution for $\tau_b = \tau_k$ and $\boldsymbol{v}_b = \boldsymbol{v}_k$ (following from our numerical simulations [1, 2]) and (b) experimental bubble distribution in the Twente Water Channel [3]. In both cases the bubble clustering in the vortices can be recognized.

is considered to be negligible as compared to the fluid density. The bubble motion can then be modeled by the equation [1, 2, 12–15]:

$$\frac{d\mathbf{v}}{dt} = 3\frac{D\mathbf{u}}{Dt} + \frac{1}{\tau_b}(\mathbf{u}(\mathbf{y}(t),t) - \mathbf{v}(t)) - 2\mathbf{g} - (\mathbf{v}(t) - \mathbf{u}(\mathbf{y}(t),t)) \times \omega(\mathbf{y}(t),t) \tag{5.1}$$

where $\mathbf{u}(\boldsymbol{x},t)$ is the turbulent velocity field, $\mathbf{y}(t)$ is the bubble position, $\mathbf{v}$ the bubble velocity, $\omega = \nabla \times \mathbf{u}$ the fluid vorticity, $\mathbf{g}$ the gravity, and τ_b a time scale connected with the rise velocity of a bubble in still fluid $v_T = 2g\tau_b$. The material derivative (D/Dt) of the fluid velocity is evaluated at the bubble position. The four terms on the right hand side of Eq. (5.1) represent the fluid acceleration plus added mass effects, the drag force, the buoyancy, and the lift force, respectively.

5.2.2 Simulation of the flow

Direct numerical simulations are employed in order to simulate the velocity field $\mathbf{u}(\boldsymbol{x},t)$. The flow satisfies the three-dimensional, incompressible Navier Stokes equations,

$$\frac{\partial \mathbf{u}}{\partial t} + \mathbf{u}\cdot\nabla\mathbf{u} = -\frac{1}{\rho}\nabla p + \nu\Delta\mathbf{u} + \mathbf{f}_L + \mathbf{f}_b. \tag{5.2}$$

The computational domain is a cube of side $L_0 = 2\pi$ subjected to periodic boundary conditions. The grid consists of 128^3 points. A statistically stationary state is achieved and sustained by forcing the turbulence at large scales. The forcing on the $\mathbf{k}$th mode of the velocity field is

$$\mathbf{f}_L(\mathbf{k},t) = \varepsilon \frac{\mathbf{u}(\mathbf{k},t)}{\sum_{\mathbf{k}\in K_{in}} |u_i(\mathbf{k},t)|^2}, \quad \mathbf{k} \in K_{in} \tag{5.3}$$

and $\mathbf{f}_L(\mathbf{k},t) = 0$ otherwise.
Here $K_{in} = \{\mathbf{k}|L_0/2\pi\mathbf{k} = \pm(-1,2,2), \pm(2,-1,-1)+\text{Permutations}\}$ [16], i.e. only the large scales are forced. Without the bubble forcing $\mathbf{f_b}$ in Eq. (5.2) the energy input rate $< \mathbf{f_L} \cdot \mathbf{u} >$ and the dissipation rate $\epsilon = \nu < (\partial_i u_j)^2 >$ balance in the statistically stationary case. The Taylor-Reynolds number is $Re_\lambda = 62$. Details on the numerics can be found in Refs [1, 2].

The bubble's back reaction on the flow is taken into account by using the point-force approximation [17]. The forcing is [1, 2, 14, 18]:

$$\mathbf{f}_b(\boldsymbol{x},t) = \sum_{i=1}^{N_b} \Big(\frac{D}{Dt}\mathbf{u}(\mathbf{y_i}(\mathbf{t}),\mathbf{t}) - \mathbf{g} \Big) \mathcal{V}_\mathbf{b} \delta(\boldsymbol{x} - \mathbf{y_i}(\mathbf{t})) \tag{5.4}$$

$\mathbf{y_i}(\mathbf{t})$ is the Lagrangian position of the i-th bubble at time t, $\mathcal{V}_b$ is its volume and N_b is the total number of bubbles.

5.2.3 Bubble clustering in vortices

When a bubble is rising in water, it locally transfers momentum mainly upwards, in the direction opposite to gravity (see Eq. (5.4)). Therefore it is important to identify the structures in which bubbles are preferentially accumulating, as the back reaction may lead to an enhancement or to a suppression of the velocity fluctuations in these regions.

Previous investigations show that particles moving in a turbulent flow fall down faster than in still fluid whereas bubbles rise slower than in non turbulent flow [18–20]. This effect is attributed to the phenomenon of 'preferential sweeping' [19] of particles and bubbles in downwards fluid velocity regions. We find it confirmed in our numerical simulations [1, 2]. It already occurs in the one-way coupling case, i.e., $\mathbf{f_b} = \mathbf{0}$ in Eq. (5.3). For example, for the case $\tau_b = \tau_k$ (the Kolmogorov time scale) and $v_T = v_k$ (the Kolmogorov velocity scale) we find [1] that 58% of the bubbles are at a flow position with a downward velocity, leading to a 72% reduction

of the mean bubble rise velocity. Refs. [1, 2] have identified preferential sweeping as an effect of the lift force. Indeed, when turning off the lift in the simulations the number of bubbles in upward and downward flow regions are nearly equal.

From a visualization of the bubbles locations (Fig. 5.1a) the bubble clustering in the vortex tubes is evident. It can be quantified by measuring the ratio $\langle\Omega\rangle_b/\langle\Omega\rangle$, i.e., the time averaged enstrophy at the bubble positions normalized with the average flow enstrophy. This ratio is always larger than 1, indicating clustering in high vorticity zones. For the above mentioned case $v_T = v_k$ and $\tau_b = \tau_k$ the clustering effect is most pronounced; we have found $\langle\Omega\rangle_b/\langle\Omega\rangle$=2.3.

5.2.4 Bubbles coupling to the carrier flow: spectral modifications

For the two-way coupling case (i.e., $\mathbf{f}_b$ as in Eq. (5.4)) we choose $\tau_b = \tau_k/10$. The reason for this (small) response time is to restrict our analysis to small bubble radii, in order to apply the point force approximation. The ratio $a/\eta = 0.8$, $N_b = 144000$, and the void fraction is $\alpha \simeq 1.6\%$. Bubble-bubble interactions are neglected. This regime corresponds to microbubbles of diameter $d \simeq 150\mu m$ in clean water. The bubble response time is kept constant and the rise speed is changed. For these two-way coupling simulations clustering in vortices and preferential sweeping still exist, though in a more modest form as compared to the one-way coupling case [2, 10].

Our main finding for the two-way coupling case [1, 2] is that the bubble action on the flow is selective in wavenumber: in Fig. 5.2 the dissipative spectra $D(k) = 2\nu k^2 E(k)$ are compared to the spectrum for single-phase flow. The spectrum with two-way coupling is *reduced* with respect to the single-phase turbulence at *large scales* and *enhanced* at *small* scales. Consequently, bubbles act as a sink of energy at large scale, whereas they force the flow at small scale.

In the competition between large scale and small scale effect we find that, for the Taylor-Reynolds number treated here ($Re_\lambda = 62$ which is hardly modified through the two-way coupling), the large scale reduction overwhelms the small scale input: the overall effect is a *reduction* of the turbulent dissipation rate. We find this result remarkable as in pseudo-turbulence (flow forcing exclusively through rising bubbles) the rising bubbles of course induce extra dissipation. In Fig. 5.4 the total energy dissipation is plotted as a function of the ratio v_T/v_k. Note that, without bubbles, $\varepsilon = 1$. The curve has a minimum at $v_T/v_k \simeq 3\ldots4$.

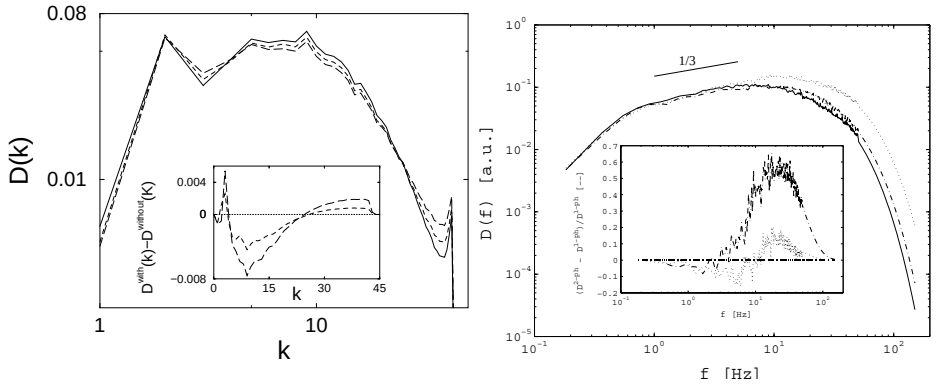

Figure 5.2: Left: dissipative spectra $D(k) = k^2E(k)$ from the numerical simulation [1] for $v_T = 2v_k$ (dashed) and $v_T = 4v_k$ (long dashed) compared to the single phase spectrum (solid). The inset shows the difference between the dissipative spectra of the single phase flow $D^{without}(k)$ and the two two-way coupled cases. Right: The right figure shows the dissipative spectra $D(f) = f^2E(f)$ for the experiments with microbubbles (taken from [4]). The solid line refers to single phase flow, the dashed and the dotted line to two-phase flow with increasing volume fraction. The insets show the difference between dissipative spectra with and without bubbles. In both the numerical and experimental case it is seen that there is an enhancement at large scales and an energy reduction at small scales.

The physical explanation of our numerical finding is that microbubbles, accumulated in downflow regions, locally transfer momentum upwards (see Fig. 5.3). Consequently, they reduce the intensity of the vertical velocity fluctuations and therefore also of the turbulent kinetic energy. The strongest effect is achieved when the bubble velocity scale v_T is of the order of the rms velocity fluctuation u_0, indeed corresponding to $v_T/v_k \simeq 3-4$. Then the bubble interaction with the energy containing large scale structures is most efficient and the dissipation reaches its minimum.

An energy reduction on large scales and an energy enhancement on small scales means the slope of the energy spectrum slope is less steep than in single phase-turbulence. Moreover, it will depend on the number of bubbles and will therefore be *non-universal*.

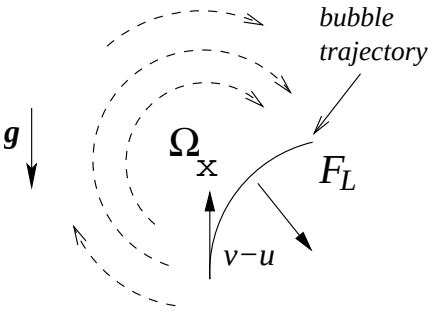

Figure 5.3: The lift force acting on a bubble rising in a horizontal vortex pushes it to the side with downward velocity (cf. Eq. (5.1)).

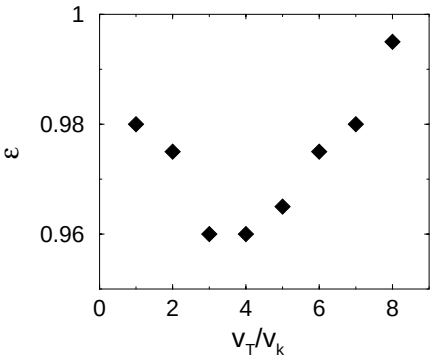

Figure 5.4: Energy dissipation rate ϵ, as a function of the ratio v_T/v_k.

5.3 Experiments

Can the reduction in the spectral slope also be found in experimental two-phase flow? To find out, we performed a series of experiments in the Twente Water Channel [21, 22] both with small bubbles ($R_b \simeq 20\eta$) [3] and with microbubbles ($R_b \simeq 1\eta$) [4].

5.3.1 Experimental setup

The Twente Water Channel is depicted in Fig. 5.5. The flow through the test section ($0.45 \times 0.45 \times 2.0$ m^3) is directed vertically downwards with mean velocities up to 0.5 m/s. The device is equipped with an active grid, which allows for Taylor-Reynolds numbers Re_λ up to 200. The Kolmogorov scale is typically $\eta \approx 10^{-4}$ m. The setup allows to study two different bubbly flow regimes. In the first regime, *small* gas bubbles with an equivalent size of 3-5 mm (corresponding to a radius of 15η to 25η) are immersed into the flow by islands of needles at the bottom, i.e. downstream of the test section (Fig. 5.5 (b,c)). Bubble size and liquid velocity are controlled such that the bubbles are rising upwards against the water flow. In this mode of operation void fractions up to 10 % can be achieved. The Reynolds number based on the bubble size is about 500. Their typical Weber number is 10.

The second regime [4] allows to study the effect of *micro*-bubbles on turbulent flow. These microbubbles are injected upstream of the test section using porous ceramic plates. The typical bubble radius is 0.1 mm;

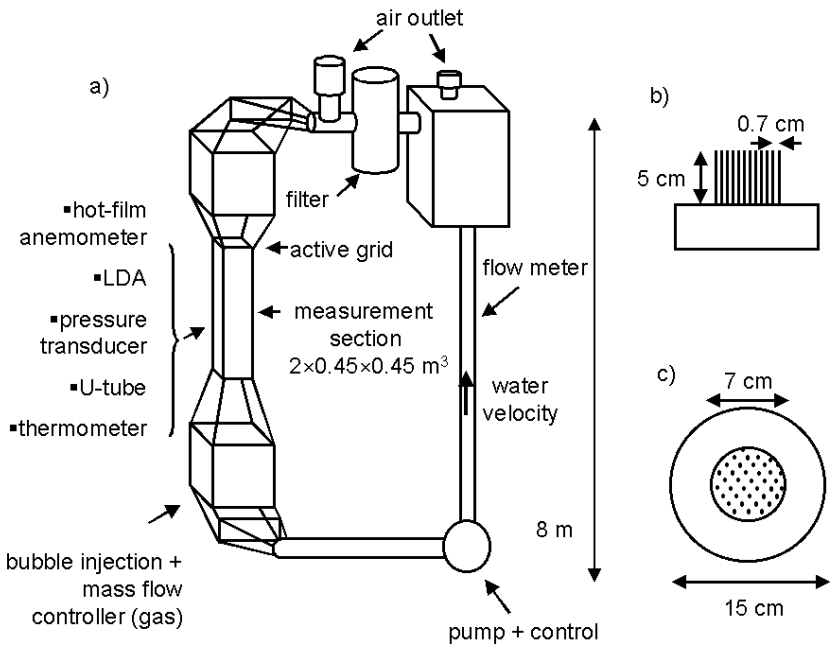

Figure 5.5: Experimental setup. (a) Vertical recirculation loop with test section, bubble injection unit, elbow pump, and reservoir. (b,c) The bubble injection unit consists of nine islands with needles (top view and side view). The gas flow is controlled by a mass flow controller.

corresponding to about 1η. The water flow velocity is controlled such that the bubbles are advected vertically downwards through the test section. In this mode of operation the maximal void fraction is 0.3 %.

The velocity of the bubbly flow is measured with a constant temperature hot-film anemometer. The probe is positioned one channel width downstream of the active grid. The probe (Dantec R55R11) has a total length of 3.0 mm (sensitive length 1.3 mm) and a diameter of 70 μm. Calibration data is obtained with a backscatter Laser-Doppler anemometer. For a description of the calibration procedure and further details of the experimental set-up, we refer to [3].

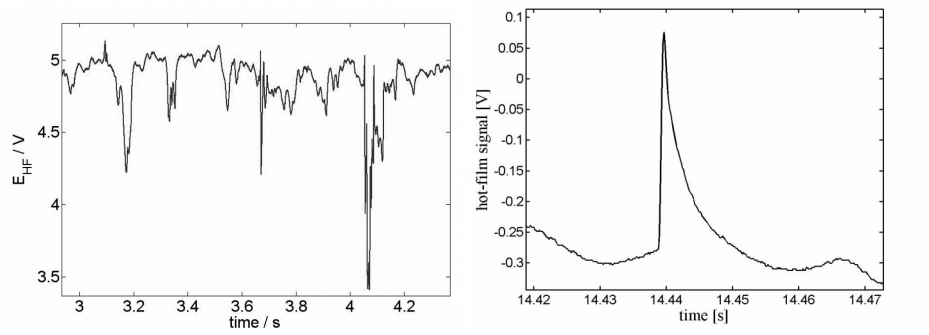

Figure 5.6: A typical hot-film signal for our measurements done with small bubbles (left) and for our measurements with microbubbles (right).

5.3.2 Signal analysis

The application of hot-film anemometry yields a velocity signal which contains information on the liquid and the bubbles due to the interaction of the bubbles with the probe. Therefore, the application of hot-film anemometry in turbulent bubbly flows consists of the following steps: (i) characterization of the bubble-probe interaction; see [23]; (ii) the detection of these interaction in the signal and its disentanglement from it [3]; (iii) conditional statistics on the segmented signal [3].

The collision of gas bubbles with the hot-film probe yields a significant change of the heat flux into the surrounding medium. This becomes visible in the hot-film signal in the form of spike-like events. The shape, the width, and the depth of this structure depends on the details of the interaction process. The interactions are commonly classified into bubble penetration, bouncing, splitting, and glancing. Details of the the shape can be understood from the dynamics of the interaction: The increase or decrease of the velocity ahead of the bubble; the spikes during the interaction due to film breakage; the velocity fluctuations due to induced bubble shape oscillations [3, 23–26]. From Fig. 5.6 we conclude that in our experiments the interaction dynamics of the microbubbles are significantly different from that of the small bubbles. The signal of the rapid impingement of microbubbles on the hot-film probe is characterized by a spike followed by an exponential decay.

Although the hot-film signal of a bubble-probe interaction has a wide variability, they share some common features. This motivates the inter-

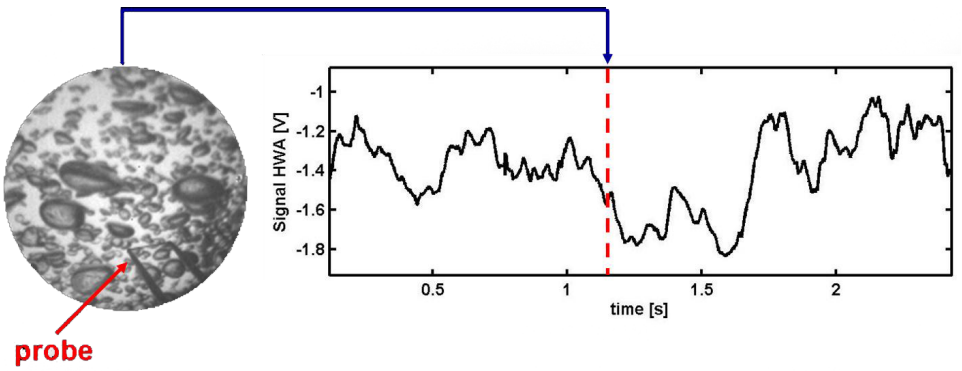

Figure 5.7: Simultaneous recordings of the hot wire signal and the endoscopically taken high-speed movie of the bubbles passing by the hot-film probe. In the lower right part of the left image the probe is visible.

pretation of the shape of the signal as the finger print of an individual interaction event. The dynamics of the bubble-probe interaction has been investigated in two sets of experiments (see [3, 23] and Ref. therein). First, a large number of bubble-probe interaction has been observed in a small water channel by recording the probe signal and high-speed stereoscopic images sequences simultaneously. This small setup allows for accurate measurements of the collision dynamics. About 350 interactions have been recorded. In a second set of experiments, the interaction of bubbles with the hot-film probe has been observed in the Twente Water Channel. This was achieved by a high-speed camera attached to an endoscope. The tip endoscope was 25 mm apart from the hot-film probe without significant distortion of the flow field. A typical data record consists of 10 s image sequence (frame rate 1 kHz) and the hot-film signal. The acquisition of the hot-film signal was triggered simultaneously with the image recording, as can be seen in Fig. 5.7. In this way the typical bubble signatures in the hot-film signal can be identified within the turbulent flow situation.

We use these features to now automatically identify the bubble spikes in the hot-film signal with the help of a neural network-type pattern recognition scheme developed in [26] and applied in [3].

The identification of the bubble-probe interactions in the signal yields a segmented time series. It is convenient to define a characteristic func-

tion ξ by

$$\xi(t) = \xi_i = \begin{cases} 1 & : \quad fluid \\ 0 & : \quad gas \end{cases} \tag{5.5}$$

indicating the presence of the gas or liquid phase at time $t = i \cdot \Delta t$, where Δt denotes the sampling interval. The characteristic function $\xi(t)$ can be used to derive conditional statistical quantities such as the mean liquid velocity or the velocity structure functions.

The power spectrum can in principle be obtained by Fourier transforming the second order velocity structure function. However, obtaining the spectrum from gapped time series as unavailable in two-phase flows is clearly nontrivial. One may believe that the problem of missing data could be solved by means of interpolating the gaps and then apply Welch's average periodogram. The result is shown in Fig. 5.8 (top), where the original single phase flow data is processed and compared to artificially gapped ones. Although the results appear promising on the first sight, the normalized power spectral density shows a significant frequency dependent bias. This example illustrates that the linear interpolation of the gaps yields a significant modification of the slope.

A remedy to the problem of spectrum calculation of gapped time series is provided by autoregressive modeling [3].

The results are shown in Fig. 5.8 (bottom). Good agreement is found for the gapped and the non-gapped data, when the used phase indication function belonged to a two-phase flow signal with a gas fraction of $\alpha < 2.0\%$. The results for the gapped signal very slightly deviates from the result for the non-gapped signal, when the phase indication function of a two-phase flow with a gas fraction of $\alpha = 2.9\%$ was used, but no frequency dependent bias is found as compared to the Welch method. The performance of the autoregressive model slightly deviates with increasing void fraction. This is due to the fact that with increasing void fraction the interaction frequency increases, which leads to a decrease of the segment lengths.

5.3.3 Power spectra

For the small bubble case ($R_b = 15\eta$ to 25η; counter-flow) the power spectral density estimate obtained by autoregressive modeling is shown in Fig. 5.9; taken from [3]. For single phase flow, the spectra show the Kolmogorov $-5/3$ scaling. As well known, intermittency effects are not very

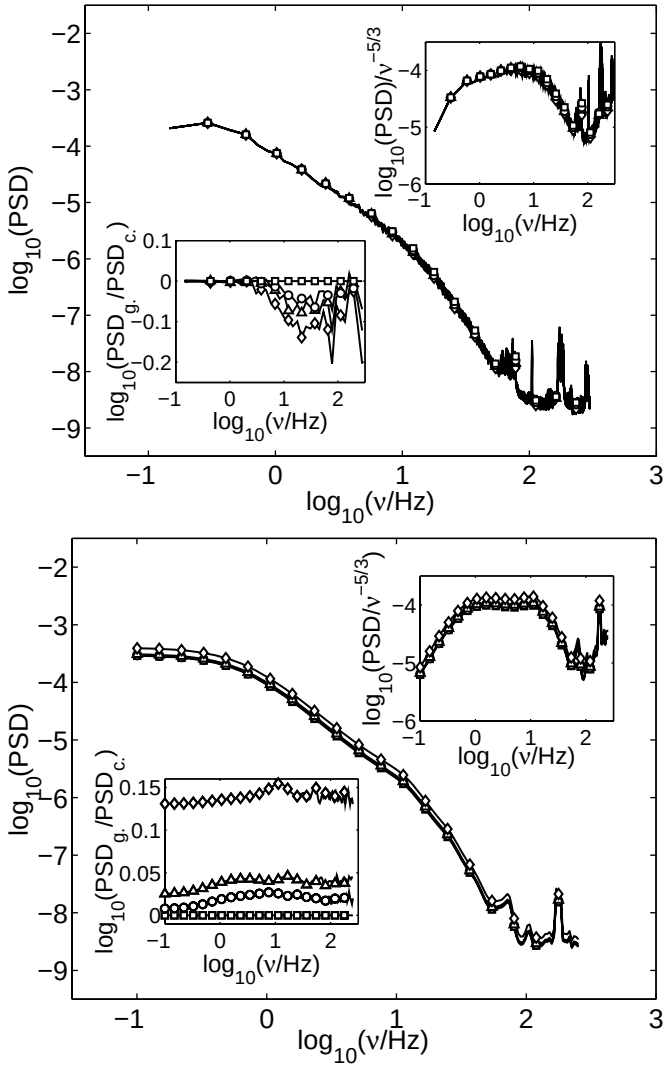

Figure 5.8: Results of processing the complete single phase data (squares) and data that were artificially gapped. To gap the data phase indication functions of two-phase flow with gas-fractions of $\alpha = 1.0\%$ ($\circ$), $\alpha = 2.0\%$ ($\triangle$ 2.0%), and $\alpha = 2.9\%$ ($\diamond$) were used. top: Power spectral density based on Fourier transform. The gaps are filled by linear interpolation. bottom: Power spectral density obtained by autoregressive modeling. In insets show the show the spectrum compensated by $\nu^{5/3}$ and the relative error given by ratio of gapped and continuous power spectral density.

visible in spectra. For the two-phase flow we measure a strong spectral energy increase at large frequencies (corresponding to small scales) and a mild spectral energy increase at small frequencies (corresponding to large scales), leading to a less steep slope as compared to $-5/3$. The less steep slope is consistent with the numerical finding on the effect of two-way coupled point-bubbles discussed in section 5.2.4 and Refs [1, 2], However, in the numerical simulations a spectral energy decrease was detected at large scales rather than the weak increase seen here. The reason for this difference between numerics and experiments presumably is that in the numerical case the flow velocity was kept constant, whereas in the experimental case with the downstream bubble injection the pump strength had to be increased in order to guarantee a large enough downflow velocity as otherwise hot-film anemometry would not be meaningful. The consequence of the stronger pumping is an additional energy input on all scales.

5.3.4 Microbubbles

This problem can be avoided in the microbubble experiments [4]. Here, flow parameters remain unchanged, apart from injecting microbubbles ($R_b = 1\eta, \alpha = 0.3\%$) from the top. We find that this injection of microbubbles indeed leads to an energy *reduction* at large scales and an energy enhancement on small scales and hence to a less steep slope as compared to the single phase case, just as predicted by our numerical simulation. Experiments and numerics are compared in Fig. 5.2. We stress that now also the typical bubble size is comparable both in experiments and numerics, namely $R_b \sim 1\eta$.
More on this can be found in Chapter 6.

5.3.5 Conclusion

The data presented in this paper do not show $-8/3$ scaling as found by Lance and Bataille [8]. However, there are general similar features, i.e. the enhancement on small scales and the energy reduction on large scales. The differences found in our measurements to those by Lance and Bataille suggest that the effect of bubbles on turbulence depends on the ratio of kinetic energy due to the bubble motion and the typical kinetic energy $\langle u'^2 \rangle$ of the fluctuations in the liquid velocity [3, 4],

$$b = \frac{1}{2}\alpha v_T^2 \,/\, \langle u'^2 \rangle \,, \tag{5.6}$$

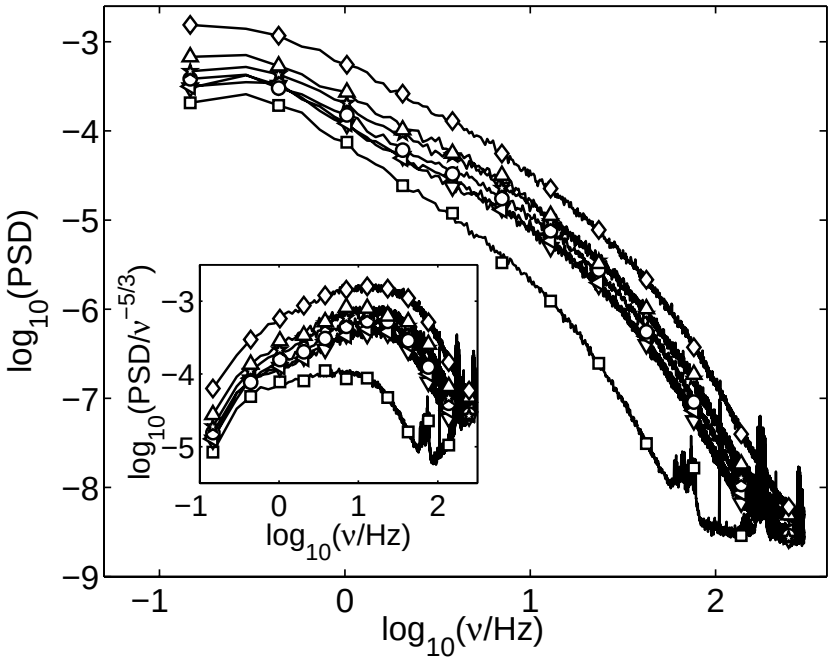

Figure 5.9: Power spectral density. The dependence on the void fraction is indicated by the following symbols: □ 0% (single phase flow); ◁ 0.5%; ○ 0.7%; ▽ 1.0%; ▷ 1.5%; △ 2.0%; ◇ 2.9%. The inserted graph shows the power spectral density compensated by $\nu^{-5/3}$.

where u' is the typical flow velocity fluctuation, and we have taken $\frac{1}{2}$ for the added mass coefficient. We call b the bubblance parameter. For $b \ll 1$ the kinetics of the bubbly flow are entirely dominated by the turbulent energy of flow, whereas for $b \gg 1$ it is dominated by the bubble motion; i.e. we have bubblance rather than turbulence. In the experiments by Lance and Bataille [8] the ratio $b \approx 1 \ldots 10$. In contrast, the microbubble data [4] as well as the numerics $b = 0.01$ [1, 2]. For the small bubbles ($R_0 \simeq 20\eta$) of Ref [3] $b = 0.1 \ldots 0.8$. The relatively large values of b in the Lance and Bataille experiments originate in their large bubbles and the relatively weak turbulence. In contrast, we can achieve stronger turbulence thanks to the active grid [21]. Therefore our bubblance parameter is always smaller than 1.

In conclusion, the main finding of both the numerical simulations and

the experiments on turbulent bubbly flows is that the bubble action on the flow is selective in wave number, leading to a less steep spectrum. As the numerical simulations reveal, this effect is related to the accumulation of bubbles in vortices, preferably on the side with down flow velocity, which is a lift force effect.

References

[1] I.M. MAZZITELLI, D. LOHSE, AND F. TOSCHI, *The effect of microbubbles on developed turbulence*, Phys. Fluids **15**, L5 (2003).

[2] I.M. MAZZITELLI, D. LOHSE, AND F. TOSCHI, *On the relevance of the lift force in bubbly turbulence*, J. Fluid Mech. **488**, 283 (2003).

[3] J. RENSEN, S. LUTHER, AND D. LOHSE, *The effect of bubbles on developed turbulence*, J. Fluid Mech. **538**, 153 (2005).

[4] T. H. VAN DEN BERG, S. LUTHER, AND D. LOHSE, *Energy spectra in microbubbly turbulence*, Phys. Fluids **18**, 038103 (2006).

[5] L.P. WANG AND M.R. MAXEY, *The motion of microbubbles in a forced isotropic and homogeneous turbulence*, Applied Scientific Research **51**, 291 (1993).

[6] O. CADOT, S. DOUADY, AND Y. COUDER, *Characterization of the low-pressure filaments in a 3-dimensional turbulent shear-flow*, Phys. Fluids **7**, 630 (1995).

[7] G. SRIDHAR AND J. KATZ, *Effect of entrained bubbles on the structure of vortex rings*, J. Fluid Mech. **397**, 171 (1999).

[8] M. LANCE AND J. BATAILLE, *Turbulence in the liquid-phase of a uniform bubble air water-flow*, J. Fluid Mech. **222**, 95 (1991).

[9] R. F. MUDDE, J. S. GROEN, AND H. E. A. VAN DEN AKKER, *Liquid velocity field in a bubbly column: LDA Experiments*, Chem. Eng. Science **52**, 4217 (1997).

[10] O. A. DRUZHININ AND S. ELGHOBASHI, *Direct numerical simulation of bubble-laden turbulent flows using the two-fluid formulation*, Phys. Fluids **10**, 685 (1998).

[11] O. A. DRUZHININ AND S. ELGHOBASHI, *Direct numerical simulation of a three-dimensionally spatially developing bubble-laden mixing layer with two-way coupling*, J. Fluid Mech. **429**, 23 (2001).

[12] N. H. THOMAS, T. R. AUTON, K. J. SENE, AND J. C. R. HUNT, in *Gas transfer at water surfaces*, edited by W. Brutsaert and G. H. Jurka (D. Reidel, Berlin, 1984), p. 255.

[13] P. D. M. SPELT AND A. BIESHEUVEL, *On the motion of gas bubbles in homogeneous isotropic turbulence*, J. Fluid Mech. **336**, 221 (1997).

[14] E. CLIMENT, Ph.D. thesis, Inst. Nat. Polytech. Toulouse, 1996.

[15] E. CLIMENT AND J. MAGNAUDET, *Large-scale simulations of bubble-induced convection in a liquid layer*, Phys. Rev. Lett. **82**, 4827 (1999).

[16] S. GROSSMANN AND D. LOHSE, *Intermittency in the Navier-Stokes dynamics*, Phys. B **89**, 11 (1992).

[17] O. S. M. BOIVIN AND K. SQUIRES, *Direct numerical simulation of turbulence modulation by particles in isotropic turbulence,* J. Fluid Mech. **375**, 235 (1998).

[18] M.R. MAXEY, E. CHANG, AND L.P. WANG, *Simulation of interactions between microbubbles and turbulent flows*, Appl. Mech. Rev. **47**, no. 6, S70 (1994).

[19] L.P. WANG AND M.R. MAXEY, *Settling velocity and concentration distribution of heavy-particles in homogeneous isotropic turbulence,* J. Fluid Mech. **256**, 27 (1993).

[20] C. YANG AND U. LEI, *The role of the turbulent scales in the settling velocity of heavy particles in homogeneous isotropic turbulence*, J. Fluid Mech. **371**, 179 (1998).

[21] R. E. G. POORTE, Ph.D. thesis, University of Twente, 1998.

[22] R. E. G. POORTE AND A. BIESHEUVEL, *Experiments on the motion of gas bubbles in turbulence generated by an active grid*, J. Fluid Mech. **461**, 127 (2002).

[23] J.M. RENSEN, S. LUTHER, J. DE VRIES, AND D. LOHSE, *Hot-film anemometry in bubbly flow I: bubble-probe interaction*, Int. J. Multiphase Flow **31**, 285 (2005).

[24] H. BRUUN, *Hot wire anemometry: principles and signal analysis*, Oxford University Press, Oxford (1995).

[25] J. DE VRIES, S. LUTHER, AND D. LOHSE, *Induced bubble shape oscillations and their impact on the rise velocity*, Eur. Phys. J. B **29**, 503 (2002).

[26] S. LUTHER AND J. RENSEN, Int. J. Multiphase Flow (submitted).

6

Energy Spectra in Microbubbly Turbulence[§]

Microbubbles ($R_0 = 100\mu m$) are injected in fully developed turbulence ($Re_\lambda = 200$) up to a volume concentration of 0.3%. An enhancement of the energy on small scales and a reduction on the large scales is observed, confirming theoretical prediction by Mazzitelli, Lohse, and Toschi, Phys. Fluids **15***, L5 (2003). The result is a (non-universal) less steep slope than $-5/3$ in the power spectrum.*

6.1 Introduction

The turbulent energy spectrum – apart from intermittency corrections – has been known since Kolmogorov 1941, $E(k) \propto k^{-5/3}$ [1]. How do bubbles modify this spectral energy distribution? The experimental and numerical results are far from conclusive: Lance and Bataille [2, 3] measured energy spectra in bubbly grid generated turbulence with hot film anemometry. They found an energy reduction at large scales and an energy enhancement at small scales. For increasing void fractions up to $\alpha = 3\%$ the $-5/3$ scaling exponent was progressively substituted by a $-8/3$ scaling law for large wavenumbers. Similar results were obtained in Refs. [4, 5]. In contrast, Mudde *et al.* [6], Mudde and Saito [7], and Cui and Fan [8] found for both pipe flow turbulence and bubble columns even for void fractions up to 25% the classical $-5/3$ scaling law.

On the numerical side Mazzitelli *et al.* [9, 10] performed numerical simulations with two-way coupled point-like bubbles, on which effective forces like drag, lift, added mass, (and buoyancy) were acting. A Taylor-

[§]See: Thomas H. van den Berg, Stefan Luther, and Detlef Lohse, *Energy spectra in microbubbly turbulence*, Phys. of Fluids **18**, 038103 (2006).

Reynolds number Re_λ of about 60 and a bubble volume concentration up to 1.6% could be achieved. Their main result was a reduction of the energy on the large scales, and an enhancement of the energy on small scales, resulting in a less steep spectral scaling of $-5/3$, see Fig. 6.1. This effect turned out to be mainly caused by the lift force which led to bubble accumulation on the downflow side of vortices, causing an upwards transfer of momentum and therefore an attenuation of the turbulence on large scales [9, 10]. Note that though the resulting spectra modifications through the microbubbles are similar as observed in turbulence with micro*particles* (see e.g. Figs. 3 and 4 of Ref. [11]), their *origin* is very different, as microbubbles accumulate in vortices, whereas (heavy) microparticles collect in low vorticity regions.

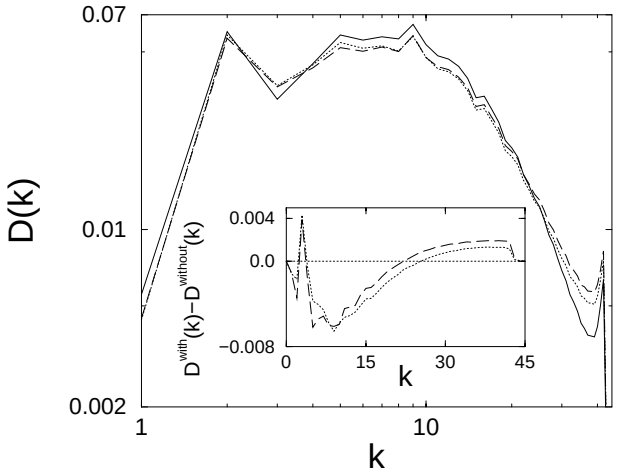

Figure 6.1: Dissipative spectra $D(k) = k^2E(k)$ for numerical single phase flow (solid) and two cases of bubbly flow with different bubble sizes (dashed), taken from Ref. [9]. The inset with the difference between the single phase dissipative spectrum and the ones for two-phase flow makes the energy reduction at large scales and the energy enhancement at small scales particularly visible. The energy reduction at large scales is roughly a 10% effect.

Can the numerically observed effect of microbubbles on turbulent spectra also be seen in experiment, at least qualitatively? After all, simplified models for the effective forces on the bubbles [12–15] had to be used. In particular, the lift force coefficient was simply assumed to be at its potential flow value $C_L = 1/2$ [16], though it is known that it strictly speaking

depends on both the local Reynolds number, the local shear, and the local rotation [12, 13].

6.2 Experiments

To find out, we performed experiments with bubbles with a volume concentration up to 3% in grid generated downward turbulent flow in the Twente water channel [17]. Due to an active grid [18] we can achieve as large Taylor-Reynolds number as $Re_\lambda = 240$. The typical bubble radius R_b was 1-2mm, corresponding to 10-20 Kolmogorov lengths η. The velocity spectra were deduced from hot-film measurements, employing a neural network type algorithm [17, 19, 20] to filter out the bubbly spikes [21] from the hot-film signal. Indeed, we obtained an energy spectrum with a slope less than $-5/3$, similar as in the numerical simulations [9, 10].

However, there were also several differences with the numerical simulations: (i) The less steep spectral slope was achieved through weak energy enhancement at large scales and strong energy enhancement at small scales. The reason for that was that for larger concentrations of the upwards rising bubbles the downward pumping strength had to be enhanced, in order to guarantee constant mean downflow velocity and thus be able to apply Taylor's hypothesis [1]. In this way an overall energy enhancement was unavoidable, due to the modified flow conditions. (ii) The bubbles in the experiment were 10-20 times larger than in the numerics (in terms of η). (iii) The bubble detection algorithm [17, 20] is complicated and in principle could introduce artefacts into the signal.

To overcome these difficulties, it is desirable to perform experiments as close as possible to the numerical simulations [9, 10]. The aim of this paper is to present the results of these experiments. The setup again is the Twente water channel described in detail in Refs. [17, 18], including the flow conditions. However, now we inject co-flowing *microbubbles* (typically $R_b = 100\mu m = 1\eta$). This is achieved upstream of the active grid by porous ceramic plates. We achieve void fractions up to 0.3%. The velocity of the liquid is again measured with hot film anemometry, but due the small size of the bubble, the bubble-probe interaction is reflected only in a sharp peak in the signal (see Fig. 6.2), which can easily be detected by a standard threshold method applied to the derivative of the signal and then be replaced by a linear fit [21]. Other fits of the gap like cubic splines give negligible differences.

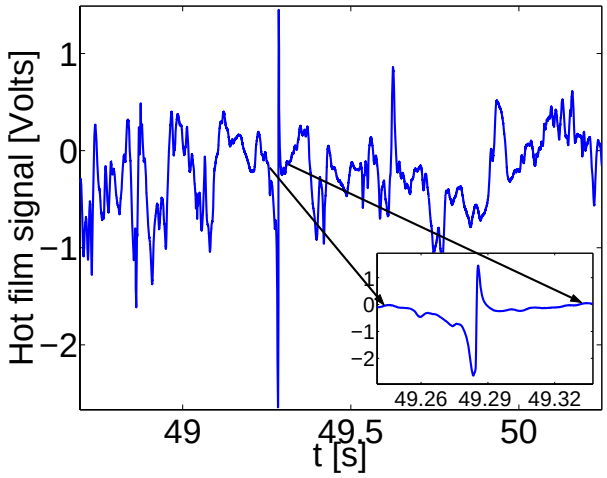

Figure 6.2: Hot film signal with a spike caused by a microbubble touching the hot film. The inset shows an enlargement of the spike.

6.3 Results

In Fig. 6.3 we show the power spectra for single phase flow and for bubbly turbulent flow for void fractions of 0.1% and 0.3%, both obtained from time series with a length of about 2400 large eddy turnovers.

The difference between single and two-phase flow spectra is small for these low void concentrations. To increase visibility, we plot the dissipative spectra $D(f) = f^2 E(f)$ in Fig. 6.4a. Qualitatively, the experimental results are similar to the numerical ones of Fig. 6.1. Again, as in the inset of Fig. 6.1a, the difference becomes particularly visible when we substract the dissipative spectra for the single phase and the two-phase case from each other, see Fig. 6.4b. For the 0.1% bubble concentration case the large scale reduction of the dissipative power is roughly a 10% effect and larger than the statistical error (which reflects itself in the wiggles of the curves). To check whether this result is robust, we split the time signal into two parts of 1200 large eddy turnover times each and repeated the analysis, leading to the same result. As compared to the statistical error, the error from reconstructing the spectra from segments is small, namely, less than 0.2%.

There are however quantitative difference between the experiments and the numerics, namely the less pronounced large scale reduction of

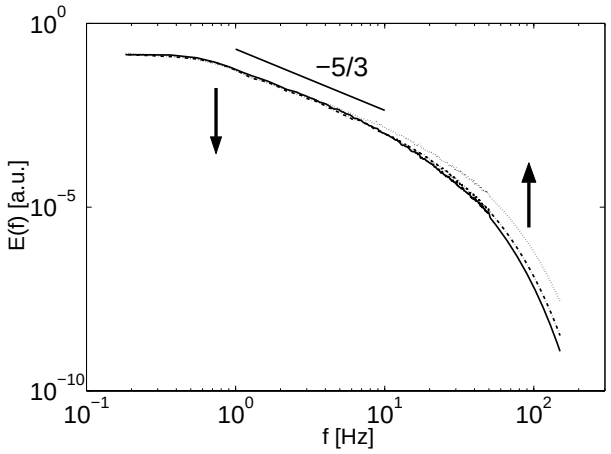

Figure 6.3: Power spectra $E(f)$ for single phase flow (solid) and the two-phase phase (dashed-dotted 0.1%, dotted 0.3% volume percentage). Note that for the analyzed very low bubble concentrations a measurement of the modification of the total energy (i.e., the integrated power spectrum) is not possible within our experimental precision.

the spectra for the case of 0.3% bubble concentration and more pronounced small scale spectral enhancement. Of course, the flow and bubble conditions are not identical in the numerics and the experiment. We speculate also about further differences: Possibly, the stronger energy reduction at large scales in the numerics can be interpreted as an indication that the employed lift coefficient $C_L = 1/2$ [9, 10] is too large and should be viewed as upper bound. This would be supported by calculations done in [10]: when taking a smaller lift coefficient the energy reduction at large scales is less pronounced. The stronger energy input at small scales in the experiments could also have its origin in a contamination of the bubbles, leading to stress free boundary conditions at their surface, as compared to the slip boundary conditions employed in the numerics.

6.4 Conclusion

In table 6.1 we compare the flow and bubble characteristics for the numerical turbulence of Ref. [9, 10] and the microbubbly turbulence analyzed here. The bubble size in terms of η, the bubble Reynolds number,

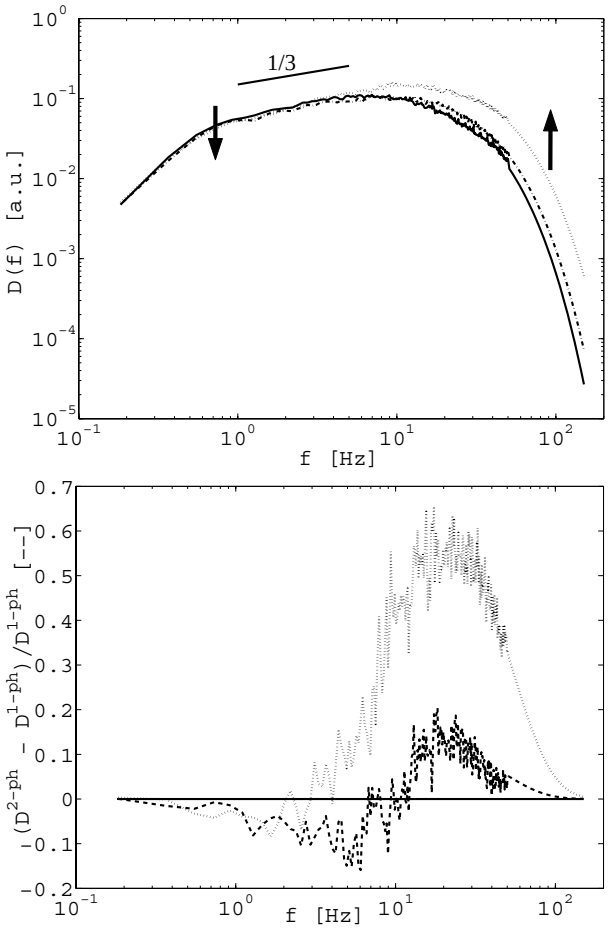

Figure 6.4: (a) Dissipative spectra $D(f) = f^2 E(f)$ for single phase flow (solid) and two-phase flow (dashed-dotted 0.1%, dotted 0.3% volume percentage). (b) The difference between the single phase dissipative spectrum and the ones for two-phase flow (dashed 0.1%, dotted 0.3% volume percentage). This way of plotting makes the energy reduction at large scales and the energy enhancement at small scales particularly visible. The plot is the experimental correspondence to the numerical result for this difference shown in the inset of Fig. 6.1. For the 0.1% bubble volume concentration, the large scale reduction is again roughly a 10% effect.

and also the 'bubblance' parameter [17]

$$b = \frac{\frac{1}{2}\alpha U_R^2}{u'^2} \tag{6.1}$$

are very similar. The bubblance parameter (which one also may want to call 'burbulence' parameter) compares the typical kinetic energy of the bubbles (which is $\alpha U_R^2/2$ where U_R is the bubble rise velocity in still water) with the typical kinetic energy u'^2 of the velocity fluctuations. Both the numerical bubbly turbulence and the microbubble turbulence are in a regime of small $b \ll 1$, which is the regime where the bubbles can only slightly modify the turbulence. In contrast, the experiments by Lance and Bataille [3] are in a regime with up to $b = 10$, and it is that large b regime or "bubblance" regime where the $-8/3$ scaling exponent is observed. However, note that apart from this additional scaling feature the two-phase flow energy spectra by Lance and Bataille [3], by our predictions based on the numerical simulations [9, 10], and by our microbubble experiments (this work) are qualitatively all the same: An enhancement at small scales and an attenuation at large scales.

	flow	method	Re_λ	R_b/mm	Re_b	$\frac{R_b}{\eta}$	α(%)	b	spectral exponent
Mazzitelli, Lohse, & Toschi [9, 10]	spectral Navier-Stokes code	two-way coupling	60	0.1	1-6	1	0-1.6	0 - 0.02	slightly less steep than $-5/3$
this work	grid generated turbulence, co-flow	hot-film	240	0.1	2	1	0-0.3	0-$2 \cdot 10^{-3}$	slightly less steep than $-5/3$

Table 6.1: Comparison between the flow and bubble characteristics for the numerical bubbly turbulence of Refs. [9, 10] with the present experimental analysis. Re_λ the Taylor-Reynolds number, R_b is the bubble radius, $Re_b = R_b U_R/\nu$ the bubble Reynolds number of a rising bubble in clean still water, η the Kolmogorov length scale, α the gas fraction, and b the bubblance parameter defined in Eq. (6.1). For an extensive overview of the flow and bubble characteristics for various other flows we refer to Ref. [17].

References

[1] S. B. POPE, *Turbulent Flow*, Cambridge University Press, Cambridge (2000)
U. FRISCH, *Turbulence*, Cambridge University Press, Cambridge (1995).

[2] M. LANCE AND J. BATAILLE, in *Proceedings of NATO Specialist's Meeting, Spitzensee, Germany*, (Martinus Nijhoff Publishers, 1983).

[3] M. LANCE AND J. BATAILLE, *Turbulence in the liquid phase of a uniform bubbly air-water flow*, J. Fluid Mech. **222**, 95 (1991).

[4] I. MICHIYOSHI AND A. SERIZAWA, in *Proceedings Japan-US Seminar on two-phase flow dynamics, July 29 - August 3, 1984, Lake Placid, USA* (1984).

[5] S. K. WANG, S. J. LEE, O. C. JONES, AND R. T. LAHEY, *Statistical Analysis of Turbulent Two-Phase Pipe Flow*, J. Fluid Eng. **112**, 89 (1990).

[6] R. F. MUDDE, J. S. GROEN, AND H. E. A. VAN DEN AKKER, *Liquid velocity field in a bubble column: LDA experiments*, Chem. Eng. Science **52**, 4217 (1997).

[7] R. F. MUDDE AND T. SAITO, *Hydrodynamical similarities between bubble column and bubbly pipe flow*, J. Fluid Mech. **437**, 203 (2001).

[8] Z. CUI AND L. S. FAN, *Turbulence energy distribution in bubbling gas-liquid and gas-liquid-solid flow systems*, Chem. Eng. Science **59**, 1755 (2004).

[9] I.M. MAZZITELLI, D. LOHSE, AND F. TOSCHI, *The effect of microbubbles on developed turbulence*, Phys. Fluids **15**, L5 (2003).

[10] I.M. MAZZITELLI, D. LOHSE, AND F. TOSCHI, *On the relevance of the lift force in bubbly turbulence*, J. Fluid Mech. **488**, 283 (2003).

[11] S. ELGHOBASHI AND G. TRUESDELL, *On the two-way interaction between homogeneous turbulence and dispersed solid particles. I: Turbulence modification*, Phys. Fluids A **5 (7)**, 1790 (1993).

[12] J. MAGNAUDET AND I. EAMES, *The motion of high-Reynolds number bubbles in inhomogeneous flows*, Ann. Rev. Fluid Mech. **32**, 659 (2000).

[13] J. MAGNAUDET AND D. LEGENDRE, *Some aspects of the lift force on a spherical bubble*, Appl. Sci. Res. **58**, 441 (1998).

[14] D. LOHSE AND A. PROSPERETTI, *Controlling bubbles*, J. Phys.: Condens. Matter **15**, S515 (2003).

[15] J. MAGNAUDET, *Small inertial effects on a spherical bubble, drop or particle moving near a wall in a time-dependent linear flow*, J. Fluid Mech. **485**, 115 (2003).

[16] T. R. AUTON, J. HUNT, AND M. PRUD'HOMME, *The force excerted on a body in inviscid unsteady non-uniform rotating flow*, J. Fluid Mech. **197**, 241 (1988).

[17] J. M. RENSEN, S. LUTHER, AND D. LOHSE, *Velocity structure functions in turbulent two-phase flows*, J. Fluid Mech. **538**, 153 (2005).

[18] R. E. G. POORTE AND A. BIESHEUVEL, *Experiments on the motion of gas bubbles in turbulence generated by an active grid*, J. Fluid Mech. **461**, 127 (2002).

[19] J.M. RENSEN, S. LUTHER, J. DE VRIES, AND D. LOHSE, *Hot-film anemometry in bubbly flow I: Bubble-probe interaction*, Int. J. Multiphase Flow **31**, 285 (2005).

[20] S. LUTHER, J.M. RENSEN, T.H. VAN DEN BERG, AND D. LOHSE, *Data analysis for hot-film anemometry in turbulent bubbly flow*, Exp. Thermal and Fluid Science **7**, 821-826 (2005).

[21] H. H. BRUUN, *Hot wire anemometry: principles and signal analysis*, Oxford University Press, Oxford (1995).

7

Microbubble clustering in turbulent flow §

Single-point hot-wire measurements in the bulk of a turbulent channel have been performed in order to detect and quantify the phenomenon of preferential bubble accumulation. We show that statistical analysis of the bubble-probe colliding-times series can give a robust method for investigation of clustering in the bulk regions of a turbulent flow where, due to the opacity of the flow, no imaging technique can be employed. We demonstrate that micro-bubbles ($R_0 \simeq 100\ \mu m$) in a developed turbulent flow, where the Kolmogorov length-scale is $\eta \simeq R_0$, display preferential concentration in small scale structures with a typical statistical signature ranging from the dissipative range, $\mathcal{O}(\eta)$, up to the lower end of inertial range, $\mathcal{O}(100\eta)$. A comparison with Eulerian-Lagrangian numerical simulations is also performed and arising similarities and differences are discussed.

7.1 Introduction

The phenomenon of preferential concentration of small particles and bubbles in turbulent flows enjoys increasing attention in recent years, the studies ranging from experimental works, [1], to numerical investigations, [2–5] and theory developments, [6, 7]. Preferential accumulation may be understood as an inertial effect. Due to inertia the Lagrangian particle/bubble velocity is not always aligned with the surrounding incompressible fluid flow velocity and this leads to the consequence that particles heavier than the fluid are on average ejected from vortices, while light buoyant particles tend to accumulate in high vorticity regions.

§See: Enrico Calzavarini, Thomas H. van den Berg, Stefan Luther, Federico Toschi, and Detlef Lohse, *Microbubble clustering in turbulent flow*, submitted to J. Fluid Mech.
T. H. v. d. Berg is responsible for the experimental results.

The scenario is complicated by the fact that a certain number of other physical effects may play a role. First, apart from body forces like gravity and added mass, there are in general surface forces acting on the particles, as for example drag and lift, whose expressions especially in unsteady flow conditions are not completely understood. For a discussions on the dynamics of a single particle settling in still fluid and for the rise of a single bubble we refer to [8–11]. Such forces may in principle produce additional non trivial effects on the clustering mechanism. Secondly, the coupling of the disperse phase on the fluid flow (*two-way* coupling) and the finite-size effect of particle-particle interaction (*4-way* coupling) may also result in non-negligible factors of perturbation for preferential concentration of particles in highly turbulent flows.

Small air bubbles in water, below the millimeter size, i.e. of typical Reynolds number of order $\mathcal{O}(1)$, can be regarded as a particular kind of non-deformable light spherical particles with density negligibly small compared to the fluid one. In fact, in this size-range, shape oscillations or deformations and wake induced effect can be reasonably neglected. Strong preferential accumulation in core vortex regions is therefore expected according to the inertia mechanism, see for instance the experimental visualizations realized by Douady *et al.* [12]. An explorative experimental investigation on the relevant features of microbubbles clustering in a developed turbulent flow is the focus of the present paper.

Experimental measurements on bubbly laden turbulent flows are challenging. Even at very low void fractions ($\sim 1\%$) the fluid tends to be completely opaque and difficult, if not impossible, to access with external optical methods, especially in the bulk region of the flow. Recently, we have performed a series of experiments in order to understand the effect of bubbles, [13], and microbubbles, [14], on the turbulent energy spectra. Numerics based on Eulerian-Lagrangian description also have been successfully employed to predict the same effects in similar flow conditions, [15, 16]. In particular, it has been demonstrated that for low void fractions, up to few percents, microbubbles induce an energy decrease at large scales and an energy enhancement at small scales. For these kind of experiments, where the main focus was on fluid velocity, a traditional *intrusive* hot-wire anemometer has been adopted, the disturbances associated to bubbles hitting the probe were successively identified and filtered out when computing fluid turbulent spectra, [17, 18].

One could object that measurement from one fixed point in space are too intrusive because they can destroy the clusters, or that they are ineffective in extracting features of the bubble trapping in turbulent vorti-

cal structures. However, in this paper we analyze the series of the bubble colliding times on the hot-wire probe from the Twente experiment by means of appropriate statistical indicators. We show that it is possible to detect and quantify the micro-bubble clustering from a one-point measurement set-up. We compare experimental findings with results from numerical simulations based on Eulerian-Lagrangian approach. Due to limitations that we will discuss later, at best only a qualitative agreement among numerics and experiments is expected. Nevertheless, we show how this comparison is helpful in clarifying the trend in the clustering at changing the turbulent conditions.

7.2 Experiment

The experimental set-up, as previously mentioned, is the Twente water channel, a vertical duct of square cross section with dimension $200cm \times 45cm \times 45\ cm$, we refer to Rensen *et al.* [13] for a detailed description. An array of porous ceramic plates, positioned on the top of the channel, is used to generate co-flowing small bubbles of average radius, $R_0 \simeq 100\mu m$, as described in [14]. Fluid turbulence is generated by means of an active grid, positioned immediately downstream the bubble injection sites. The typical flow is characterized by a large mean flow, U, with turbulent fluctuations, $u' \equiv u_{rms}$, of smaller amplitude. The condition $u'/U \ll 1$ assures that Taylor's frozen-flow hypothesis can be applied. The dissipative Kolmogorov scale measures typically $\eta = 400 - 500\ \mu m$, while the Taylor micro-scale and the integral one, are respectively $\lambda \simeq 30\ \eta$, and $L_0 \simeq 4 - 5 \cdot 10^3\ \eta$. The typical bubble size is of the same order, or weakly smaller, than η.
We consider microbubble signals extracted from a hot-film anemometry probe (300 μm in size) fixed at the center of the channel. Detection of micro-bubbles is luckily less ambiguous than for large bubbles where probe piercing and break-up events are highly probable [19]. A microbubble hitting the probe produces a signal with a clear spike and the bubble can be identified by threshold check on the velocity time-derivative signal, see Fig. 7.1. This identification procedure leads to the definition of a minimal cut-off time in the capability to detect clustered events, two consecutive bubbles in our records cannot have a separation time smaller than $\tau = 10^{-2} sec$. Such dead-time is mainly linked to the typical response-time of the acquisition set-up. Here we consider two time series of microbubble measurements, i.e. hitting times, selected from a larger

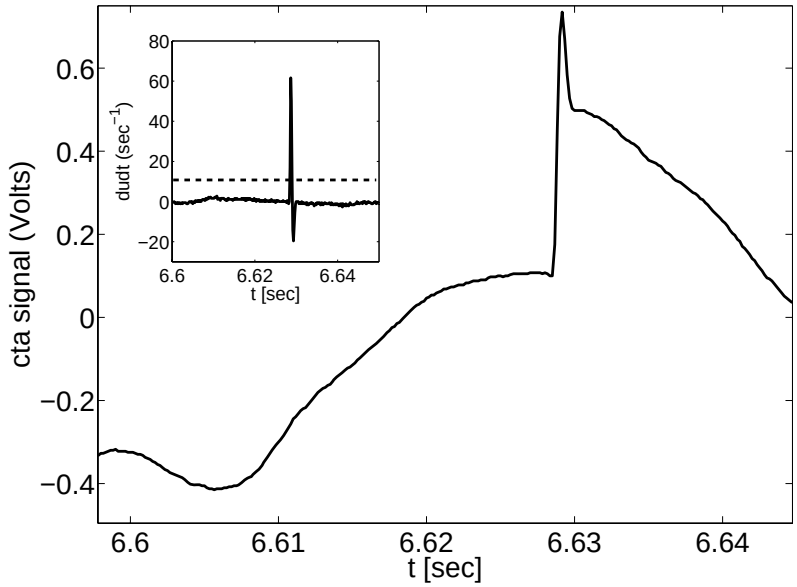

Figure 7.1: A typical voltage, $V(t)$, signal from the hot-wire anemometer, a spike is produced by a hitting micro-bubble. Due to the internal electrical impedance of the acquiring set-up we consider the signal's perturbation fully restored after 10^{-2} sec. The inset shows for the same event, the voltage time derivative normalized by the mean velocity standard deviation (dudt). The dotted line shows the level of the threshold adopted for bubble identifications.

database because of their uniformity and relevant statistics, we will refer to them in the following as sample (a) and (b). The first sample (a) has been taken for a 12 hours long measurement; it consists of $N_b = 24099$ bubbles with a mean hitting frequency $f = 0.56\ sec^{-1}$. The second sample, (b), is a record of 11 hours, $N_b = 11194$ and $f \simeq 0.28\ sec^{-1}$. There are two main differences among the experimental conditions in which the two samples have been recorded, that is the total volume void fractions (α) and the amplitude of the mean flow and therefore the intensity of turbulence. Case (a) has a void fraction of $\approx 0.3\%$ and (b) has a void fraction of $\approx 0.1\%$. Given the small effect produced by the dispersed bubbly phase on the turbulent cascading mechanism, [14], we consider the discrepancy in α as irrelevant for the velocity spectra. In contrast, the difference in the forcing amplitude is more important, because it changes sensibly all the

relevant scales of turbulence as summarized in Table 7.1.

In particular, this leads to different values for the minimal experimentally detectable scale: $\Delta r_{min} \simeq 5\eta$ for case (a) and $\Delta r_{min} \simeq 3\eta$ for (b), where Taylor hypothesis has been used to convert time to space measurements, i.e. $\Delta r = \tau \cdot U$. In the following, results of our analysis will be presented by adopting space units made dimensionless by the Kolmogorov scale η, we consider this re-scaling more useful for comparison with different experiments and simulations where a mean flow may be absent.

7.2.1 Methods

In this section we present the statistical tests we will adopt to quantify the clustering. A first way to assess the presence of preferential concentrations in the experimental records is to compute the probability density function (pdf) of the distance, Δr, between couples of successive bubbles. We note that the pair-separation pdf corresponding to a random and homogeneous distribution follows the exponential form, $\rho \exp(-\rho \Delta r)$, where $\rho = f/U$ is the mean rate of bubbles per unit length. In general, one expects that for large enough separation-scales the exponential form of the pdf is recovered. In fact, pairs of successive bubbles with large separations Δr, larger then any structures in the flow, are uncorrelated, memory-less, events. However, due to the possible accumulation on small scales the long tail of the pdf may have an exponential decay rate that is different from the global mean, ρ. The tail of the experimentally measured pdf can be fitted with an exponentially decaying function, $A \cdot \exp(-\rho_h \Delta r)$, with a rate that we call ρ_h, where h stands for homogeneous. In case of small-scale clustering we expect ρ_h to be smaller than ρ. As an indicator of the fraction of bubbles accumulated in turbulent structures, we use the coefficient $\mathcal{C} \equiv 1 - \rho_h/\rho$, whose value varies in between 0 and 1.

A second statistical test is particularly useful to reveal the scales at which the non-homogeneity first takes place. The idea is to compute the coarse-grained central moments of the number of bubbles, on a window of variable length r, $\mu_r^p \equiv \langle (n - \langle n \rangle_r)^p \rangle_r$. From them several relevant statistical observables can be derived. We will focus here on scale dependent Kurtosis, $K(r) \equiv \mu_r^4/(\mu_r^2)^2 - 3$, and Skewness excess, $S(r) \equiv \mu_r^3/(\mu_r^2)^{3/2}$. A random spatially homogeneous distribution of particles with mean rate ρ corresponds to a Poisson distribution of the form
$p(n) = \exp(-\rho\, r)(\rho r)^n (n!)^{-1}$, where r is the length of the spatial window considered and n is the number of events expected in it. Therefore, once the particle space rate ρ is given, the value of any statistical moments and

their combinations can be derived for the corresponding window length r. Homogeneous and random statistics for instance implies the functional dependencies $K(r) = (\rho r)^{-1}$ and $S(r) = (\rho r)^{-1/2}$. Furthermore, we note that at the smallest scale, when $r = \Delta r_{min}$, we reach the singular limit (shot-noise limit) where for any given space-window we can find only 1 or 0 bubbles. Therefore all the statistical moments collapse to the same value. This latter limit, which is by the way coincident with Poisson statistics, represents our minimal detectable scale. We are interested in departures from the shot-noise/random-homogeneous behavior for the statistical observables $K(r)$ and $S(r)$.

7.2.2 Results

In Fig. 7.2 we show in a Linear-Log plots the computed pdf(Δr) for the two data samples considered. Deviations from global homogeneity are clear if the shape of the histogram is compared with the solid line representing the pdf $\rho \cdot \exp(-\rho \Delta r)$. These deviations are weakly more marked in case (a), the most turbulent, than case (b). Nevertheless, one can notice that the pure exponentially decaying behavior, i.e. homogeneity, is recovered from distances of the order of $\mathcal{O}(100\eta)$ up to the large scales. The dotted line on Fig. 7.2, which represents the linear fit on the long homogeneous tail in the interval $[10^3, 2 \cdot 10^3]\eta$, and the inset boxes, where the pdf is compensated by the fit, shows this latter feature. The evaluation of the coefficient $\mathcal{C}$ leads to values for the relative bubbles excess in clusters corresponding to 19 % for case (a) ($Re_\lambda \simeq 206$) and 10 % for case (b) ($Re_\lambda \simeq 180$), confirming the trend of stronger concentration in flows with stronger turbulence level. In Fig. 7.3 we show the Kurtosis and Skewness behavior, evaluated for the two cases (a)-(b), in a comparison with the Poissonian dependence. We observe in both cases a clear departure at small scale from the scaling implied by the global homogeneity, this behavior is then recovered at large scale ($\gtrsim 500\eta$) where the data points falls roughly parallel to the Poisson line. The departure from the Poisson line, that is noticeable already at the scales immediately above Δr_{min}, is an indication that bubbles form clusters even at the smallest scale we are able to detect, that is even below 5η for case (a) or 3η for case (b). We observe that for the less turbulent case, (b), the departure from the homogeneous scaling is less marked. A comparison with synthetic Poisson samples of an equivalent number of bubbles, that we have tried, shows that although limited, the available statistics is enough to validate the deviations from the homogeneity discussed so far. Scale dependent deviation from Pois-

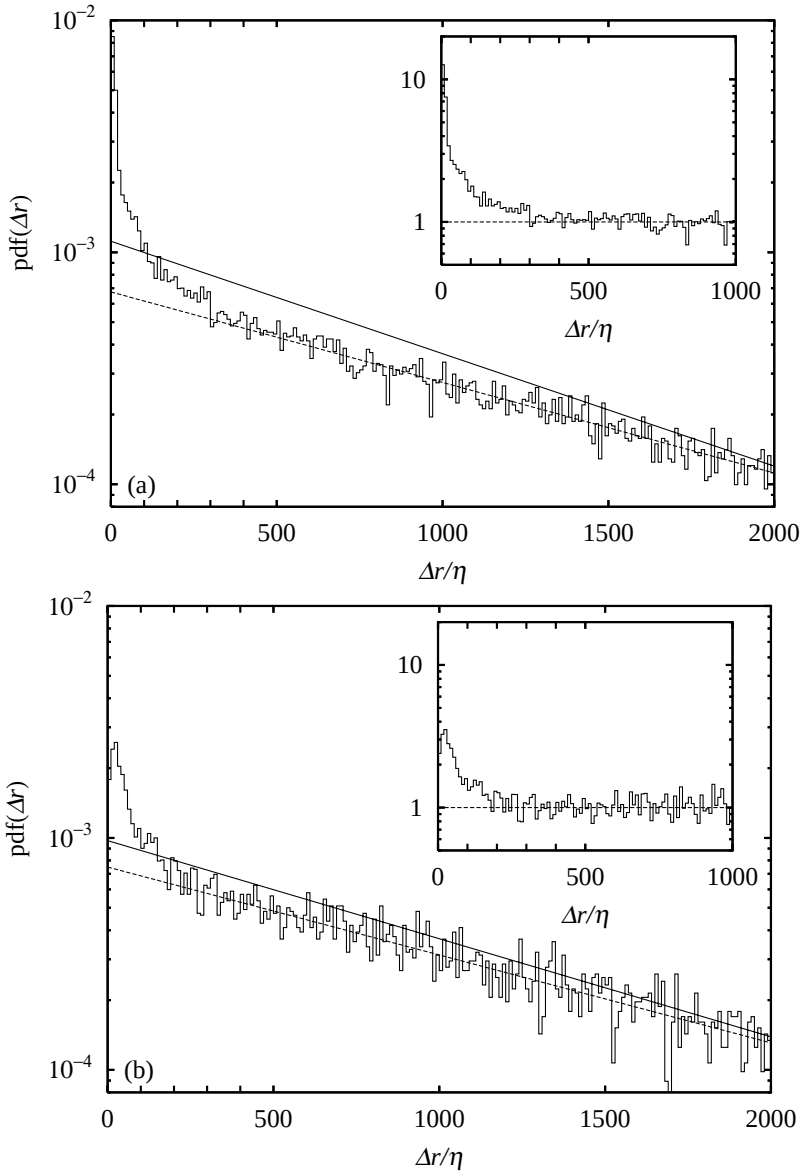

Figure 7.2: Linear-log plot of the probability density function of distance between successive bubbles, pdf(Δr). Exponential behavior, $\rho e^{-\rho \Delta r}$, (solid line) and exponential fit ($A \cdot e^{-\rho_h \Delta r}$) of the large-scale tail (dashed line) are reported. The inset shows the pdf(Δr) compensated by the fitted large-scale exponential behavior, i.e. pdf(Δr) divided by $A \cdot e^{-\rho_h \Delta r}$.

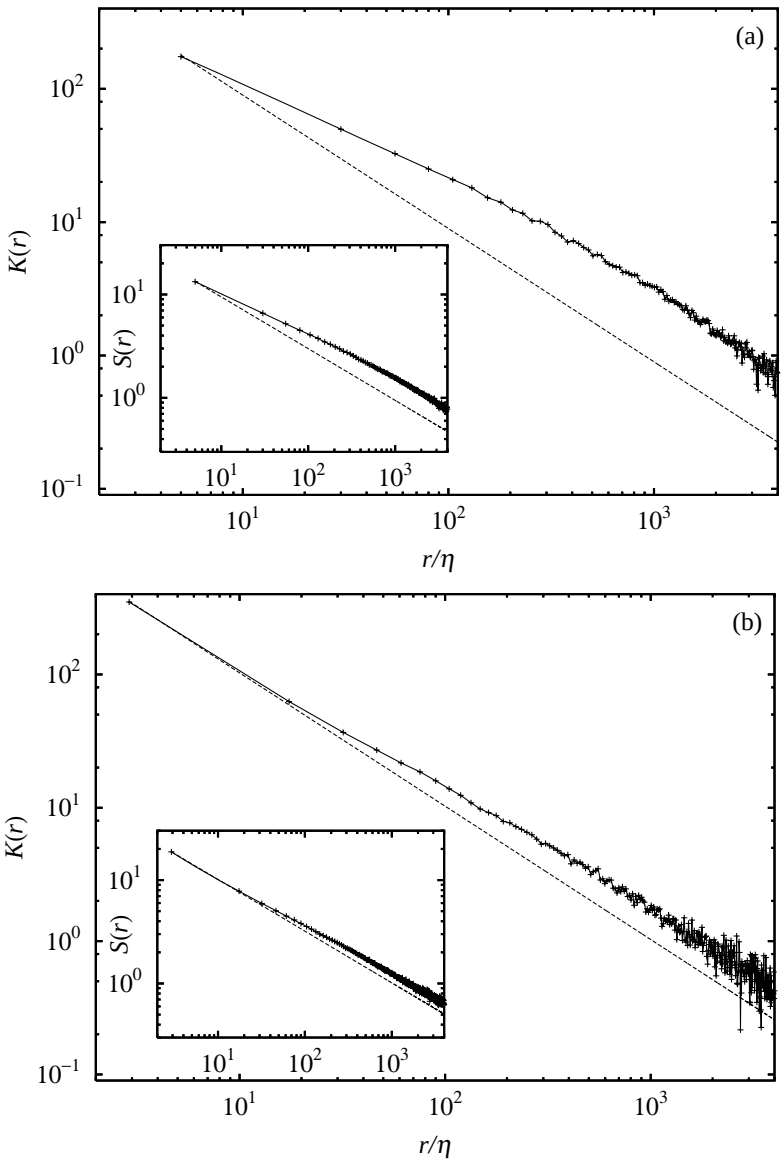

Figure 7.3: Log-log plot of scale dependent Kurtosis, $K(r)$, for case (a) (top) and (b) (bottom). Dotted lines represent the Poissonian behavior, that is $K_{(P)}(r) = (\rho\, r)^{-1}$. Notice that the Poisson scaling behavior is reached for large r-windows only scaling wise. In the insets the scale dependent Skewness, $S(r)$, behavior is shown. Again the Poissonian relation is drawn $S_{(P)}(r) = (\rho\, r)^{-1/2}$ (dotted line).

son distribution is an evidence of the fact that the dispersed microbubbles are trapped within the dynamical vortical structures of turbulence. Furthermore, we observe that gravity plays a minor role in this dynamics. In fact, as it can be noticed in Tab. 7.1, on average the bubbles are swept down by the large mean flow, i.e. $v_T/U \ll 1$. It is mainly the inertia that drives the bubble accumulation in the flow.

7.3 Simulations

Is the picture drawn from experiment also confirmed by present numerical simulations? Despite the many improvement in numerical methods for multi-phase flows achieved in recent years, as for instance the reliable class of front-tracking methods, [20], the only scheme today available for the study of a dispersed multi-phase flow in the conditions of high fluid turbulence, i.e. large-scale separation, and large number of bubbles is the Eulerian-Lagrangian approach. According to this scheme the fluid is described by the Navier-Stokes equation. Bubbles are treated as point-particles with an equation of motion accounting for the effective forces acting on them, namely added mass, drag, buoyancy, lift and history forces, as already mentioned in the introduction. Our knowledge of these forces, even in the simplified case of $Re_b \sim \mathcal{O}(1)$, is only approximate. Therefore the Eulerian-Lagrangian approach can only be considered as a phenomenological method. In this study we assume the limit of negligible air density compared to water to hold, $\rho_g/\rho_f \to 0$, which fixes the inertia term. We use the spherical added mass coefficient, $C_M = 1/2$, drag coefficient for the steady Stokes flow ($Re \ll 1$), $C_D = 16/Re$, buoyancy, the Auton's expression for the lift force with lift coefficient $C_L = 1/2$, [21], and finally we neglect the history force, [22]. The bubble's velocity equation of motion we adopt is therefore the following, [15, 16, 23–25]:

$$\frac{d\boldsymbol{v}}{dt} = 3\frac{D\boldsymbol{u}}{dt} - \frac{1}{\tau_b}(\boldsymbol{v}-\boldsymbol{u}) - 2\boldsymbol{g} - (\boldsymbol{v}-\boldsymbol{u})\times\boldsymbol{\omega} \tag{7.1}$$

where $\boldsymbol{u}$ and $\boldsymbol{\omega}$ are respectively the fluid velocity and vorticity computed at the bubble position. In previous numerical studies based on the same description of the multi-phase system Mazzitelli *et al.* [16, 26], pointed out that bubbles can strongly concentrate in turbulent vortical filaments: we refer in particular to Figure 1(a) of [26]. How does this look like from a single point probe measurement? And how does this change at varying the turbulence intensity? To address these questions, we attempt a

numerical test of the two-phase system. The flows is homogenous and isotropic turbulence in a periodic box, of resolution 128^3, seeded approximately with 10^5 bubbles, corresponding to a void fraction $\alpha = 2.5\%$. Since previous experimental and numerical studies by van den Berg *et al.* [14] and Mazzitelli *et al.* [15] have revealed that the effect of bubbles on strong unbounded turbulence is relatively weak, our numerical bubbles are only coupled in one-way mode to the fluid, i.e. bubbles do not affect the fluid phase. The bubble-Reynolds number Re_b is set to unity, the bubble radius is of order η, the Stokes number is $St \ll 1$, and the bubble terminal velocity v_T in still water is much smaller than the large scale flow, u'. Therefore, as in the experiment, the role of gravity is marginal.

In Table 7.2 we report the characteristics of the simulated flow, they are similar to the ones displayed in the experiment. We however can not reach the same scale separation as displayed by our turbulence experiments. Therefore, in order to have a better comparison with the scales of the real world we give, on the bottom panel of Tab.7.2, the physical equivalent quantities of our numerics. We note also that in the numerics the Stokes number, $St = \tau_b/\tau_\eta$, which is an indicator of the degree of bubble interaction with turbulence, can not be as low as in the experiments unless at the price of highly time demanding computations. In fact to correctly resolve the motion of the bubble the computational time step (dt) shall be always adjusted to satisfy the relation $dt \ll \tau_b$, increasing sensibly the computational needs. For practical reason the Stokes values adopted in our numerics are roughly one order of magnitude larger than in the experiments, but always much below unity, $St \ll 1$. Under this conditions, spatial visualizations show strong bubble accumulation in nearly one-dimensional elongated structure in correspondence to high enstrophy regions, identified as vortex filaments [26].

To detect bubbles clustering in a similar way to the experiments, we put 128 virtual point-like probes in the flow and recorded the hitting time of bubbles, giving them a virtual radius, R_0. We note that the bubble radius is linked to the typical bubble response time, τ_b, via the relation, $R_0 \equiv (6\tau_b\nu)^{1/2}$, implying free-slip boundary conditions at the gas-fluid interface. Another distinction between the experiment and our numerics that we shall mention is on the mean flow: active in the experiment while intrinsically suppressed in the simulations. In the numerics time is connected to space displacement by mean of the relation $\Delta R = \Delta t \cdot u'$, where, u', is the root mean square velocity. The level of turbulence, given the available resolution, has been pushed as high as possible ($Re_\lambda \simeq 90$)

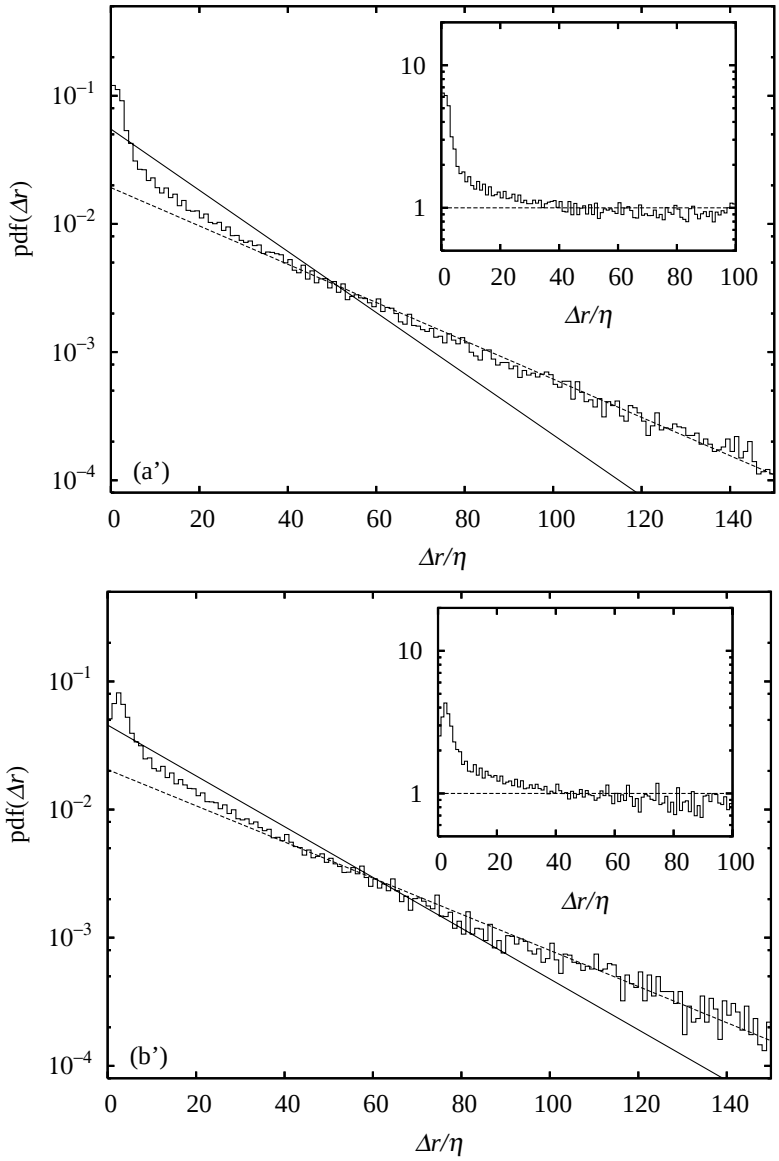

Figure 7.4: Linear-Log plot. Numerical result on the probability density function of distance between successive bubbles, pdf(Δr). Case (a') (top) is the most turbulent. In the inset the same compensated plot as in Fig. 7.2

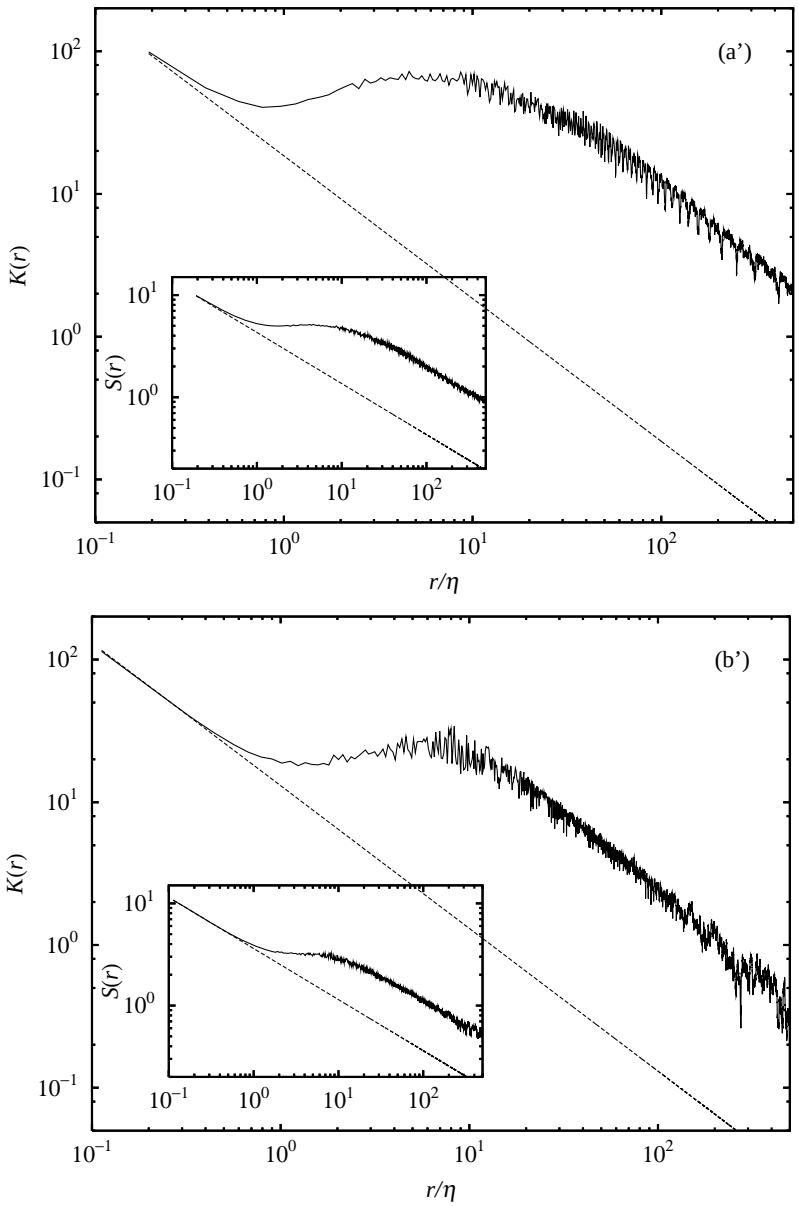

Figure 7.5: Log-Log plot. Numerical result on scale dependent Kurtosis, $K(r)$, for case (a') (top) and (b') (bottom), and Poissonian behavior (dotted). In the insets the scale dependent Skewness, $S(r)$, behavior is shown.

to obtain a better analogy with the experiment. Furthermore also in the numerics two cases are considered, we vary the amplitude of the external forcing while we keep the bubble size constant, see again Tab. 7.2.

We show in Fig. 7.4 and Fig. 7.5 our results for the statistical analysis of clustering from the numerical virtual probes. These two figures are compared with the analogous experimental findings already discussed and shown in Fig. 7.2 and 7.3. Some qualitative similarities are striking. First, starting from Fig. 7.4, we observe that deviations from random and homogeneous, i.e. pure exponential behavior, are relevant at small scales. This feature is confirmed by the scale dependent Kurtosis and Skewness of Fig. 7.5, where departure from the Poisson scaling already starts below η scale. Second, the most turbulent case is the most clusterized, (a') ($Re_\lambda \simeq 95$) more than (b') ($Re_\lambda \simeq 91$). The evaluation of the fraction of clustered bubbles, based on the fit of the pdf(Δr) as in the experiment, gives the value 29% for (a') and 37% for (b'). Nevertheless, even if the qualitative behavior of the statistical indicators adopted are the same, important differences arise in this comparison and they shall be discussed too. Full homogeneity in the numerics seems to be recovered at scales of order $\mathcal{O}(10\eta)$, this is not the case in the experiments where we reach $\mathcal{O}(100\eta)$ scales, furthermore the deviations from Poisson distribution and the fraction of clustered bubbles are definitely stronger in the numerics. There is more than one possible interpretation for this mismatch. Here we would like to mention what we consider more relevant besides the possible incompleteness of the model, on which we have already commented at the beginning of this section. We first note that some known physical effects have been neglected so far: the fluid-bubble and the bubble-bubble couplings and the associated finite size effects (in the present conditions bubbles can overlap!). A second reason can be the different degree of bubble interaction with turbulence, a quantity that is parameterized by the Stokes number $St = \tau_b/\tau_\eta$. The estimated St in the experiment is roughly one order of magnitude smaller than in the simulation, this corresponds to bubbles that react faster to the fluid velocity changes and hence to bubbles that follow closely the fluid particles and accumulate less. Such a trend is also confirmed by our numerics.

7.4 Conclusions

We have performed statistical tests in order to detect and characterize the bubble preferential concentration phenomenon from single-point hot-

wire anemometer measurements in the bulk of a turbulent channel. We have shown that our experimental records clearly display bubble clustering. The fraction of bubbles trapped in such structures is relevant and estimated to be of the order of 10%. The scale-dependent deviations from random homogeneous distribution, that we associate to typical cluster dimension, extend from the smallest detectable scale, $\mathcal{O}(\eta)$, to scales in the lower inertial range, $\mathcal{O}(100\eta)$. Accumulation of bubbles is enhanced by increasing the turbulence intensity. Comparison with present Eulerian-Lagrangian simulations, where point-like bubbles strongly accumulate in vortex core regions, shows similar qualitative features and trends.

We hope this work will stimulate new dedicated experiments to further quantify the clustering dynamics at changing turbulence intensity and bubble concentration. For instance, an analysis on the statistics of fluid velocity signal just before a bubble arrives on the probe could be interesting to determine the influence of the lift force on the bubble spreading. In fact it is thought that, due to the combined effect of buoyancy and lift, bubbles shall accumulate preferentially in down-flow sides of vortices, [16]. Unfortunately, a corresponding analysis of our experimental data has hitherto not been successful, presumably due to flow contaminations by small impurities.

	$U\ (cm/s)$	$u'\ (cm/s)$	Re_λ	$\tau_{eddy}\ (s)$	$\tau_\eta\ (ms)$	$\eta\ (\mu m)$	$v_\eta\ (\mu m/s)$	Re_b	R_0/η	St	v_T/U
a)	19.4	1.88	206	12.0	151.	388.	6.63	4.4	0.26	0.007	0.11
(b)	14.2	1.39	180	16.6	240.	489.	4.17	4.4	0.20	0.004	0.15

Table 7.1: Relevant turbulent scales and bubble characteristics for the two experimental samples analyzed. Fluid turbulent quantities have been estimated from one-dimensional energy spectra.

	L_0	u'	Re_λ	τ_{eddy}	τ_η	η	v_η	Re_b	R_0/η	St	v_T/u'
(a')	2π	2.4	95	3.0	0.093	0.025	0.275	1.0	0.94	0.14	0.06
(b')	2π	1.8	91	5.6	0.148	0.032	0.217	1.0	0.73	0.09	0.08
	$L_0\,(cm)$	$u'\,(cm/s)$	Re_λ	$\tau_{eddy}\,(s)$	$\tau_\eta\,(ms)$	$\eta\,(\mu m)$	$v_\eta\,(cm/s)$	Re_b	R_0/η	St	v_T/u'
(a')	1.43	14.9	95	0.1	3.4	57	1.7	1.0	0.94	0.14	0.06
(b')	1.43	11.2	91	0.2	5.4	73	1.4	1.0	0.73	0.09	0.08

Table 7.2: Relevant turbulent scales and bubble characteristics for the two numerical simulation performed. The top part reports the actual values in numerical units from the simulation, the bottom part shows for comparison the corresponding physical equivalent quantities for air bubbles in water, this is to better appreciate similarities/differences with the experimental conditions of Table 7.1.

References

[1] J. FESSLER, J. KULICK, AND J. EATON, *Preferential concentration of heavy particles in a turbulent channel flow*, Phys. Fluids **6**, 3742 (1994).

[2] M. R. MAXEY, *The gravitational settling of aerosol particles in homogeneous turbulence and random flow fields*, J. Fluid Mech. **174**, 441–465 (1987).

[3] K. SQUIRES AND J. EATON, *Preferential concentration of particles by turbulence*, Phys. Fluids A **3**, 1169 (1991).

[4] L. WANG AND M. R. MAXEY, *Settling velocity and concentration distribution of heavy particles in homogeneous isotropic turbulence*, J. Fluid Mech. **256**, 27–68 (2006).

[5] J. BEC, L. BIFERALE, G. BOFFETTA, A. CELANI, M. CENCINI, A. LANOTTE, S. MUSACCHIO, AND F. TOSCHI, *Acceleration statistics of heavy particles in turbulence*, J. Fluid Mech. **550**, 349 (2006).

[6] G. FALKOVICH AND A. PUMIR, *Intermittent distribution of heavy particles in a turbulent flow*, Phys. Fluids **16** (2004).

[7] T. ELPERIN, N. KLEEORIN, M. A. LIBERMAN, V. S. L'VOV, A. POMYALOV, AND I. ROGACHEVSKII, *Clustering of inertial particles in a turbulent flow*, Arxiv preprint nlin.CD/0305017 (2003).

[8] N. MORDANT AND J. F. PINTON, *Velocity measurement of a settling sphere*, Eur. Phys. J. B **18** (2), 343–352 (2000).

[9] W. L. SHEW, S. PONCET, AND J. F. PINTON, *Path instability and wake of a rising bubble*, Phys. Fluids submitted (2005).

[10] C. VELDHUIS, A. BIESHEUVEL, L. VAN WIJNGAARDEN, AND D. LOHSE, *Motion and wake structure of spherical particles*, Nonlinearity **18** (1), C1–C8 (2005).

[11] J. MAGNAUDET AND I. EAMES, *The Motion of High-Reynolds-Number Bubbles in Inhomogeneous Flows*, Ann. Rev. Fluid Mech. **32** (1), 659–708 (2000).

[12] S. DOUADY, Y. COUDER, AND M. BRACHET, *Direct observation of the intermittency of intense vorticity filaments in turbulence*, Phys. Rev. Lett., **67** (8), 983–986 (1991).

[13] J. M. RENSEN, S. LUTHER, AND D. LOHSE, *Velocity structure functions in turbulent two-phase flows*, J. Fluid Mech. **538**, 153–187 (2005).

[14] T. H. VAN DEN BERG, S. LUTHER, AND D. LOHSE, *Energy spectra in microbubbly turbulence*, Phys. Fluids **18**, 038103 (2006).

[15] I. M. MAZZITELLI, D. LOHSE, AND F. TOSCHI, *The effect of microbubbles on developed turbulence*, Phys. Fluids **15**, L5 (2003).

[16] I. M. MAZZITELLI, D. LOHSE, AND F. TOSCHI, *On the relevance of the lift force in bubbly turbulence*, J. Fluid Mech. **488**, 283–313 (2003).

[17] S. LUTHER, J. RENSEN, T. H. VAN DEN BERG, AND D. LOHSE, *Data analysis for hot-film anemometry in turbulent bubbly flow*, Experimental thermal and fluid science **29**, 821–826 (2005).

[18] J. M. RENSEN, S. LUTHER, J. DE VRIES, AND D. LOHSE, *Hot-film anemometry in bubbly flow I: Bubble-probe interaction*, Int. J. Multiphase Flow **31**, 285–301 (2005).

[19] R. ZENIT, D. KOCH, AND A. SANGANI, *Measurements of the average properties of a suspension of bubbles rising in a vertical channel*, J. Fluid Mech. **429**, 307–342 (2001).

[20] G. TRYGGVASON, B. BUNNER, A. ESMAEELI, N. AL-RAWAHI, W. TAUBER, J. HAN, Y. JAN, D. JURIC, AND S. NAS, *A front-tracking method for the computations of multiphase flow*, J. Comp. Phys. **169** (2), 708–759 (2001).

[21] T. AUTON, *The lift force on a spherical body in a rotational flow*, J. Fluid Mech. **183**, 199–218 (2006).

[22] M. R. MAXEY AND J. RILEY, *Equation of motion for a small rigid sphere in a nonuniform flow*, Phys. Fluids **26**, 883 (1983).

[23] N. THOMAS, T. AUTON, K. SENE, AND J. HUNT, *Entrapment and transport of bubbles in plunging water*, Gas Transfer at Water Surfaces (ed. W. Brutsaert & GH Jurka) pp. 255–268 (1984).

[24] P. SPELT AND A. BIESHEUVEL, *On the motion of gas bubbles in homogeneous isotropic flow*, J. Fluid Mech.**336**, 221–244 (1997).

[25] E. CLIMENT AND J. MAGNAUDET, *Large-Scale Simulations of Bubble-Induced Convection in a Liquid Layer*, Phys. Rev. Lett. **82** (24), 4827–4830 (1999).

[26] T. H. VAN DEN BERG, S. LUTHER, I. M. MAZZITELLI, J. M. RENSEN, F. TOSCHI, AND D. LOHSE, *Turbulent bubbly flow*, J. Turbul. **7** (14), 1 (2006).

8

Phase Sensitive Constant Temperature Anemometry[§]

Hot-film measurements in bubbly flows provide time series that contain information about the liquid and the gas phase. Signal classification is required to disentangle the corresponding segments. The classification algorithms are prone to detection bias, which makes hot-film measurements in two-phase flows very difficult. We present a new phase sensitive hot-film probe that provides velocity data and optical phase classification in a single device. We report a proof of concept of this method and demonstrate its accuracy and robustness. Furthermore, we discuss its application to turbulent bubbly flows.

8.1 Introduction

Turbulent bubbly flows are common in nature and in many technical applications. The most important questions are: How do bubbles change the statistical properties of the flow [1–9]? How does the flow modifies the distribution of bubbles [10]? To answer these questions, detailed measurements of both the fluid flow and the bubbles are required. Non-invasive optical measurement techniques are not feasible in many applications due to low opacity of bubbly flows even at low or moderate void fractions. Instead, hot-film anemometry is commonly used in two-phase flow measurements. The signal obtained with this technique contains information on both phases. Two problems arise when using hot-film anemometry in bubbly flows: (i) identification of phase boundaries by detecting bubble-probe interactions; (ii) estimating the statistical prop-

[§]See: Thomas H. van den Berg, Willem D. Wormgoor, Stefan Luther, and Detlef Lohse, *Phase Sensitive Constant Temperature Anemometry*, submitted to Exp. Fluids. (2006)

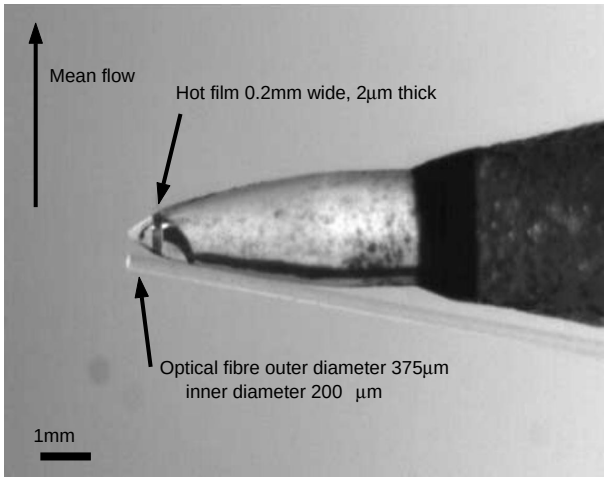

Figure 8.1: Photograph of the conical hot-film probe (55R42, Dantec Inc., Denmark). The probe is aligned perpendicular to the flow, which is directed downwards. The optical fiber is positioned below the conical probe, such that the tip does not occlude the hot-film.

erties of both phases. The first problem poses a significant limitation to this technique since the hot film probes do not provide intrinsic means to distinguish between the liquid and the gaseous phase. Therefore, various parametric or non-parametric signal processing algorithms have been proposed to identify interfacial boundaries [11]. In Refs [6, 12] an indicator function is computed that labels liquid and gaseous parts of the signal. The second problem is to estimate statistical properties of both phases based on a segmented or gapped signal. For this purpose, the previously computed indicator function is used to obtain conditional statistics. It has been shown that the accuracy and robustness of these conditional statistical quantities strongly depend on the indicator function, i.e., the phase detection algorithm [6]. Classification algorithms are prone to detection bias. In many applications of practical interest, this poses a potentially severe conceptual limitation to hot-film measurements in two phase flow.

This paper reports on a new approach by introducing a simple but effective phase sensitive hot-film probe. This is to the best of our knowledge the first report of such a technique. We achieve this goal by combining optical fiber probes for phase detection with conventional hot-film probes. In contrast to hitherto methods, we *measure* the phase indicator function. This approach removes ambiguities associated with computational phase

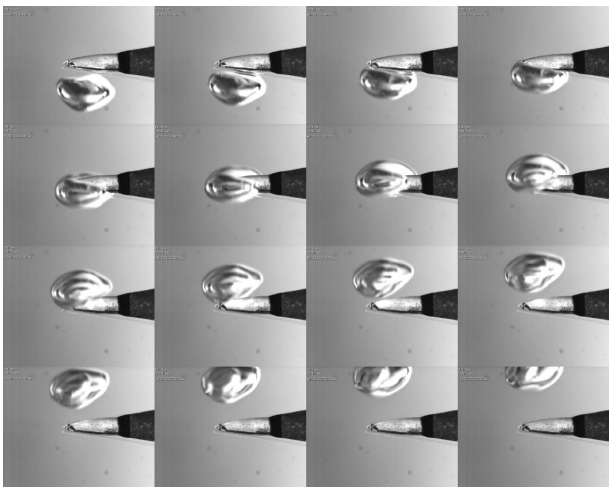

Figure 8.2: Bubble-probe interaction sequence. The flow is directed downwards, the bubble is rising upwards. The bubble diameter (measured along its major axis) is approximately 10 mm. Time proceeds in this panel from left to right and top to bottom. The time interval between two consecutive frames is 1 ms.

detection methods as these methods are prone to errors.

The development of this new experimental method is motivated by our study of the effect of bubbles on fully developed turbulence. Based on numerical studies by Mazzitelli et al. [7, 8], it has been suggested that bubbles enhance the energy density of the flow on small scales, but reduce energy density on large scales. This mechanism has been confirmed experimentally for micro-bubble turbulence by van den Berg et al. [9]. However, it has also been demonstrated by Rensen et al. [6] that such effects on second and higher order statistics can easily be obfuscated by bubble detection ambiguities and artifacts. Therefore, the development of *phase sensitive* constant temperature anemometry, which resolves this problem by direct phase detection, will be an important tool for two-phase flow research.
In this paper, we outline the basic measurement principle in Sec. 8.2 and provide a proof of concept. In Sec. 8.3 we demonstrate its accuracy and robustness by using simultaneous hot-film measurements and high-speed imaging. Furthermore, we apply the method to turbulent bubbly flow, indicating its potential for two-phase flow research in general. The conclusions are given in Sec. 8.4.

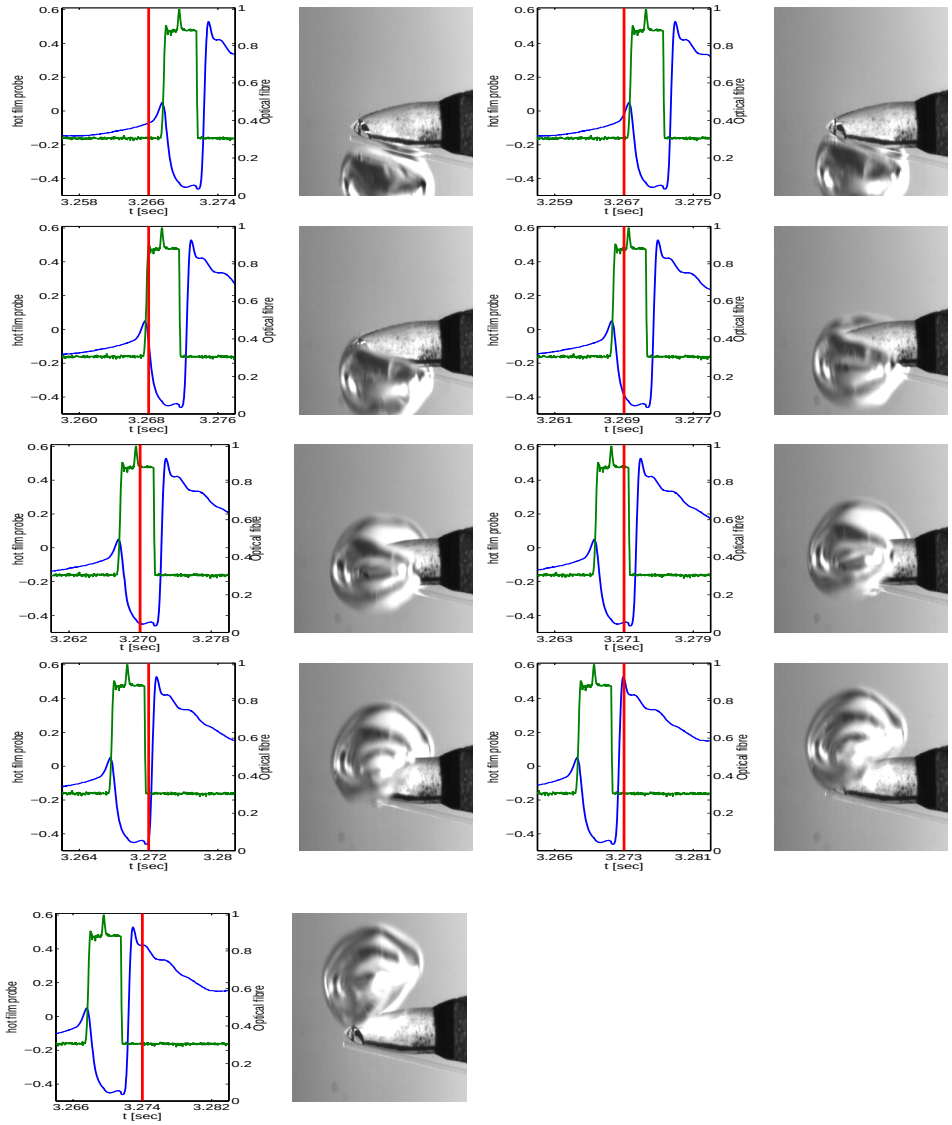

Figure 8.3: Penetrating bubble-probe interaction. Right column: High-speed images of the bubble probe interaction. The field of view is 12 × 11 mm^2. The bubble size is approximately 1cm (major axis) while the mean flow speed was 0.16m/sec. Left column: Hot-film signal and the corresponding fiber optical signal. The vertical line indicates the time at which the image to the right has been taken.

8.2 Methods

A hot-film anemometry consists of an electrically heated sensing element whose heatflux to the surrounding medium is monitored. In constant

temperature mode the film's resistance and hence its temperature is kept constant. The voltage of the sensing element E_{HF} and local flow velocity U are given by King's law

$$E^2{}_{HF} = A + B\,U^n. \tag{8.1}$$

The constants A, B, and n are obtained by calibration with laser doppler anemometry. The application of hot-film anemometry in two-phase flow is complicated by complex bubble-probe interaction. The interfacial dynamics has been investigated in detail. Various types of interactions have been found, such as bouncing, splitting, and penetration of bubbles [13, 14]. The details of these interaction processes depend on the relative orientation, velocity, and size of the bubbles with respect to the probe. However, bubble-probe interactions share some generic features, due to the substantial change of heat flux of the hot-film into the surrounding medium once the bubble is hitting the probe [13]. Typically 5 stages in the bubble probe interaction can be seen in the CTA-signal. First of all when the bubble approaches the probe, the fluid in front of the bubble is pushed forward, giving an increase in flow speed and hence a rise in the signal. This can be seen in Fig. 8.3 from 3.266 s till 3.268s. When the bubble touches the probe, the front surface of the bubble is being deformed until the forces on the bubble are too large for the surface tension and the probe pierces through the interface. In the signal this can be seen from 3.268s till 3.270s. At that point, the liquid layer around the probe becomes so thin that it breaks, exposing the probe to air. When the probe reaches the rear surface, surface tension can again close the bubble and the probe is wetted, causing a large spike in the signal (between 3.272s and 3.273s in our example in Fig. 8.3). The last stage is reached when the bubble has departed from the probe and the signal reaches the normal situation again. The bubble approach signal is slower than the departure signal, as the surface tension prevents the bubble from early breaking at approach, and causes it to leave the probe faster as surface energy is gained at bubble-reformation. A more detailed description of the interaction dynamics is given in [11] and references therein.

Various numerical algorithms have been proposed to identify the presence of a gas-liquid interface within time series obtained with hot-film probes [11]. The identification of segments in this time series that correspond to either phase is a typical classification problem. The simplest – and in some cases optimal – solution is given by thresh-holding the time series based on its amplitude or derivative. If the signal's probability distribution is bi-modal, an optimal threshold can be obtained. This

criterion may or may not be fulfilled, depending on probe type and geometry, bubble size, and flow properties. For example, the threshold on the derivative provides accurate results if the bubbles are significantly smaller than the probe [9]. However, bi-modality is usually not found in turbulent bubbly flow measurements, which renders thresholding algorithms less reliable. A different approach has been developed by Luther *et al.* [12]. It assumes that phase interfaces can be identified by detecting characteristic features of the bubble-probe interaction. The pattern recognition problem is solved using an adaptive wavelet dictionary which is trained with experimental data. It has been demonstrated that this method works with high accuracy and robustness, provided that sufficient training data is available for both phases. Additionally, the pattern recognition approach provides an estimate of the classification error. The disadvantages of the pattern recognition approach are its high computational demand and the extensive need for training data. Training data are obtained by careful measurements of bubble-probe interaction events using simultaneous high-speed imaging [13]. Despite the success of various algorithms to estimate the indicator function *numerically*, an alternate and robust approach to *measure* the indicator function is highly desirable.

Optical fibers provide reliable local phase indication [15, 16]. Their working principle is based on the difference of the index of refraction in either phase [17, 18]. A light source is coupled into the fiber. A photodiode measures the intensity of the light that is reflected from the remote fiber tip via a fiber coupler. The incident light leaves the tip of the fiber when immersed in water, but it is reflected back into the fiber when exposed to air. Thus, the intensity of the reflected light indicates the presence of either gas or liquid at the fiber's tip. If the axis of the fiber optical probe is aligned with the preferential direction of the flow, intrusive interfacial effects are reduced. This results in fast rise and decay times of the optical signal at the interface, while the fiber tip pierces the phase boundary. Optical fibers are available in one, two, and four fiber configurations, which allow for chord length, bubble velocity, and bubble shape distribution measurements, respectively [19].

We combine a single fiber optical probe with a hot-film anemometer, thus providing both phase and velocity information. Fig. 8.1 shows the implementation of this measurement principle. We use a conical hot-film probe (55R42, Dantec Inc., Denmark). The sensor of this probe is placed as a ring (diameter approx. 0.6 mm) around a cone on the tip of a 1.5 mm quartz rod. Sensor dimension is 1.4×0.2 mm^2.
A multi-mode optical fiber (from Laser Components, core diameter $200\mu m$,

cladding diameter $375\mu m$, numerical aperture of 0.22 ± 0.02) is placed next to the sensitive film of the probe. In our set-up, the hot-film probe is mounted perpendicular to the flow. This rather unusual mounting facilitates the study of co- and counter flowing bubbly flows but will inherit a measured delay in the bubble arrival and departure when compared to the probe. We have measured flow velocity with and without the fiber being attached to the probe. We found that the presence of the fiber does not compromise the probe's bandwidth and that its influence on the power spectrum is negligible. This can be seen in Fig.8.4 where we plotted the turbulent spectra for the flow measured with the probe with and without the fibre attached to it, in order to investigate the influence of this fibre. In the inset the spectra measured with the fibre is compensated with respect to the case without the fibre and the largest deviations are found in the higher frequency range dominated by noise, thus causing no problems for our purposes.

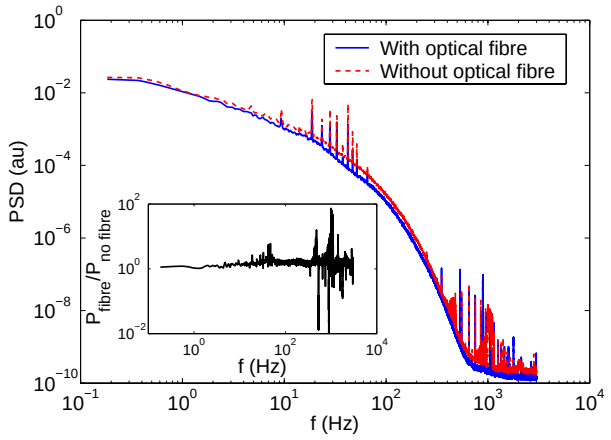

Figure 8.4: The measured spectra for a turbulent flow ($Re = 2\cdot10^4$) measured with the probe with and without the fibre to compare the influence the effect of the fibre on the measured flow. In the inset the spectra with the fibre is compensated with respect to spectra without the fibre. Deviations can be seen around 1kHz, probably due to vortex shedding from the fibre and/or oscillations from the fibre due to the flow. Nevertheless, as these deviations mostly occur in the noise part of the spectral; they do not cause a problem.

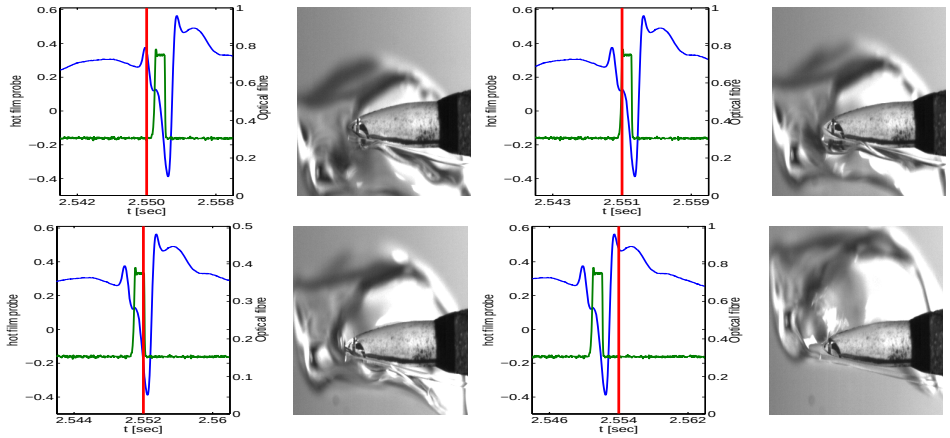

Figure 8.5: Example of bouncing bubble-probe interaction. Figure annotation same as in Fig. 8.3.

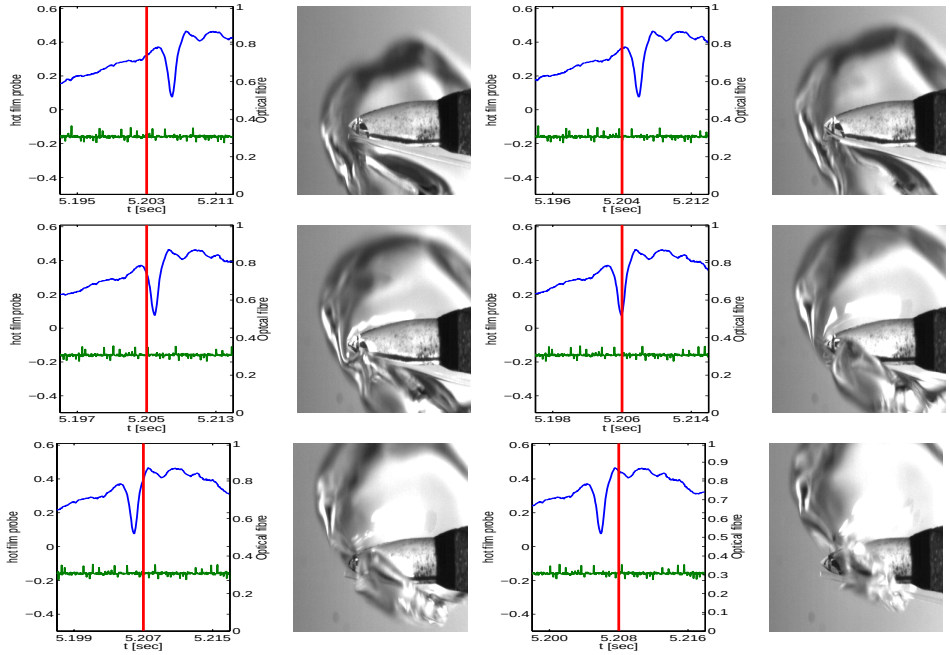

Figure 8.6: Example of glancing bubble probe interaction, which was not detected by the optical fiber. Figure annotation same as in Fig. 8.3.

8.3 Results

The experiments described in this section were done in a small scale two-phase flow test facility. The measurement section is 1.5 m in length and has a cross section of 0.1 $\times$ 0.1 m^2. The water was pumped around by a progressing cavity pump from Allweiler (AEB IE) with a maximum flow capacity of 2900 liters / minute. The probe was located in the top part of the measurement section. A high-speed camera (Photron Ultima APX-RS) is used to image bubble-probe interactions, with a frame rate of 1kHz. Bubbles were injected with a needle with a inner diameter of $0.8mm$, placed in the bottom part of the measurement section. The airflow is controlled by a mass flow controller (MKS coorporation) with a maximum throughput of $100l/min$. Typical bubble sizes are between 1-5 mm. We define the Reynolds number as

$$Re = \frac{Ud}{\nu} \tag{8.2}$$

where U is the mean flow in the channel, d is the channel width, and ν the kinematic viscosity. With a maximum mean flow of 0.9 m s^{-1} we could obtain a Reynolds number of $9 \cdot 10^4$.

8.3.1 Single Bubble Probe Interactions

Fig. 8.2 shows the typically complex interaction of the probe with a large bubble (diameter of the major axis ≈ 10 mm). During this particular event the bubble hits the probe, wraps around it and the tip penetrates the air-water interface. Eventually, the bubble detaches from the probe which induces surface oscillations [13]. Fig. 8.3 shows the bubble-probe interaction event shown in Fig. 8.2 along with hot-film and fiber optical signals. The hot-film signal shows the characteristic interaction features as discussed in Sec. 8.2, corresponding to approach, contact with front surface, penetration, contact with rear surface, and departure. These events can be identified in the corresponding high-speed images in Fig. 8.3. The time series obtained from the optical probe shows an increase of intensity in the second panel at t =3.268s, indicating the penetration of the optical fiber into the bubble. Since the fiber is located downstream of the hot-film, it is expected to detect the arrival of the bubble earlier, and its departure delayed. This introduces an systematic error in our measurements of about 0.5 ms corresponding to an relative error of 10%. Due to this error, the residence times of the bubbles at the probe and hence the void fraction is systematically underestimated. For practical application the resi-

dence times are artificially prolonged in order to mask artifacts following and caused by the dynamic overshoot of the probe. Therefore, this error has no direct effect on velocity measurements. In some case, e.g. if the bubble does not hit the probe centrally, more complex bubble-probe interactions are possible. This effect is inevitable for invasive probes, but it can be minimized by optimizing shape, size, and alignment of the probe. Examples of bouncing and glancing bubble-probe interactions and their corresponding hot-film and optical signals are shown in Figs. 8.5 and 8.6. The presence of the bouncing bubble shown in Fig. 8.5 has been correctly detected by the optical probe. However, the bubble's arrival and departure times are found with significant deviation from the times anticipated from hot-film signal and the high-speed imaging. Therefore, bouncing events bias the void fraction and leave interaction artifacts within the time series if not masked otherwise. Whether or not these complex interaction patterns have significant effects depends on their relative probability and the sensitivity of the physical quantity under investigation.

8.3.2 Turbulent Bubbly Flow

Fig. 8.7 shows a typical measurement with both the hot wire signal and the optical fibre signal. In the top part of the plot the hot wire signal is shown, clearly indicating the large spikes caused by bubble-probe interactions. The optical fibre signal, shown in the lower part of the plot, indicates the presence of a bubble at the probe and thus functions as a phase indicator.

We compare the performance of the phase sensitive constant temperature anemometer against a bubble detection algorithm. This method is based on the pattern recognition approach described in [12]. We record 8 segments of 30 minutes with 10kHz sampling frequency at a $Re = 20.000$. The first four segments were used for training data. For this purpose, bubble-probe interactions are identified by the fiber optical signal. A bubble-probe interaction example vector is obtained by selecting a window of 1250 ms centered around the interaction event. We use 353 such vectors to set up a so called codebook of bubble-probe interactions. A similar codebook is generated for single phase flow data using single phase measurements, this time with approximately 1000 vectors, chosen randomly out of the available single phase data.

Fig. 8.8 shows the result of the classification method. The pattern recognition method successfully detected up to 99% of the bubble probe interactions. About 5% of the fluid segments have falsely been classified

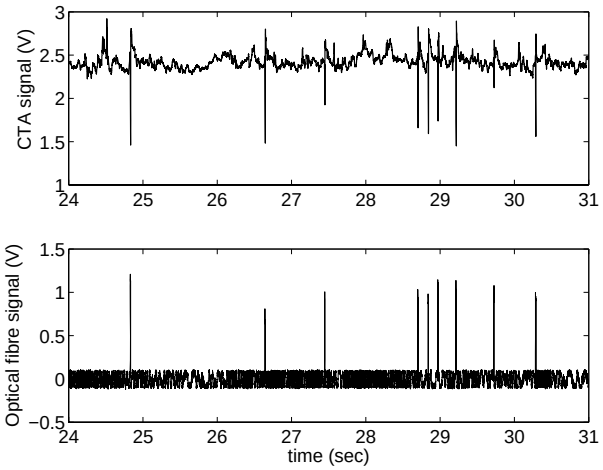

Figure 8.7: The top curve shows the measured signal of the hot film probe in which the bubble-probe interactions are easy to identify due to the simultaneously recorded optical fibre signal which is shown below.

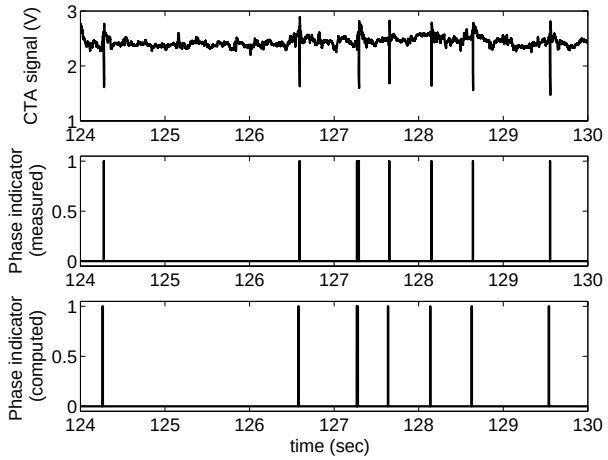

Figure 8.8: Result of the pattern recognition toolbox. In the top the CTA signal is displayed. In the middle we show the optical fibre signal (without noise, i.e. the (measured) phase indicator function). In the bottom the computed phase indicator function as it follows from the pattern recognition toolbox is shown. Although all the bubbles in the shown segment are correctly identified by both the fibre and the pattern recognition toolbox, the optical fibre recording is clearly the preferred method for bubble detection. It is a direct measure of the phase indicator function.

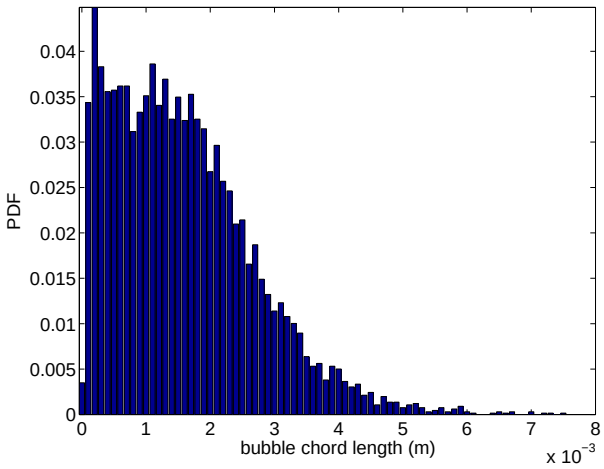

Figure 8.9: Histogram of bubble chord lengths. The mean bubble size is 1.6mm.

as bubbles. However, this classification error affects only the void fraction and dead time estimates only. It does not pose any problems for spectral estimates.

With this combined probe more statistical properties on the flow can be estimated, as the local void fraction [20, 21]. The local void fraction α is defined by

$$\alpha = \frac{1}{T}\sum_{i}^{N} \delta t_i, \tag{8.3}$$

where T is the total measurement time, during which we observe N bubble-probe interactions with residence times δt_i. In our measurements the mean δt_i was $6ms$, leading to a void fraction of 0.5%. Furthermore, the residence time can be related to chord length, provided the bubble velocity is known. We calibrated the signal with simultaneous recorded LDA measurements, for which we could calibrate the anemometer signal. The interfacial velocity can be estimated from the measured velocity at contact time. This gives a rough estimate on the approximate bubble size. The resulting chord length distribution is shown in Fig. 8.8. The mean bubble chord length is 1.6 $\pm$ 0.3 mm. This compares to 4 $\pm$ 1 mm obtained from high-speed imaging. As the bubbles are highly deformable, correct size estimations on the bubble size by high speed imaging recording are not very accurately possible. Furthermore, the bubbles hit the probe perpendicular to the major axis which is evaluated by the high speed image recordings, and the minor axis is measured via the estimate of the bubble

chord length by the optical fibre. More on the accuracies of the optical fibre can be found in [22, 23]. By adding an additional fibre on top of the probe, a more accurate measurement of the residence time, the velocity, and hence the bubble chord length can be made.

8.4 Conclusions

Phase sensitive constant temperature anemometry provides simultaneous phase indication and velocity data. To the best of our knowledge, this is the first report of such a method. In this paper we have provided an experimental proof of concept. The key advantage of this technique is that it does not require the use of phase detection algorithms. Thus it is free from typical detection ambiguities and artifacts. The current simple but efficient implementation using a conical hot-film probe and an optical fiber demonstrates the encouraging accuracy and robustness of this method. The versatility and robustness of the instrument can be further enhanced by incorporating the optical fiber into the conical probe. This should also remove the preferential orientation of the probe. It can be applied to investigate complex two-phase flow phenomena such as turbulent bubbly flow.

References

[1] M. LANCE AND J. BATAILLE, *Turbulence in the liquid-phase of a uniform bubbly air water-flow*, J. Fluid Mech. **222**, 95 (1991).

[2] I. MICHIYOSHI AND A. SERIZAWA, Proceedings Japan-US seminar on two phase flow dynamics, July 29 - August 3, 1984, Lake Placid, NY, USA.

[3] S.K. WANG, S.J. LEE, O.C. JONES, AND R.T. LAHEY, *Statistical analysis of turbulent two-phase pipe flow*, J. Fluids Eng. **112**, 89 (1990).

[4] R.F. MUDDE, J.S. GROEN, AND H.E.A. VAN DER AKKER, *Liquid velocity field in a bubble column, LDA Experiments*, Chem. Eng. Sci. **52**, 4217 (1997).

[5] Z. CUI AND L. S. FAN, *Turbulence energy distribution in bubbling gas-liquid and gas-liquid-solid flow systems*, Chem. Eng. Science **59**, 1755 (2004).

[6] J.M. RENSEN, S. LUTHER, AND D. LOHSE, *The effect of bubbles on developed turbulence*, J. Fluid Mech. **538**, 153 (2005).

[7] I.M. MAZZITELLI, D. LOHSE, AND F. TOSCHI, *The effect of microbubbles on developed turbulence*, Phys. Fluids **15**, L5 (2003).

[8] I.M. MAZZITELLI, D. LOHSE, AND F. TOSCHI, *On the relevance of the lift force in bubbly turbulence*, J. Fluid Mech. **488**, 283 (2003).

[9] T.H. VAN DEN BERG, S. LUTHER, AND D. LOHSE, *Energy spectra in microbubble turbulence*, Phys. Fluids **18**, 038103 (2006).

[10] E. CALZAVARINI, T.H. VAN DEN BERG, S. LUTHER, F. TOSCHI, AND D. LOHSE, *Microbubble clustering in turbulent flow*, submitted to J. Fluid Mech. (2006).

[11] H. H. BRUUN, *Hot-wire Anemometry, Principles and Signal Analysis*, Oxford University Press (1995).

[12] S. LUTHER, J. RENSEN, T.H. VAN DEN BERG, AND D. LOHSE, *Data Analysis for hot-film anemometry in turbulent bubbly flow*, Exp. Therm. Fluid Sci. **29**, 821 (2005).

[13] J.M. RENSEN, S. LUTHER, J. DE VRIES, AND D. LOHSE, *Hot-film anemometry in bubbly flow I: bubble-probe interaction*, Int. J. Multiphase Flows **31**, (3), 285 (2005).

[14] J. DE VRIES, S. LUTHER, AND D. LOHSE, *Induced bubble shape oscillations and their impact on the rise velocity*, Eur. Phys. J. B. **29**, (3), 503 (2002).

[15] A. CARTELLIER, *Local phase detection probes in fluid two-phase flows*, Rev. Sci. Instr. **62**, 279 (1991).

[16] F.J. FORDHAM, *Multi-phase-fluid discrimination with local fibre-optical probes: I. Liquid/liquid flows*, Meas. Sc. Tech. **10**, 1329 (1999).

[17] A. CARTELLIER, *Monofiber optical probes for gas detection and gas velocity measurements: conical probes*, Int. J. Multiph. Fl. **24**, 1265 (1998).

[18] A. CARTELLIER, *Monofiber optical probes for gas detection and gas velocity measurements: optimised sensing tips*, Int. J. Multiph. Fl. **24**, 1295 (1998).

[19] S. GUET, S. LUTHER, AND G. OOMS, *Bubble shape and orientation determination with a four-point optical fibre probe*, Exp. Therm. Fluids Sci. **29 (7)**, 803 (2005).

[20] S. LUTHER, J.M. RENSEN, AND S. GUET, *Bubble aspect ratio and velocity measurement using a four-point fiber-optical probe*, Exp. Fluids **36**, 326 (2004).

[21] A. CARTELLIER, *Simultaneous void fraction measurement, bubble velocity, and size estimate using a single optical probe in gas-liquid 2-phase flows*, Rev. Sci. Instr. **63**, 5442 (1992).

[22] J.E. JULIÁ, R. F. MUDDE, AND H.E.A. VAN DEN AKKER, *On the accuracy of the void fraction measurements using optical probes in bubbly flows*, Rev. Sci. Instr. **76**, 035103 (2005).

[23] A. CARTELLIER, *Optical probes for local void fraction measurements - characterization of performance*, Rev. Sci. Instr. **61**, 874 (1990).

9 Conclusions

The main goal of this thesis was to investigate the effect of bubbles on developed turbulence, either in a bulk flow, or in a boundary layer driven turbulence. We reported on the results following out of experiments conducted on two different setups: the Taylor-Couette Setup and the Twente Water Tunnel.

In the Taylor-Couette Setup several experiments were conducted to investigate the behavior of the nondimensional torque G on different experimental conditions.

We roughened the cylinder walls of the Taylor-Couette cylinders, forcing the laminar boundary layer to a more turbulent state, which lead to a huge increase in drag for fixed Reynolds number as compared to the smooth wall case. We did experiments in the Reynolds number range of $1 \cdot 10^4$ to $1 \cdot 10^6$. Even up to 30 times more torque was required for the rough walled case as compared to the smooth walled case for fixed Reynolds number. Our main interest lay in what would happen if either one of the walls was roughened while the other wall remained smooth. It was shown that the overall drag behavior was dominated by the smooth wall; acting as the rate limiting step for the observed momentum transfer.

We did experiments to shed more light on the intriguing drag reduction phenomena. Bubbles can reduce the drag considerable (colleagues reported in lab conditions 80% was achieved), but what the mechanism behind this effect is, is still a topic of strong debate. We did experiments with rough walls, leading to a strongly turbulent boundary layer. In these experiments even a strong drag increase was observed after bubble injection, while in the smooth wall case we observed strong drag reduction, of even up to 30%. Consequently, we concluded drag reduction by bubbles is a boundary layer effect. Surprisingly, by looking at the dimensional

torque versus rotation rate in Hertz, we observed no change whatsoever for rough wall Taylor-Couette flow with bubbles; not even for the decrease in mass weight. Hence by compensation for the change in mass we surprisingly find a drag increase.

To further invest this phenomenon we looked at whether or not the deformability of the bubbles was the main reason behind the drag reduction observed with bubbles. We injected hollow glass spheres of $\sim 100\mu m$ in the liquid, which are buoyant, like bubbles, but not deformable, unlike bubbles. These hollow glass spheres showed little drag reduction, while the bubbles showed strong drag reduction of up to 30% as mentioned before. Apparently, not only the deformability of the bubbles is of main importance for the drag reduction, but their buoyant properties as well; although leading to a less stronger drag reducing effect than the deformability of the bubbles. Overall we can conclude that drag reduction by bubbles is a boundary layer effect, primarily caused by the deformability of the bubbles.

The effect of bubbles on developed homogenous isotropic turbulence was studied in the Twente Water Tunnel. We injected microbubbles of approximately $100\mu m$ in the flow to investigate the effect on the turbulent power spectra. These experiments were conducted at a Reynolds number of approximately $9 \cdot 10^4$, comparable to previous studies on this topic with larger bubbles; which found a less steeper slope for the power spectra of a two phase turbulent flow. Our bubbles were coflowing in contrast to the larger bubble case and we achieved minute void fractions of $\sim 0.2\%$. As these bubbles were too fast to be accurately resolved by the hot film probe used to measure the velocity fluctuations in the channel, their signature in the signal was a strong large peak caused by the collision of the bubble with the probe. Therefore, removing these bubbles from the signal was straightforward. We found an increase at small scales and a decrease at large scales in the energy spectrum, leading to a less steep slope in the energy spectra as the $-5/3$ Kolmogorov scaling for the single phase case. This was an experimental confirmation of the numerical work explained in Ch. 5. This increase on small scale is caused by the wakes of the bubbles while the reduction on large scales was caused by the accumulation of the bubbles on the downflow side of the vortices due to the strong lift force acting on these bubbles.

We experimentally confirmed this bubble accumulation in Ch. 7 where

we showed that microbubbles with a radius approximately the size of the Kolmogorov length scale η showed preferential concentrating in small scale structures.

In the last chapter, we presented a new experimental technique to discriminate the bubble and fluids part in a hot film signal. This is a problem in two phase flows as these bubble-probe interactions have a huge effect on the estimated power spectra if left in the signal. The removal of these interactions is therefore necessary to be able to tell what the effect of the bubbles is on the turbulent flow. To detect these bubbles in a CTA signal is nevertheless not so straightforward, as these interactions for large bubbles have a multitude of patterns in the CTA signal. We devised a probe, consisting of a conical hot film probe with an optical fibre attached close to the measuring part of the hot film probe; being able to measure simultaneously the CTA signal and the optical fibre signal. Whether the CTA probe was surrounded by a bubble or not can be deduced by looking at the measured phase indicator function from the fibre, making bubble detection in the CTA signal straightforward. We used this probe to test a pattern recognition toolbox which till then had been used as a numerical solution to detect bubbles by identifying typical bubble and fluid patterns in the signal. We showed that the probe was able to accurately detect the bubbles in a hot film signal and the pattern recognition toolbox was able to detect practically all (99%) of the bubbles in a hot film signal; but sometimes labels a turbulent fluid signature erroneously as a bubble. Although incorrect, it does not imply difficulties in data analysis later on as only bubbles in the signal tend to affect the turbulent energy spectra. Nevertheless, considering the huge computational demands of the pattern recognition toolbox and the fact that it does not show a 100% accuracy we recommend the use of this new probe for further turbulent two phase flow research.

Summary

The aim of this work was to investigate the effect of bubbles on turbulent flow. We investigated in turbulent Taylor-Couette flow the effect of turbulent boundary layers on the drag. We showed that this drag can be 30 times higher as compared to the smooth wall case, leading to the conclusion that it is energetically efficient to keep the wall roughness for ships to an absolute minimum. When either one of the two walls is smooth, we observed that the overall behavior of the drag was surprisingly governed by this smooth wall.

As the roughness seems to be of crucial importance for the observed drag, it is as well crucial for the effect of drag reduction by bubbles. We found even a drag increase (up to 15%) in a Taylor-Couette cell with rough walls while in the smooth wall case we found a strong decrease in drag, suggesting that bubble drag reduction is a boundary layer effect.

To further analyze the mechanism for bubble drag reduction, we did experiments with two phase flows in Taylor-Couette flow with smooth walls for which we found drag reduction of up to 30%. We redid these experiments but now instead of bubbles we used hollow glass spheres of approximately $\sim 100\mu m$ diameter in the same volume fraction as the bubbles. These glass hollow spheres are buoyant, but not deformable. We found little drag reduction for these hollow spheres, indicating that drag reduction is mainly due to the bubble deformation in the boundary layers.

To investigate the effect of bubbles on the local properties of a turbulent flow, we used the Twente Water Tunnel. In this setup we investigated the effect of bubbles on the energy spectrum and we tested the hypothesis made by Mazzitelli, Toschi, and Lohse on the preferential accumulation of bubbles in turbulent vortices.

The numerical work done by Mazzitelli *et al.* showed a less steep slope for the spectrum of a turbulent flow, caused by an energy increase at higher frequencies due to the wakes of these bubbles and a energy decrease at lower frequencies because of a reduction of larger structures due to the accumulation of bubbles on the downflow side of the vortices. We did experiments using coflowing microbubbles of approximately $100\mu m$ in diameter in a turbulent flow of a Reynolds number of $9 \cdot 10^4$. We reached a void fraction in the order of 0.2%; in the same regime as the numerical simulations. We found the same less steep slope as in the numerics, though the reduction at the low frequencies was less pronounced as in the

numerics. We believe that this is due to the low void fractions making it difficult to measure these minute effects on the large scales.

We did statistical analysis on the bubble accumulation to see whether or not the bubbles tend to cluster as compared to a normal Gaussian distribution. We found that this is indeed the case, confirming the numerical work.

The last chapter was devoted to the design and testing of a new experimental technique which we believe will be a preferred method to detect bubbles in a hot film signal. While measuring the velocity fluctuations in a turbulent flow, we are interested in the change of the statistics of these fluctuations by the addition of bubbles. These bubbles have a different heat capacity leading to sharp peaks and oscillations in the hot film signals which has a huge effect on the energy spectrum. To remove these bubbles from the hot film signal is a rather complicated task as they imply various different signatures in the signal. Microbubbles, on the other hand, move so fast; they can't accurately be resolved by the hot film probe causing only a large peak in the signal, making them easy to remove. For the large bubbles we need a so called phase discriminating mask, telling whether or not a part of the signal is a bubble or fluid. Several computational pattern recognition methods have been developed by others, some working better than the other but none of them can be 100% accurate if all the bubbles are found in the signal. Besides this, their computational demands are not to be ignored.

We combined an optical fibre with the hot film, as an optical fibre reflects light when inserted in air, and transmits light when inserted in water. Therefore, a bubble present at the tip of the fibre will give a high signal, creating thus a bubble mask itself, telling when bubbles were present at the probe. We tested this probe and showed its potential and accuracy. We were able to detect all the bubbles in the signal and thus the void-fraction of the liquid and the mean bubble size. Furthermore, we used this probe to test the accuracy of the pattern recognition toolbox. This pattern recognition toolbox identifies bubbles and fluid in a CTA signal by means of a so called codebook with either typical fluid signatures, or typical bubble signatures. The pattern recognition toolbox was able to detect 99% of the bubbles in the signal present. Nevertheless, a few fluid segments were coincidentally labeled as being bubbles as well, probably due to the fact that turbulent fluctuations can, by coincidence, actually

look like a bubble. This overestimation of found bubbles does not cause a problem as only left bubbles in the signal give rise to sharp deviations in the evaluated spectra. Although the pattern recognition toolbox does work, we prefer the future use of the phase discriminating probe as this has a higher accuracy and no computational demands, as the phase mask is actually measured instead of calculated.

Samenvatting

Het doel van het werk gepresenteerd in dit verslag betrof het onderzoek van het gedrag van bellen op een turbulente stroming. In een Taylor-Couette opstelling is het effect bestudeerd van turbulente grens lagen op de weerstand. We hebben aangetoond dat de weerstand tot wel 30 keer hoger kan zijn dan in het gladde wanden geval, leidend tot de conclusie dat het energetisch efficient is om de wanden zo glad mogelijk te houden. Met een van de twee wanden glad vonden we verrassend genoeg dat het totale gedrag van de weerstand in de gehele opstelling voornamelijk gedomineerd werd door deze gladde wand.

De ruwheid van de wanden bleek dus van grote invloed op de gemeten weerstand te zijn, hetgeen eveneens van belang bleek voor weerstandsvermindering door bellen. Is er in het gladde wanden geval een weerstandsvermindering van 30% haalbaar door het injecteren van bellen, in het ruwe wanden geval werd er zelfs een weerstandsverhoging geconstateerd. Alhoewel het mechanisme achter weerstandsvermindering nog niet geheel duidelijk is, suggereert ons onderzoek dat het een grens laag effect is.

Om weerstandsvermindering door bellen verder te onderzoeken hebben we onderzoek gedaan in een Taylor-Couette opstelling met gladde wanden waar bellen in geïnjecteerd zijn, waar we een weerstandsvermindering van 30% vonden. We hebben deze experimenten opnieuw uitgevoerd, maar nu hebben we in plaats van bellen, glazen holle balletjes gebruikt met een doorsnee van $\approx 100\mu m$; in een zelfde volume hoeveelheid als bij bellen. Deze holle balletjes bleven wel drijven, maar waren niet vervormbaar, in tegenstelling tot de bellen. We vonden een veel kleinere weerstandsvermindering met deze glazen balletjes dan in vergelijking met de bellen, wat aangeeft dat weerstandsvermindering door bellen voornamelijk te danken is aan de bel vervorming in de grens lagen.

Om het effect van bellen op de lokale eigenschappen van een turbulente stroming te onderzoeken hebben we onderzoek gedaan in het Twente Water Kanaal. In deze opstelling onderzochten we het effect van de bellen op het turbulente energie spectrum en testen we de hypothese gedaan door Mazzitelli, Toschi en Lohse op accumulatie van bellen in turbulente wervels.

Het numerieke werk gedaan door Mazzitelli en anderen lieten een mindere sterke helling zien in het energie spectrum van een turbulente stroming, veroorzaakt door een stijging in energie voor de hogere frequenties als gevolg van oscillaties geïnduceerd door het zog van de bellen, en

een vermindering in energie voor de lagere frequenties als gevolg van een vermindering in kracht van de grotere wervels door het accumuleren van de bellen in de naar beneden gerichte stromings kant van de wervels. We hebben metingen gedaan waarbij we bellen gebruikten van ongeveer $100\mu m$ in diameter in een turbulente stroming met een Reynolds getal van $9 \cdot 10^4$. Het volume percentage was ongeveer 0.2%, in hetzelfde regime als in het numerieke geval. We vonden eveneens een minder sterke helling; alhoewel de vermindering voor de lagere frequenties minder sterk was dan in de simulaties. Wij denken dat dit komt door het bijzonder kleine effect wat bij deze lage volume percentages zeer moeilijk te meten valt.

We hebben statistische analyses uitgevoerd om te kijken of de bellen inderdaad accumuleren, in vergelijking met een normale Gaussische distributie. Dit bleek inderdaad het geval te zijn, wederom de numerieke simulaties bevestigend.

Het laatste hoofdstuk behandelde het ontwerp en testen van een nieuw experimentele methode wat, naar wij verwachten, de voorkeur zal krijgen om bellen in een hete film signaal te detecteren. Bij het meten van snelheidsoscillaties in een turbulente stroming, zijn we primair geïnteresseerd in de verandering in de statistische eigenschappen van deze vloeistof snelheidsfluctuaties als gevolg van deze toegevoegde bellen. Maar, deze bellen hebben een andere warmte overdracht, wat leidt tot sterke pieken in het hete film signaal wat een groot effect heeft op het energie spectrum. Deze bellen verwijderen uit het hete film signaal is een behoorlijk gecompliceerde taak aangezien deze bel - hete film interacties divers in karakter kunnen zijn. Microbellen, daarentegen bewegen zo snel dat ze amper kunnen worden gedetecteerd door de hete film sensor. Zij veroorzaken dan ook slechts een grote piek in het signaal, wat makkelijk te detecteren is en te verwijderen. Voor de grotere bellen hebben we een zogenaamde fase onderscheidend masker nodig, dat vertelt of een gedeelte van het signaal hetzij een bel, hetzij vloeistof betreft. Verscheidene numerieke patroon herkenningsmethodes zijn ontworpen, maar geen van allen zijn in staat om alle bellen uit een signaal te verwijderen. Dit nog los bezien van het feit dat het veel tijd en rekenkracht kost om deze bellen te detecteren via deze numerieke methodes.

We hebben een optische fiber gecombineerd met een hete film sensor, aangezien een optische fiber licht reflecteert wanneer hij zich in lucht bevindt, en licht doorlaat zodra hij in water bevindt. Hierdoor zal een bel aan het einde van de fiber een hoog signaal geven, en op deze manier een fase onderscheidend masker creëren door hoge signalen te geven zodra er een bel zich bevindt aan het einde van de fiber. We hebben deze

gecombineerde sensor getest en zijn nut en accuraatheid aangetoond. We waren met deze sensor in staat om alle bellen in een hete film signaal te detecteren en zodoende ook het volume percentage van bellen in de stroming, en de gemiddelde grootte van de bellen. We hebben deze sensor gebruikt om de accuraatheid van de patroon herkenning programmatuur te testen. Deze programmatuur identificeert bellen en vloeistof oscillaties aan de hand van zogenaamde 'codeboeken' met daarin opgeslagen typische bel interacties met de sensor en typische turbulente vloeistof stroming interacties. De geteste patroon herkenning programmatuur bleek in staat om 99% van de aanwezige bellen in het hete film signaal te herkennen. Er werden echter ook enkele gedeeltes met vloeistof stroming interacties foutief geclassificeerd als bellen; waarschijnlijk doordat deze stroming interacties bij toeval ook een bel sensor profiel kunnen aannemen. Deze foutief gelabelde 'bellen' vormen geen probleem aangezien alleen bellen in het signaal achtergelaten van grote invloed zijn op de te bepalen energie spectra. Alhoewel de patroon herkenning programmatuur goed werkt, geven wij de voorkeur aan het werken met de nieuwe fase onderscheidende sensor, aangezien deze een hogere accuraatheid heeft en geen rekenkracht behoeft, doordat het fase masker direct gemeten wordt en niet hoeft te worden berekend.

Acknowledgements

And so I have arrived at the final part of the thesis. For me it is the hardest part and presumably it is the most read part of the thesis. It is for me the hardest part, as I have an annoying habit of forgetting a lot. Blame my age if you like but I am sure I will forget a lot of people here: so to start with; I apologize, and thank them nevertheless. Making sure I have now a fail proof acknowledgement section I can continue.

Doing research is a weird kind of job; if you even might call it a job. It is sometimes some sick kind of psychological self mutilation, sometimes it is high speed email checking and trying to beat CNN in fast news gathering and sometimes it is just good old plain fun. It sure is perseverance, although I must say I certainly see more positive than negative parts to my job.

First of all, I am deeply indebted to my supervisor, Prof. Detlef Lohse, who was always willing to help me at whatever time of day (Detlef gives me a call: 'Do I call you at a convenient time? No? Well, in that case we'll keep it brief...'), who showed huge flexibility in allowing me to do to several other tasks next to my PhD-work; like World Year of Physics co-organizing, the visit of 40 kids ('Ramon: I've invited 40 children to pay a visit to our group in upcoming December, can you fix that?') or giving me the opportunity to work part time at the Public Relations Department of the faculty. For this, I am also grateful to my employer, stichting FOM, who agreed on this 'off-track' distractions from my PhD-work. Detlef realized what my interests are (doing experimental work; the dirty work and having a lot of different topics to work on) and helped me to achieve these interests. For that, I am extremely grateful to him.

Besides Detlef, the group in total has helped me a lot in finishing my PhD-work. I would like to thank Gert-Wim Bruggert and Martin Bos for their deeply needed technical assistance *('No, Gert-Wim I really really really have no clue how that could have happened'* or *'whoops, clumsy me')*, Bas Benschop for sometimes deeply needed assistance on computing business and Joanita Leferink for her shared cups of coffee and administrative invaluably help. Her optimism in starting a VISA request procedure can only be regarded with the utmost respect.

I would like to thank Ko van der Weele for his shared senseo cups of coffee after our shared tutored course on Classical Dynamics in which we

sometimes barely made it out alive and Devaraj van der Meer as my co-supervisor for helping me several times with reading my papers and helping me with accepting the fact that one sometimes just doesn't have a clue on what is going on in the lab. Gerrit de Bruin is thanked for introducing me to the fact that turbulence is actually everywhere: in your beer, in another beer, and look, even in that glass of beer!

Of course a warm thanks goes to my supervisor Stefan Luther, whom was for me a good reason to start in this group in the first place ('Après nous, le déluge'). We had a great project in the first few months, Project 1 Terabyte, which had a success rate of 23%. Naive of me, all that data had to be analyzed as well and around that time Stefan told me he got an appointment at Cornell University in the USA. The fact that Stefan left after nine months is not taken personally by me, but we kept in close contact, both on scientific as well as personal parts which is highly appreciated. I can only hope he will someday appreciate the delicacies of Dutch cuisine, like 'kroketten'. Stefan went with me for a few weeks to the USA, where I worked in the lab of prof. Dan. Lathrop. I am deeply grateful for Dan his help and hospitality over the years, as well as prof. Charlie Doerings help. I have really had a great (and extremely productive) time in the USA, but, to be fair, it made me appreciate the Netherlands even more.

I would like to thank my co-author of Ch. 7, Enrico Calzavarini. He really had a hard time even finding me sometimes due to my part time job at the PR-department but luckily we came up with a nice paper eventually! I nevertheless need to apologize for both the weather and the coffee in the Netherlands, which must be tough for an Italian to cope with.

Furthermore I would like to thank Judith Rensen, who helped me start up in the first place and I continued in her place. She quickly showed me the nasty things of the big tunnel and told me to bring boots. I learned that doing experiments is just sometimes keeping fingers crossed and hope for the best once everything is running. And don't be afraid of the water, it is just water. Only a lot.

All the PhD's in the group are thanked of course, especially my roommates Hanneke, Marlies, Henk Jan and Sander, whom 'missed' me the last months as I worked at home a lot in finishing my thesis. This was done because the fun we have in the office is not a real productive atmosphere. See it as a compliment!

From the students over the years I especially would like to thank Willem Wormgoor and Dennis van Gils whose research ended up in this thesis.

During my time in Twente I have made loads of friends, primarily because of my involvement in the study association of the faculty applied physics, s.v. Arago. I have really appreciated the years there and for that I would thank the several boards over the years.

Although several friends offered me to help me write up these acknowledgements (making sure they will get the place they deserve in their opinion) I will try to do it myself. I have to say; even an online auction was taking place to decide what ranking my friends would deserve but I would like to thank the following friends for doing two phase research in beer and other related fun (in *no* particular order): Jeroen, Martijn, Gossie, Erik, Roel, Merel, Petra, Joris, Joost, Rob and Eric.

The last few years for me personally were sometimes quite turbulent as well and most certainly not the easiest part of my life, although not everybody might have noticed that. I am deeply indebted to a few who helped me on the way: René van de Ven, Sjoerd Ligthart, Wouter Peeters, Jeroen Huijben, Frans Jonkers, Gijs and Aafke.

Oan Kor Bras: Ik wit dat ik it dy net altiten like maklik makke ha. Dochs hoopje ik dasto nearne spyt fan hân hast, ik in elts gefal net. Tige tank foar dyn abslúte leafde en oanwêzigens, hoe dreech it foar dy bytiden ek wie. Tút.

Two need to be mentioned separately: Sander van der Meer and Hester Broekhuis. The friends dearest to me and they have on several occasions redefined the term friendship for me, in a most positive way. Their support has been invaluable and I'm extremely grateful they agreed to be my paranimf on my PhD defense.

Last: I would like to thank my family, in particular my parents Henk and Joke van den Berg for their never tiring support and guidance; although they might not realize their impact on my life. I thank them for giving me the opportunities they never had and state that this achievement is as much their effort as it is mine.

About the Author

Thomas Hendrik (Ramon) van den Berg was born on June 2nd, 1976 in Reeuwijk, The Netherlands. He graduated from high school 'Scholengemeenschap Christelijk Lyceum-HAVO' in Gouda in 1996, and started that same year studying Applied Physics at the University of Twente in Enschede. During his study he co-organized a studytour to Scandinavia, was for two years head editor of the faculty magazine Focus, was one year chairman of the study association for Applied Physics and was involved in several other tasks in this association. For this, he was unanimously chosen honorary member for life in 2003 of this association. In 2002 he went for a four month intership to the group of prof. Daniel Lathrop at the University of Maryland, USA. He graduated in 2003 on the study of Rarefaction Waves in Bubbly liquids in the group of prof. Detlef Lohse; after which he started his PhD work in the same group. During his PhD work he spent several months conducting research in the aforementioned group of prof. Daniel Lathrop and had a 5 months part time occupation in the Public Relations Department of the faculty of Applied Physics at the University of Twente.